

2010

Optimization and application of ultrasound attenuation estimation algorithms

Yassin Labyed
Iowa State University

Follow this and additional works at: <https://lib.dr.iastate.edu/etd>

 Part of the [Electrical and Computer Engineering Commons](#)

Recommended Citation

Labyed, Yassin, "Optimization and application of ultrasound attenuation estimation algorithms" (2010). *Graduate Theses and Dissertations*. 11249.
<https://lib.dr.iastate.edu/etd/11249>

This Dissertation is brought to you for free and open access by the Iowa State University Capstones, Theses and Dissertations at Iowa State University Digital Repository. It has been accepted for inclusion in Graduate Theses and Dissertations by an authorized administrator of Iowa State University Digital Repository. For more information, please contact digirep@iastate.edu.

Optimization and application of ultrasound attenuation estimation algorithms

By

Yassin Labyed

A dissertation submitted to the graduate faculty
in partial fulfillment of the requirements of the degree of
DOCTOR OF PHILOSOPHY

Major: Electrical Engineering

Program of Study Committee:
Timothy Bigelow, Major Professor
Aleksandar Dogandzic
Viren Amin
Namrata Vaswani
Adin Mann

Iowa State University

Ames, Iowa

2010

Copyright © Yassin Labyed, 2010. All rights reserved.

Table of contents

1	INTRODUCTION.....	1
2	LOCAL ATTENUATION ESTIMATION OF THE CERVIX OF PREGNANT PATIENTS.....	9
2.1	INTRODUCTION	9
2.2	HYPOTHESIS	9
2.3	<i>IN-VIVO</i> DATA ACQUISITION METHODS	10
2.4	VALIDATION OF THE SPECTRAL DIFFERENCE METHOD	11
2.5	RESULTS	25
2.6	DISCUSSION	33
3	COMPARISON OF LOCAL ATTNEUATION ESTIMATION ALGORITHMS	36
3.1	INTRODUCTION	36
3.2	THE SPECTRAL DIFFERENCE METHOD.....	38
3.3	THE SPECTRAL LOG DIFFERENCE METHOD	41
3.4	THE HYBRID METHOD	42
3.5	SIMULATION PARAMETERS AND RESULTS	45
3.5.1	<i>Simulation parameters</i>	45
3.5.2	<i>Homogeneous region of interest</i>	48
3.5.3	<i>In-homogeneous region of interest with varying scatterer number density</i>	52
3.5.4	<i>Inhomogeneous region of interest with varying scatterer size</i>	56
3.6	TISSUE MIMICKING PHANTOM RESULTS	59
3.7	DISCUSSION	65
4	DERIVATION AND VALIDATION OF THE TWO PROPOSED ALGORITHMS FOR TOTAL ATTENUATION ESTIMATION.....	72
4.1	INTRODUCTION	72
4.2	DERIVATION OF THE PROPOSED ALGORITHMS.....	73
4.2.1	<i>Derivation of the modified spectral fit algorithm</i>	74

4.2.2	<i>Derivation of the modified multiple filter algorithm</i>	78
4.3	STATISTICAL ANALYSIS OF THE TOTAL ATTENUATION ESTIMATION ALGORITHMS	79
4.3.1	<i>Statistical analysis of the power spectrum</i>	80
4.3.2	<i>Statistical analysis of the modified spectral fit method</i>	82
4.3.3	<i>Statistical analysis of the modified multiple filter algorithm</i>	86
4.4	VALIDATION OF STATISTICAL ANALYSIS RESULTS USING COMPUTER SIMULATIONS	89
4.4.1	<i>Simulation Procedure</i>	89
4.4.2	<i>Validation of the power spectrum statistical analysis</i>	91
4.4.3	<i>Validation of the spectral fit statistical analysis</i>	99
4.4.4	<i>Validation of the multiple filter statistical analysis</i>	102
5	COMPARISON OF THE TWO PROPOSED ALGORITHMS FOR TOTAL ATTENUATION	
	ESTIMATION	108
5.1	COMPARISON BASED ON THEORY	108
5.2	COMPARISON USING SIMULATIONS	109
5.3	COMPARISON USING A SPHERICALLY FOCUSED TRANSDUCER	113
5.4	COMPARISON USING A CLINICAL ARRAY TRANSDUCER	117
5.5	FREQUENCY DEPENDENCE OF THE BACKSCATTER.....	120
5.6	DISCUSSION	122
6	SUMMARY AND DISCUSSION	126
	APPENDIX A: OTIMIZATION OF THE SPECTRAL DIFFERENCE METHOD FOR USE IN THE	
	LONGITUDINAL STUDY OF THE PREGNANT PATIENT CERVIX	140
	APPENDIX B: PROCEDURE FOR EXTRACTING THE RAW DATA FROM A ZONARE ULTRASOUND	
	SYSTEM	145
	APPENDIX C: PROCEDURE FOR OBTAINING LOCAL ATTENUATION MAPS	147
	APPENDIX D: PROCEDURE FOR OBTAINING TOTAL ATTENUATION MAPS	152

APPENDIX E: PROCEDURE FOR OBTAINING THE BACKSCATTER COEFFICIENT	156
APPENDIX F: PROCEDURE FOR OBTAINING THE SCATTERER SIZE	161
ACKNOWLEDGMENTS	166
REFERENCES	167

LIST OF FIGURES

<u>Figure 1</u> The correlation coefficient between the time sample at 6 μ s and the rest of the time samples of the RF echo lines of the reference phantom	14
<u>Figure 2</u> Plot of the correlation coefficient between the 100 th echo line and the echo lines from 80 to 120.....	15
<u>Figure 3</u> Scatter plot of the mean and standard deviation of the error in the attenuation coefficient estimates versus ROI size. Each symbol represents a different window length that is used to gate the time domain waveform.....	18
<u>Figure 4</u> Surface plot of the mean of the error in the ACEs versus window size and ROI length.....	20
<u>Figure 5</u> Surface plot of the STD of the percent error in the ACEs versus window size and ROI length.....	21
<u>Figure 6</u> Plot of the mean and STD of the percent errors in the ACEs with respect the number of echoes per ROI	23
<u>Figure 7</u> Attenuation map for a B-mode image from phantom 1 (0.64 dB/cm-MHz).....	24
<u>Figure 8</u> B-mode image obtained from the cervix of a 14 week pregnant patient.....	26
<u>Figure 9</u> Superimposed attenuation estimate for the B-mode image obtained from the cervix of a 14 week pregnant patient	27
<u>Figure 10</u> B-mode image obtained from the cervix of a 38 week pregnant patient.....	28
<u>Figure 11</u> Superimposed attenuation for the B-mode image obtained from the cervix of a 38 week pregnant patient	29
<u>Figure 12</u> Scatter plot of the ultrasonic attenuation coefficient versus the interval time from the ultrasound examination to delivery.....	31

<u>Figure 13</u> Scatter plot of the ultrasonic attenuation versus the cervical length at the ultrasound examination.....	32
<u>Figure 14</u> Scatter plot of the ultrasonic attenuation versus the gestation age at the time of ultrasound examination.....	33
<u>Figure 15</u> Plot of the Full Width Half Maximum bandwidth of the backscatter power spectrum of the reference phantom with respect to the size of the time gated windows in spatial pulse lengths	47
<u>Figure 16</u> The mean (a) and (b) the standard deviation (STD) in the percent error of the attenuation coefficient estimates that were obtained using the spectral difference method from the homogeneous sample, versus the number of pulse lengths and the number of echoes per ROI.....	49
<u>Figure 17</u> The mean (a) and (b) the standard deviation (STD) in the percent error of the attenuation coefficient estimates that were obtained using the spectral log difference method from the homogeneous sample, versus the number of pulse lengths and the number of echoes per ROI.....	50
<u>Figure 18</u> The mean (a) and (b) the standard deviation (STD) in the percent error of the attenuation coefficient estimates that were obtained using the hybrid method from the homogeneous sample, versus the number of pulse lengths and the number of echoes per ROI	51
<u>Figure 19</u> The mean (a) and (b) the standard deviation (STD) in the percent error of the attenuation coefficient estimates that were obtained using the spectral difference method from the inhomogeneous sample that has the same effective scatterer size but different	

scatterer number densities, versus the number of pulse lengths and the number of echoes per ROI..... 53

Figure 20 The mean (a) and (b) the standard deviation (STD) in the percent error of the attenuation coefficient estimates that were obtained using the spectral log difference method from the inhomogeneous sample that has the same effective scatterer size but different scatterer number densities, versus the number of pulse lengths and the number of echoes per ROI..... 54

Figure 21 The mean (a) and (b) the standard deviation (STD) in the percent error of the attenuation coefficient estimates that were obtained using the hybrid method from the inhomogeneous sample that has the same effective scatterer size but different scatterer number densities, versus the number of pulse lengths and the number of echoes per ROI.... 55

Figure 22 The mean (a) and (b) the standard deviation (STD) in the percent error of the attenuation coefficient estimates that were obtained using the spectral log difference method from the inhomogeneous sample that has the same scatterer number density but different effective scatterer size, versus the number of pulse lengths and the number of echoes per ROI 57

Figure 23 The mean (a) and (b) the standard deviation (STD) in the percent error of the attenuation coefficient estimates that were obtained using the hybrid method from the inhomogeneous sample that has the same scatterer number density but different effective scatterer size, versus the number of pulse lengths and the number of echoes per ROI..... 58

Figure 24 (a) The correlation coefficient of the time sample at $12 \mu s$ with the rest of the time samples of the RF echo lines of the reference phantom and (b) the hydrophone measured pulse length of the clinical array transducer 60

<u>Figure 25</u> Plot of percent error in the mean of attenuation slope versus the number of independent echoes and number of pulse lengths per ROI for the spectral difference method	62
<u>Figure 26</u> Plot of percent error in the mean of attenuation slope versus the number of independent echoes and number of pulse lengths per ROI for the spectral log difference method.....	63
<u>Figure 27</u> Plot of percent error in the mean of attenuation slope versus the number of independent echoes and number of pulse lengths per ROI for the hybrid method.....	64
<u>Figure 28</u> The expected percent error and the measured percent error in the attenuation coefficient slope of the sample using the hybrid method and the modified spectral log difference method for the four simulated cases.	71
<u>Figure 29</u> A plot of the normalized power spectrum obtained from averaging 50 power spectra from the sample and the reference in the simulations	91
<u>Figure 30</u> Plot of the square of the mean and the variance of 100 power spectra obtained from the sample.....	92
<u>Figure 31</u> plot of the correlation coefficient of the power spectrum at frequency 7.5 MHz with the rest of the frequency components in the usable frequency range.	94
<u>Figure 32</u> Plot of the expected variance and the measured variance of the power spectrum that is obtained by averaging (a) 10 periodograms and (b) 25 periodograms.	96
<u>Figure 33</u> Plot of the expected variance and the measured variance of the power spectrum that is obtained by taking the ratio of (a) 25 averaged periodograms of the sample and 25 averaged periodograms of the reference (b) 50 averaged periodograms of the sample and 50 averaged periodograms of the reference	98

Figure 34 Plot of the expected variance and the measured variance of the power spectrum that is obtained by taking the natural logarithm of the ratio of (a) 25 averaged periodograms of the sample and 25 averaged periodograms of the reference (b) 50 averaged periodograms of the sample and 50 averaged periodograms of the reference..... 100

Figure 35 Plots of the measured and theoretical standard deviation of the estimate $d\alpha_s$, which was obtained using the spectral fit method with an ROI length of (a) 5 pulse lengths (b) 10 pulse lengths (c) 15 pulse lengths (d) 20 pulse lengths, with respect to the number of independent of echoes per ROI..... 102

Figure 36 Plots of the measured and theoretical standard deviation of the estimate $d\alpha_s$, which was obtained using the multiple filter method with 2 Gaussian filters and an ROI length of (a) 5 pulse lengths (b) 10 pulse lengths (c) 15 pulse lengths (d) 20 pulse lengths, with respect to the number of independent of echoes per ROI..... 105

Figure 37 Plots of the measured and theoretical standard deviation of the estimate $d\alpha_s$, which was obtained using the multiple filter method with 4 Gaussian filters and an ROI length of (a) 5 pulse lengths (b) 10 pulse lengths (c) 15 pulse lengths (d) 20 pulse lengths, with respect to the number of independent of echoes per ROI..... 106

Figure 38 Plots of the measured and theoretical standard deviation of the estimate $d\alpha_s$, which was obtained using the multiple filter method with an ROI length of 10 pulse lengths and an ROI width of 60 independent echo lines, with respect to the number of Gaussian filters.... 107

Figure 39 Plots of the theoretical standard deviation of the estimate $d\alpha_s$, which was obtained using spectral fit method and the multiple filter method with 2 Gaussian filters with an ROI length of (a) 5 pulse lengths (b) 10 pulse lengths (c) 15 pulse lengths (d) 20 pulse lengths, with respect to the number of independent of echoes per ROI..... 109

Figure 40 Plots of the (a) bias (b) STD, and (c) MSE of the estimate $d\alpha_s$, which was obtained using the multiple filter method with 3 independent Gaussian filters, the multiple filter method with 3 Gaussian filters, the multiple filter method with two independent filters, and the spectral fit method, with respect to the number of independent of echoes per ROI for an ROI length of 10 pulse lengths..... 112

Figure 41 Plots of the (a) bias (b) STD, and (c) MSE of the estimate $d\alpha_s$, which was obtained using the multiple filter method with 3 Gaussian filters, the multiple filter method with two independent filters, and the spectral fit method, with respect to the number of pulse lengths per ROI for an ROI that contains 50 independent echo lines..... 113

Figure 42 Plots of the (a) bias (b) STD, and (c) MSE of the estimate $d\alpha_s$, which was obtained using the multiple filter method with 3 independent Gaussian filters, the multiple filter method with 3 Gaussian filters, the multiple filter method with two independent filters, and the spectral fit method, with respect to the number of independent of echoes per ROI for an ROI length of 10 pulse lengths..... 116

Figure 43 Plots of the (a) bias (b) STD, and (c) MSE of the estimate $d\alpha_s$, which was obtained using the multiple filter method with 3 Gaussian filters, the multiple filter method with two independent filters, and the spectral fit method, with respect to the number of pulse lengths per ROI for an ROI that contains 45 independent echo lines..... 117

Figure 44 Plots of the (a) bias (b) STD, and (c) MSE of the estimate $d\alpha_s$, which was obtained using the multiple filter method with 3 independent Gaussian filters, the multiple filter method with 3 Gaussian filters, the multiple filter method with two independent filters, and the spectral fit method, with respect to the number of independent of echoes per ROI for an ROI length of 12 pulse lengths..... 119

- Figure 45** Plots of the (a) bias (b) STD, and (c) MSE of the estimate $d\alpha_s$, which was obtained using the multiple filter method with 3 Gaussian filters, the multiple filter method with two independent filters, and the spectral fit method, with respect to the number of pulse lengths per ROI for an ROI that contains 60 independent echo lines..... 120
- Figure 46** Plot of (a) the relative error and (b) the standard deviation in the estimates of $d\alpha_s$ versus the frequency dependence of the backscatter 122
- Figure 47** Plot of the normalized power spectrum versus frequency, for the Gaussian focused beam in the simulations, the spherically focused transducer, and the clinical array transducer. 125
- Figure 48** Attenuation map for the cervix of a pregnant patient (1.28 ± 0.98 dB/cm-MHz). Axial ROI size = 3 pulse lengths, Lateral ROI size = 5 independent echo lines 128
- Figure 49** plot of the normalized power spectra that are obtained from a TMP by exciting a clinical array transducer (L8-3 Linear Array Transducer, z.one Ultrasound System, ZONARE Medical Systems, Inc.) at three difference frequencies 132
- Figure 50** plot of (a) the ratio of the power spectra from Figure 48 by the power spectra that are obtained for a reference tissue mimicking phantom and (b) the spectrum that is obtained from combining the high frequency spectrum and low frequency spectrum from plot (a). . 133
- Figure 51** Total attenuation map of the 0.7dB/cm-MHz tissue mimicking phantom that is obtained by using the multiple filter method with two independent Gaussian filters and using the spectrum that is obtained from exciting the transducer at one center frequency (~ 7 MHz) only. The axial ROI size is 12 pulse lengths and the lateral ROI size is 35 independent echo lines. Mean= 0.6003 ± 1.06 dB dB/cm-MHz..... 136

- Figure 52** Total attenuation map of the 0.7dB/cm-MHz tissue mimicking phantom that is obtained by using the multiple filter method with two independent Gaussian filters and using the spectrum that combines the spectra from three excitement frequencies of the transducer. The axial ROI size is 12 pulse lengths and the lateral ROI size is 35 independent echo lines. Mean= 0.7085 ± 0.13 dB/cm-MHz..... 137
- Figure 53** Total attenuation map of the 0.7dB/cm-MHz tissue mimicking phantom that is obtained by using the multiple filter method with two independent Gaussian filters and using the spectrum that is obtained from exciting the transducer at one center frequency (~ 7 MHz) only. The axial ROI size is 6 pulse lengths and the lateral ROI size is 10 independent echo lines. Mean= 0.54 ± 2.35 dB/cm-MHz 138
- Figure 54** Total attenuation map of the 0.7dB/cm-MHz tissue mimicking phantom that is obtained by using the multiple filter method with two independent Gaussian filters and using the spectrum that combines the spectra from three excitement frequencies of the transducer. The axial ROI size is 6 pulse lengths and the lateral ROI size is 10 independent echo lines. Mean= 0.7013 ± 0.53 dB/cm-MHz..... 139
- Figure 55** Local attenuation map of the reference tissue mimicking phantom that is obtained using the spectral difference method for an axial ROI size of 3 pulse lengths and a lateral ROI size of 5 independent echo lines. 0.4435 ± 1.10 dB/cm-MHz 143
- Figure 56** local attenuation maps of the reference tissue mimicking phantom that is obtained using the spectral difference method for an axial ROI size of 10.5 pulse lengths and a lateral ROI size of 10 independent echo lines. 0.47 ± 0.12 dB/cm-MHz 144

LIST OF TABLES

<u>Table 1</u> Characteristics of the 40 study participants by gestational age at the time of the cervical examination	25
<u>Table 2</u> The mean and the STD of the local attenuation coefficient estimates in the reference tissue mimicking phantom. The estimates were obtained by using the spectral difference method on the RF data of the reference tissue mimicking phantom that is obtained from the trans-vaginal array transducer.....	142

ABSTRACT

Ultrasound imaging is widely used in clinical settings because of its safe non-ionizing radiation and its low cost. The ultrasound images are generated by performing envelope detection on the backscattered signals. These images show different tissues, organs, and major blood vessels (qualitative information only). In the past three decades however, there has been strong interest in obtaining quantitative information about tissue microstructure by analyzing the backscattered signals rather than using envelope detected data only. The backscattered signals contain information about the size, shape, distribution and mechanical properties of the scatterers within the tissues. These properties can be related to the state of the tissue and may be used to differentiate between healthy and diseased tissue. The tissue microstructure information however, can only be obtained if the total ultrasonic attenuation along the propagation path to the region of interest is accurately compensated. The primary contribution of this thesis is developing two methods for estimating the attenuation along the propagation path. Statistical analysis is performed on each method, and the results are validated using computer simulations and tissue mimicking phantoms. The second contribution is estimating the local ultrasonic attenuation in the cervix of human pregnant patients for the purpose of diagnosing premature delivery. The final contribution is optimizing three common local attenuation estimation algorithms, by using computer simulations and tissue mimicking phantoms.

1 INTRODUCTION

Ultrasound imaging is a modality that has been used to image soft tissues for decades. Unlike light microscopy which uses electromagnetic waves to detect changes in the refractive index (dielectric) between different materials, the longitudinal ultrasound waves detect changes in the mechanical (compressibility, density) properties of tissues [1]. At low diagnostic powers, ultrasound is considered safe compared to other ionizing radiation modalities such as X-ray imaging. The portability of ultrasound imaging equipment and its low-cost compared to other imaging modalities makes it suitable for use in clinical settings.

Conventional ultrasound pulse-echo B-mode imaging uses transducers with nominal center frequencies between 1 to 20 MHz depending on the desired tissue to be imaged. However, because B-mode imaging only measures the envelope of the RF signals, the frequency dependent information of the backscattered radio frequency (RF) signals is not utilized. This allows only organs, and large tissues and blood vessels to be visualized (tissue macrostructure only) [2]. In the last three decades however, there has been interest in obtaining quantitative information about the tissue structures that are on the order or smaller than the wavelength of the center frequency of the transducer (tissue microstructure). This is accomplished by analyzing the frequency dependence of the backscattered RF signals rather than retaining the envelope data only. The size, shape, distribution, and mechanical properties of the scatterers within the tissue determine the frequency dependence of the backscattered signals. These properties can be related to the state of the tissue and may be used to differentiate between healthy and diseased tissue, differentiate between different types of tumors or lesions, predict the stage of a disease, monitor the progress of a disease, and monitor the change in tissue properties due to therapeutic agents [1, 3-7].

The process of interaction between ultrasound and human tissues are fundamentally of two kinds: absorption processes in which acoustic energy is transformed into thermal energy, and scattering processes in which the acoustic energy is re-radiated from the site of interaction with properties varying from those of the incident wave [8]. Both processes contribute to the attenuation of the ultrasound wave as it propagates through tissue. In this thesis, we discuss the local attenuation and the total attenuation, both of which are very important parameters in tissue characterization using ultrasound. The local attenuation is the ultrasonic attenuation within a region of interest (ROI) in tissue; it is frequency dependent and varies from tissue to tissue. The total attenuation is the attenuation of the sound wave as it propagates from the surface of the transducer to the ROI. The total attenuation depends on the local attenuation of the overlying tissues that lead to the ROI.

The reflected signals from soft tissue can be represented in three classes [9, 10]. The first class is incoherent scattering which results from randomly positioned diffuse scatterers of sufficient concentration to give an echo signal with Gaussian statistics and yet tenuous enough to assume that the positions of individual scatters are uncorrelated and that multiple scattering is negligible. The average scattering intensity from this diffuse tissue is I_d [10-12]. In incoherent scattering, the power spectrum is frequency dependent and includes information about the size, shape, density, and mechanical properties of the scatterers. The second class is coherent scattering which results from non-randomly distributed microstructures. The scattered wavelets from each scatterer add up constructively to generate a strong signal with mean intensity I_s . Examples of coherent scatterers include the long range order of the portal triads in liver parenchyma and the collagenous sheaths that surround muscle bundles [9, 13]. In coherent scattering, the power spectrum is also a

function of the individual scatterer properties but is strongly dependent on the spatial variation of the scatterers. When the scatters are not randomly spaced in the volume, then resonance peaks would appear in the spectrum corresponding the spacing of the scatters. For random scattering, the coherent spectrum appears as noise (called spatial variation noise) [1, 3]. The third class is specular reflection which occurs at smooth boundaries that are much bigger than the wavelength, such as bone. In specular reflection, the magnitude of the echo is independent of frequency and is only a function of the acoustic impedance difference between the two tissues at the boundary, and the angle of incidence. The acoustic impedance is a function of the density and compressibility of the tissue. In soft tissue however, compressibility differences between different types of tissue are larger than density differences, and therefore reflection and scattering are due mainly to compressibility changes [14].

In ultrasound tissue characterization, only regions of tissues that generate coherent and incoherent scattering are of interest since the backscattered signals from these tissues contain quantitative information about the tissue microstructure. Many parameters can be extracted from the backscattered signals and one or a combination of these parameters may prove useful in characterizing that tissue of interest. The main parameters that have been investigated are the ultrasonic attenuation coefficient, the ratio of coherent to incoherent backscatter intensity I_s/I_d , the backscatter coefficient, the scatterer size, the acoustic concentration, and the average scatterer spacing. With the exception of the local attenuation coefficient, the estimation of all these acoustic parameters requires the total attenuation along the propagation path to be known. This is a consequence of the frequency dependence of both the attenuation and the backscattered signals from the tissue microstructures. Therefore,

obtaining an accurate estimate of the total attenuation along the propagation path is essential to extracting quantitative tissue microstructure information from the backscattered ultrasonic signals.

The ratio of incoherent to coherent backscatter intensity was used by Fellingham to differentiate between normal and infarcted heart muscle [15]. The heart suffers morphological changes in the form of collagen deposition which changes the properties of the tissue and results in a coherent component in the backscattered signal. The ratio of incoherent to coherent backscatter intensity was also used to characterize tissues such as the kidney, spleen and liver [9].

The mean scatterer spacing was used to characterize the liver and to diagnose diffuse liver disease [9, 13]. Normal liver is organized in lobules that have a roughly hexagon form whose angles are the portal triad veins and whose center is the central vein. The connective tissues in the veins of the central and portal veins are spaced approximately 1mm apart. In a liver diffusely involved with cirrhosis, a composite of nodules and thickened fibrotic septae is organized on a larger scale than the structure of the normal liver. Results showed that the normal liver had an average scatter spacing of 1.07mm while cirrhotic liver had an average scatterer spacing of 1.55mm.

Scatterer size and acoustic concentration estimates were performed by Oelze and O'Brein to characterize and differentiate between rat mammary fibroadenomas and carcinomas [16]. Results showed that in fibroadenomas, the average scatterer diameter and the acoustic concentration are $105 \pm 25 \mu\text{m}$ and $-15.6 \pm 5 \text{ dB/mm}^3$ respectively, and for carcinomas $28 \pm 4.6 \mu\text{m}$ and 10.6 dB/mm^3 , respectively. Scatterer size estimates were also

used in ophthalmology studies by Lizzi et al to diagnose retinal detachments that occur prior to the development of degenerative processes [5, 17].

The attenuation coefficient was used by Landini to distinguish malignant breast tumors characterized by fibrosis from normal fatty tissue [18, 19]. The attenuation coefficient was also used to differentiate between the normal liver, liver with chronic active hepatitis, and fatty infiltrated liver [20]. Results showed that the liver with chronic active hepatitis (inflammatory disease) had lower than normal attenuation coefficients while fatty infiltrated liver (diffuse liver disease) had a higher than normal attenuation coefficient.

The backscatter coefficient was used to diagnose liver disease [7, 8], diagnose vitreous hemorrhages in the eye [4, 17], differentiate between different ocular tumors [4], and to differentiate between carcinomas and fibroadenomas in rat mammary tumors [16]. The linear regression of the backscatter coefficient with respect to frequency provides three parameters that have been found to be collectively significant for tissue characterization. Specifically, these parameters are the spectral slope (dB/MHz), intercept (dB), and the statistical standard error at the intercept, or simply the residual (dB) [4].

The tissue microstructure information that is contained within the backscattered RF signals is modified by the transducer directivity function, the transmit pulse, the electro-mechanical properties of the transducer, and the total ultrasonic attenuation along the propagation path to the region of interest. The directivity function depends on frequency, propagation sound speed, and spatial location. In biological tissues, with the exception of bone, the variation in sound speed is less than 5% with a mean speed of 1540 m/s [15]. The sound speed is also a very weak function of frequency over the range 1-10MHz. In single

element transducers where the transducer geometry is well known, the directivity function can be calculated accurately and the effects of the transmit pulse and the electromechanical properties of the transducer can be compensated by using a planar specular reflector with a known reflection coefficient [4, 21]. In clinical array transducers, however, the directivity function is very complex due to the various patterns that are used to excite the multiple elements of the transducer to achieve beam steering and focusing. It is also difficult to compensate for the transmit pulse and electromechanical properties of clinical transducers using planar reflectors. One efficient method that was developed to compensate for these effects is based on obtaining reference backscattered signals from a well characterized tissue mimicking reference phantom with known attenuation and scattering properties [22, 23].

When tissue characterization is performed *ex-vivo*, the tissue of interest is often excised to eliminate the problem of intervening tissues and through transmission techniques are employed to measure the frequency dependent attenuation of the tissue of interest [8]. A compilation of the attenuation coefficients of different human and animal tissues is given by Dunn [24]. However, if ultrasound tissue characterization is to be useful clinically, *in-vivo* pulse echo techniques are essential and the total attenuation must be known. Some investigators compensate for the attenuation along the propagation by path by assuming a value for the attenuation coefficient [25]. This however, can lead to erroneous estimates of tissue microstructure parameters. Others measured the thickness of the overlying tissues based on the boundaries of intervening tissues and assigned an attenuation coefficient value to each tissue based on existing values that were measured *ex-vivo* [26]. This can lead to erroneous results due to the inaccuracies in the thickness measurements (sound speed changes), the inaccuracies of the assigned attenuation coefficients which were measured ex-

vivo (low blood perfusion), and the variability of the attenuation coefficients due to in between patient variability.

Recently, Bigelow et al developed a method to simultaneously estimate the scatter size and the total attenuation along the propagation path to the ROI [27, 28]. The algorithm also assumes that the attenuation coefficient has linear frequency dependence. The algorithm was developed for spherically focused transducers with known geometries, and used a planar reflector to compensate for the effects of the transducer and the transmit pulse. A more recent technique by Bigelow makes use of several Gaussian filters in an effort to make the previous algorithm less dependent on the frequency dependence of the tissue scattering [29]. However, his analysis did not include a statistical analysis of the dependence of the variance in the estimates on the parameters of the algorithms.

The research work in this thesis is composed of three main parts. In the first part, we estimated the local ultrasound attenuation coefficient in the cervix of human pregnant patients. This study was performed to test the hypothesis that the ultrasound attenuation decreases with increasing gestational age, and to examine whether the ultrasound attenuation could potentially be used to diagnose premature delivery. Changes in the ultrasonic attenuation with increasing gestation age may signal the dynamic changes in tissue structure that occur prior to delivery. If preterm cervical ripening is accurately diagnosed, new drugs could potentially be developed to delay cervical ripening and prevent early delivery.

In the second part of the thesis, we used computer simulations and tissue mimicking phantoms to compare the three algorithms that use a tissue mimicking reference phantom to estimate to the local ultrasound attenuation, namely the hybrid method, the spectral difference method, and the spectral log difference method. This study was performed to

quantify the dependence of the algorithms on the ROI size, and to examine the effects of variations in scatterer number density and scatter size within the ROI on the accuracy of each method. The results of this study are important because they give insight into choosing the optimal method for estimating the local ultrasonic attenuation in the tissue of interest based on the available ROI size and the level of homogeneity within the ROI. For example, we will argue that the spectral difference method is the optimal method for estimating the attenuation coefficient in the cervix of pregnant patients.

In the third part, we modified the total attenuation estimation algorithms that were developed by Bigelow to permit their use in clinical settings where array transducers are used. We also performed statistical analysis on the two algorithms in order to quantify their dependence on the ROI size, the bandwidth, and the number of Gaussian filters (multiple filter algorithm). The algorithms were then compared and validated using computer simulations and tissue mimicking phantoms. The results of this study demonstrate the feasibility of these algorithms in estimating the total attenuation to a region of interest in tissue, and quantify the ROI size and the bandwidth that are required to obtain a certain precision in the estimates of total attenuation. This is important because estimating other acoustic parameters that are related to tissue microstructure such as the backscatter coefficient and the scatterer size, hinges on the compensating for the total attenuation. For example, the differentiation between fibro-adenomas and carcinomas based on scatterer size estimates requires the scatterer size estimates to be accurate with a certain precision. The precision of the scatterer size estimates is dependent on the precision of the total attenuation estimates and hence on the ROI size and the available bandwidth.

2 LOCAL ATTENUATION ESTIMATION OF THE CERVIX OF PREGNANT PATIENTS

2.1 Introduction

Premature delivery is the leading cause of infant mortality in the United States and it is estimated that neonatal care costs 10 billion dollars annually [30]. Since the introduction of medications to halt contractions, the preterm birth rates have not been reduced and the medications carry significant maternal and fetal risks [31]. Prior to uterine contractions, the cervix undergoes a long period of phasic changes in the microstructure and composition [32]. During this period often referred to as cervical ripening, the concentration of collagen decreases as more space is created between the fibrils. Water and other enzymes occupy this space and act to loosen collagen fibrils and soften elastin in preparation for delivery [33]. These cervical changes that occur before preterm birth go undetected because women do not have symptoms (contractions) or signs (vaginal discharge). If preterm cervical ripening is accurately diagnosed, new drugs could potentially be developed to delay cervical ripening and prevent early delivery.

A preliminary *in vivo* study on pregnant rats demonstrated that the decreased collagen concentration associated with cervical ripening clearly affected ultrasonic attenuation in cervical tissue [34]. The study showed that estimates of attenuation corresponded to gestational age changes in the rat cervix as ripening occurred, and that attenuation was greater at early gestational age and decreased as pregnancy advanced toward term.

2.2 Hypothesis

In pregnancy, as the collagen rich cervix prepares for labor and birth, the cervix transforms from a rigid structure to a soft extensible structure that contains high water content and low collagen concentration [33]. Ultrasonic attenuation has been observed to be related to tissue stiffness, collagen content and water concentration of tissues [18, 35]. It is thus hypothesized that by estimating changes in ultrasonic attenuation with increasing gestation age, the dynamic changes in tissue structure and function can be detected.

2.3 *In-vivo* data acquisition methods

A sample of 40 pregnant women underwent a single ultrasonic examination during pregnancy using a 6.8 MHz trans-vaginal array transducer (E9-4, z.one Ultrasound System, ZONARE Medical Systems, Inc., Mountain View, CA). The gestational age at the time of the cervical ultrasound examination ranged from 10 – 40 weeks gestation. Two sagittal scans of the cervix were acquired from each woman and the cervical length was measured from the internal os to the external os in each image. Immediately after the ultrasonic data was acquired from the patient, the same transducer and settings were used to acquire reference data from a well characterized tissue mimicking phantom. The tissue mimicking phantom had an attenuation coefficient of 0.64 dB/cm-MHz and a sound propagation speed of 1540 m/s which is similar to the propagation speed in soft tissue. The scattering targets in the phantom were glass beads with a number density of 5 mm^{-3} and a scatterer diameter of 45 μm . The phantom was custom fabricated at the University of Wisconsin Madison by Ernest L. Madsen.

Digital Imaging and Communications in Medicine (DICOM) data of the beam formed images of the patient and phantom were saved on a flash drive, and converted to RF data on a

personal computer with a Matlab® (Mathworks, Natick, MA) program supplied by Zonare®. Gestational age of the fetus at the time of cervix scans was determined by a first trimester ultrasound. Pregnancy characteristics and previous history of preterm birth were collected via patient interview. Gestational age at delivery and neonatal outcome data were collected by a telephone verbal report by the patient.

Our collaborator at the University of Illinois Chicago (Barbara L McFarlin) chose the ROIs from the cervix images for obtaining the local attenuation estimates. The ROIs were chosen so that they correspond to homogenous areas of the cervix with adequate sizes to obtain reasonable attenuation estimates. Due to the variation in tissue architecture between the patients, the same region of the cervix could not be chosen for each patient image. The spectral difference method (described in Chapter 3) was used to estimate the local ultrasonic attenuation within each selected ROI of the patients' cervix images. The mean of the attenuation coefficient estimates of the selected ROIs in each patient image was chosen to be the attenuation value for that patient. During the processing of the RF data, I was blinded to gestation age and clinical information about the patients.

2.4 Validation of the spectral difference method

Prior to applying the spectral difference algorithm to the *in vivo* cervix data, it was validated by using two homogeneous tissue mimicking phantoms with attenuation coefficients 0.64 dB/cm-MHz (phantom 1) and 0.5 dB/cm-MHz (phantom 2) respectively. Phantom 1 is the same phantom that was used to obtain the reference data for the cervix images. Phantom 2 was also fabricated at the University of Wisconsin Madison and had a sound propagation speed of 1540 m/s. The scattering targets in phantom 2 were glass beads

with a number density of 5 mm^{-3} and mean scatterer diameter of $45 \text{ }\mu\text{m}$. Using the same trans-vaginal array transducer that was used to obtain the cervix data, the two phantoms were insonified with the same system settings and 5 RF data sets corresponding to 5 different B-mode images were obtained for each phantom. One of the data sets from phantom 1 is chosen as the reference, and the spectral difference method was used to estimate the attenuation coefficients in the remaining 9 data sets.

The error in the attenuation coefficient estimates depends on the ROI length (number of spatial pulse lengths) and the ROI width (number of independent echo lines). We employed a correlation technique to measure the spatial pulse length of the transducer because it is difficult to measure it experimentally. The number of correlated adjacent time samples in an RF echo line multiplied by the sampling period corresponds to the pulse length (μs). To determine the pulse length, the correlation coefficient was measured among the adjacent time samples of the RF data that is obtained from phantom 1. The following equation is used to calculate the correlation coefficient [26]:

$$\rho = \frac{\sum_{i=1}^m [(X_i - \bar{X})(Y_i - \bar{Y})]}{\sqrt{\sum_{i=1}^m [(X_i - \bar{X})^2 (Y_i - \bar{Y})^2]}}$$

(2.1)

where X_i and Y_i are the RF echo amplitudes of the time samples X and Y, respectively, at echo line i of the RF data. \bar{X} and \bar{Y} are the sample mean values. The pulse length was chosen so that it corresponds to the time samples for which the absolute value of the correlation coefficient is above 0.2. This result is validated experimentally in section 3.6 and

in Figure 24. Figure 1 shows the correlation coefficient between the time sample at 6 μs and the rest of the time samples of the RF echo lines that are obtained from the reference phantom. Based on this figure, the time pulse length of the trans-vaginal transducer is approximately 0.8 μs (0.6 mm, 2.5λ). 0.6 mm is the spatial pulse length and is given by

$$\Delta x = \frac{c\Delta t}{2} \quad (2.2)$$

where Δx is the spatial pulse length, Δt is the time pulse length, and c is the sound speed. The spatial pulse length can also be written in terms of the wavelength λ of the center frequency f_c of the transducer according to equation (2.3). In the rest of this thesis, we refer to spatial pulse length as simply the pulse length.

$$\frac{\Delta x}{\lambda} = \frac{c\Delta t}{2\lambda} \quad (2.3)$$

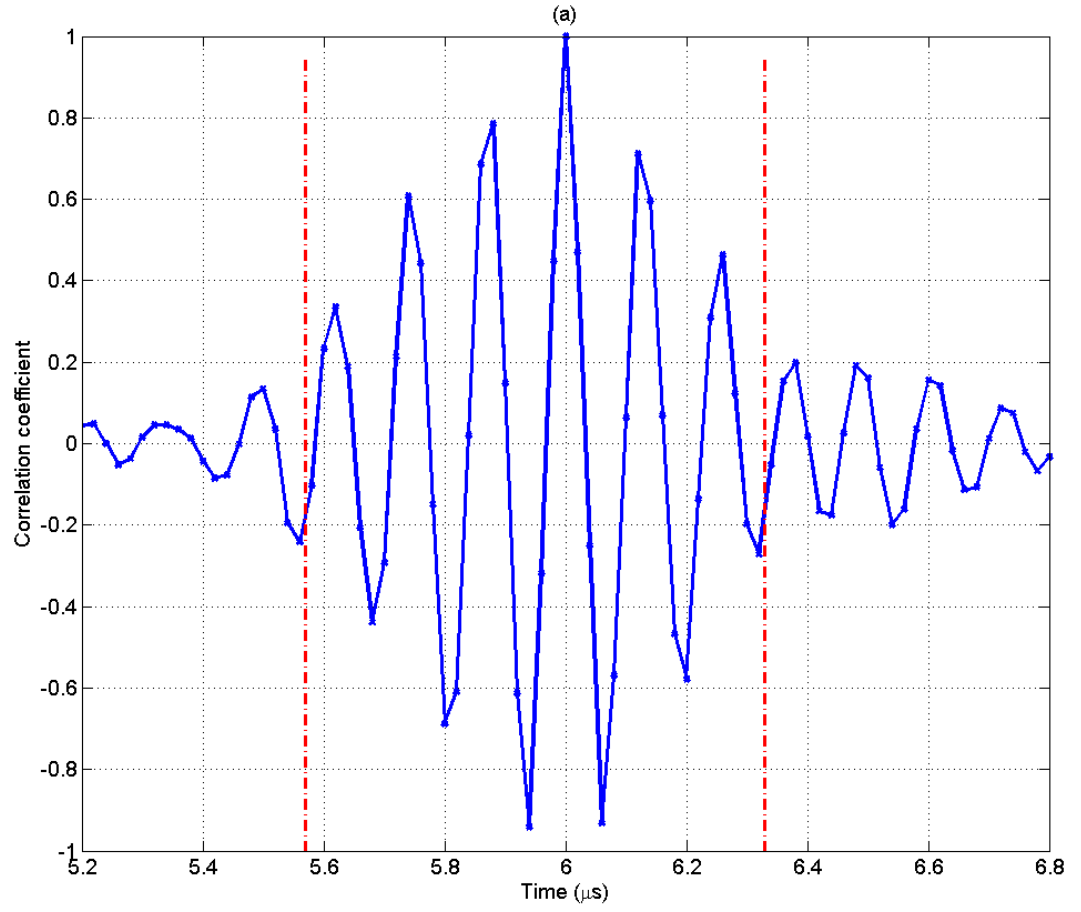


Figure 1 The correlation coefficient between the time sample at 6 μs and the rest of the time samples of the RF echo lines of the reference phantom

To determine the number of uncorrelated echo lines in the ROI, the correlation coefficient was measured among adjacent echo lines from the reference phantom using equation (2.1). This time however, X_i and Y_i are the RF echo amplitudes of echo lines X and Y, respectively, at time sample i of the RF echo data, and \bar{X} and \bar{Y} are the sample mean values. Figure 2 shows the correlation coefficient between the 100th echo line and the echo lines from 80 to 120. Based on this figure, the correlation coefficient is less than 0.2 between

echo lines that are separated by at least two adjacent lines. Thus with a 20% criterion for de-correlation, we considered the echo lines that are separated by two lines to be uncorrelated.

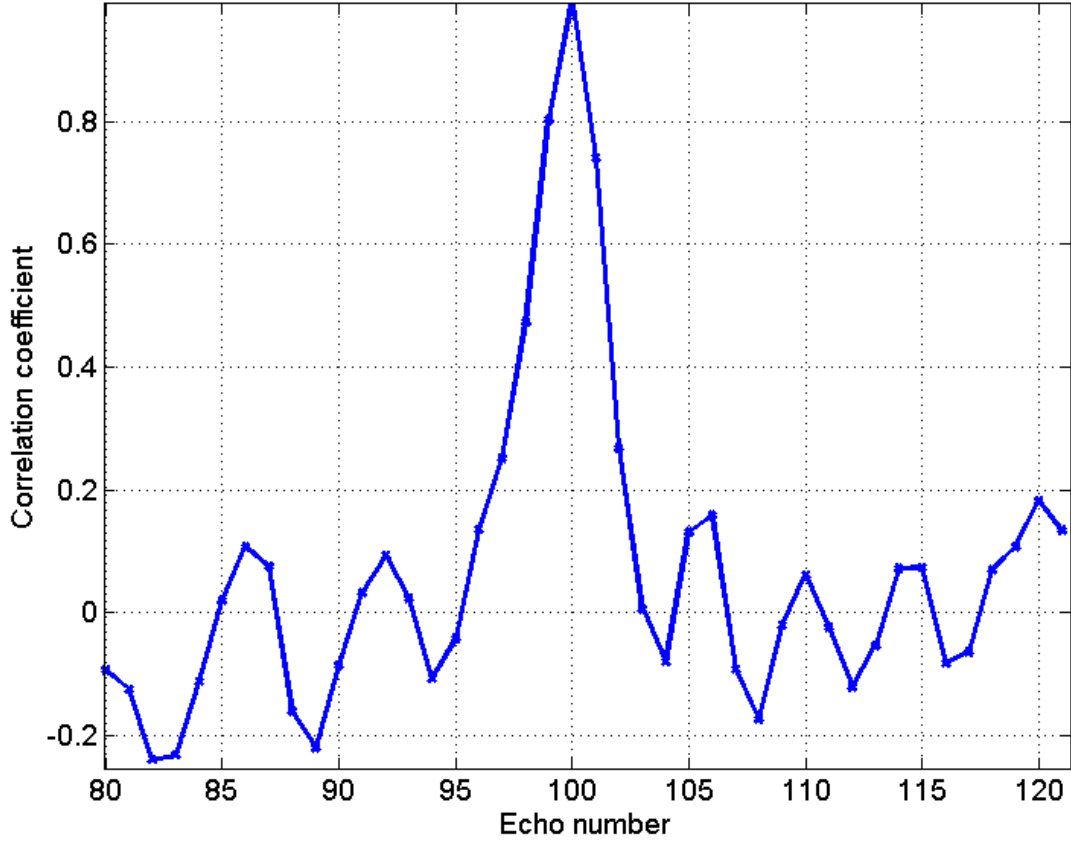


Figure 2 Plot of the correlation coefficient between the 100th echo line and the echo lines from 80 to 120

In order to obtain the least error in attenuation coefficient estimates (ACEs), parameters such as the ROI length, the size of the time gated window that is used to compute the Fourier Transform at each depth within the ROI, and the number of independent echoes per ROI must be optimized. The ROI length in the axial direction is composed of multiple overlapping time gated windows. To optimize the ROI length and the length of the time

gated window, we took ROIs that consisted of 50 echo lines (17 independent echo lines) and varied the size of the time gated window from 2 pulse length (2.5λ , $0.8 \mu\text{s}$) to 10 pulse lengths (25λ , $8 \mu\text{s}$) with increments of 0.4 pulse lengths. The length of the ROI was also varied from 4 pulse lengths (10λ , $3.2 \mu\text{s}$) to 29 pulse lengths (75λ , $23.2 \mu\text{s}$) by varying the number of time gated windows per ROI. We chose 50% overlapping between the time gated windows. For every combination of window size and ROI length, one ROI was selected from each B-mode image so that the center of the ROI corresponds to the center of the B-mode image. The selected ROIs correspond to the same depth. The spectral difference method was then used to estimate the attenuation coefficient in the selected ROI of each data set. Subsequently, the error in the attenuation coefficient estimate of each ROI was calculated according to the following equation:

$$Error = \frac{\alpha_{true} - \alpha_{est}}{\alpha_{true}} \times 100 \quad (2.4)$$

In this equation, α_{true} is the true attenuation coefficient of the sample and α_{est} is the estimated attenuation coefficient of the ROI. Lastly, for every combination of window size and ROI length, the mean and standard deviation of the errors in the ACEs of the nine ROIs were calculated. Note that we didn't calculate the mean square error (MSE) in the ACEs because the MSE combines the bias and the variance in the ACEs together. Although the MSE is a good measure of the overall performance of the algorithm, it doesn't quantify the contribution of the bias and the contribution of the variance to the error in the ACEs.

Figure 3 shows a scatter plot of the mean and the standard deviation of the error in the attenuation coefficient estimates versus ROI size. Each symbol represents a different

window size that is used to gate the time domain waveform. It is apparent from the figure that for a specific ROI size, the magnitudes of the mean and STD of the errors in the ACEs exhibit little variation with respect to window size (i.e., different symbols). It is also observed that the mean and STD of the errors in the ACEs decrease with increasing ROI size. For ROI sizes that are greater than 16 pulse lengths (40λ , $12.8 \mu\text{s}$), there is little or no decrease in the mean and STD of the errors in the ACEs. In this study, we used all 50 echo lines of the ROI, i.e. we didn't skip every other 2 echo lines to make sure that all the echo lines in the ROI are independent. In another study that was performed later in time (see Chapter 3), we made sure that all the echo lines of the ROI are independent.

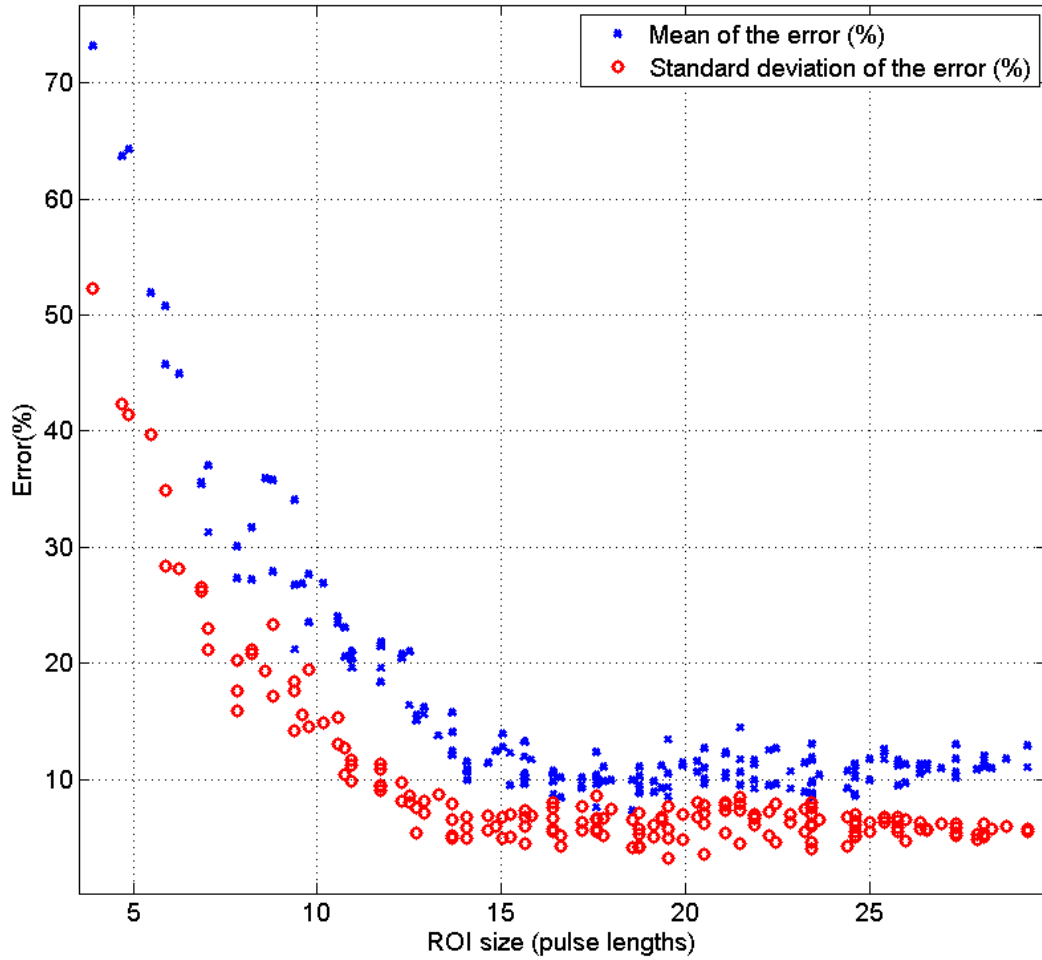


Figure 3 Scatter plot of the mean and standard deviation of the error in the attenuation coefficient estimates versus ROI size. Each symbol represents a different window length that is used to gate the time domain waveform

In order to explore the dependence on ROI length and window size in greater detail, we generated surface plots of the mean and STD of the errors in the ACEs with respect to ROI length and window size. The two plots are shown in Figure 4 and Figure 5, respectively. Visually assessing the two plots, it is observed that the mean and STD of the errors in the ACEs stay nearly constant with respect to ROI length for ROI lengths greater than 16 pulse

lengths (40λ , $12.8 \mu\text{s}$). For a specific ROI length, the mean and STD of the errors in the ACEs are nearly constant with respect to window size for window sizes greater than 2 pulse length (5λ , $1.6 \mu\text{s}$). The mean and STD of the errors in the ACEs are less than 15% and 10% respectively for ROI lengths greater than 16 pulse lengths (40λ , $12.8 \mu\text{s}$) for all window sizes. Based on these observations, we concluded that the precision of the attenuation estimates are independent of window size for window sizes greater than 2 pulse length (5λ , $1.6 \mu\text{s}$). This is attributed to the negligible changes in the spectrum due to gating effects for window sizes that are larger than 2 pulse length. We also concluded that ROI lengths greater than 16 pulse lengths (40λ , $12.8 \mu\text{s}$) are optimal for attenuation estimation. In the rest of the analysis, we used ROI lengths of 16 pulse lengths (40λ , $12.8 \mu\text{s}$) and window sizes of 2 pulse lengths (10λ , $3.2 \mu\text{s}$).

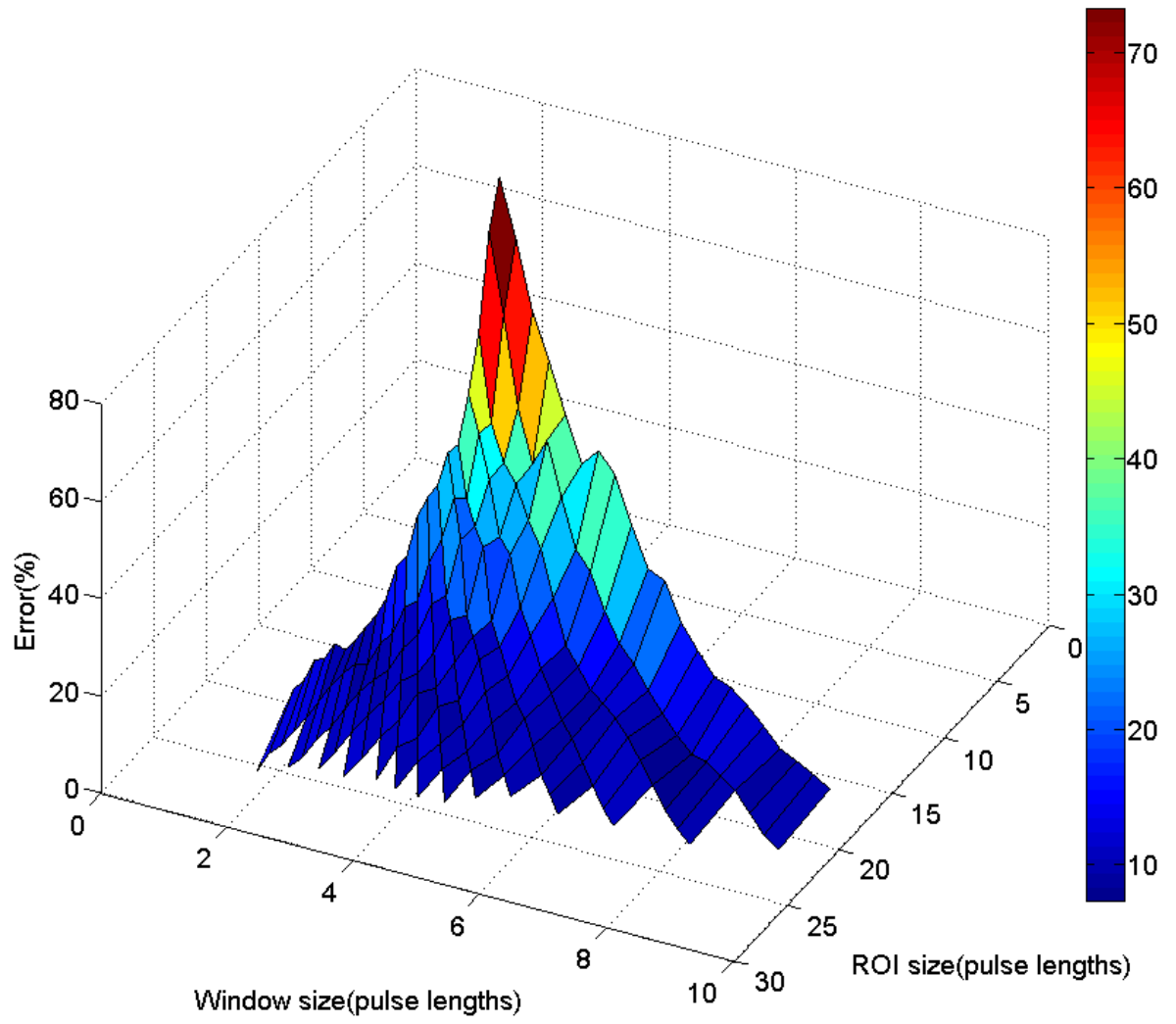


Figure 4 Surface plot of the mean of the error in the ACEs versus window size and ROI length

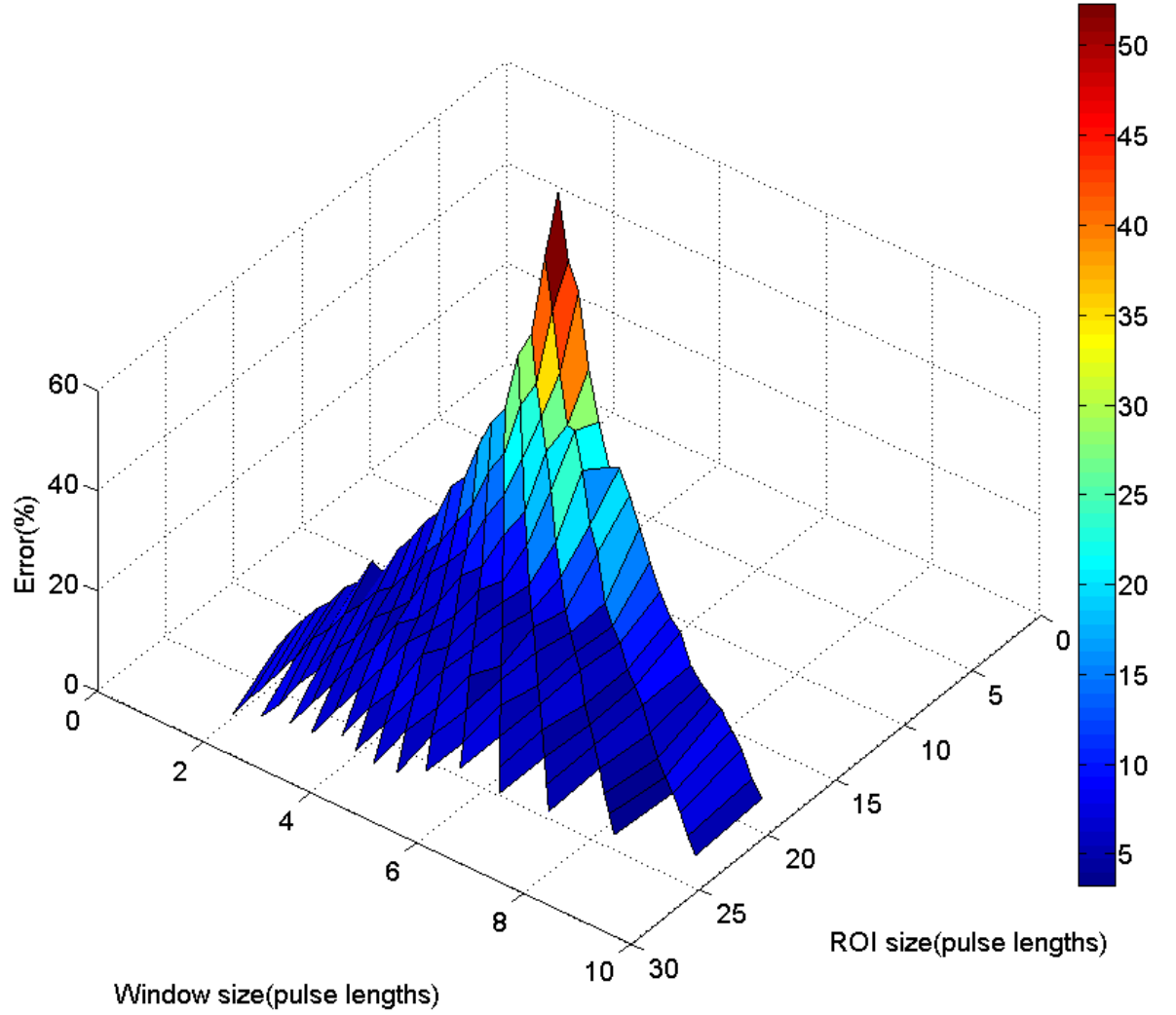


Figure 5 Surface plot of the STD of the percent error in the ACEs versus window size and ROI length

After determining the optimal ROI length, we determined the optimal number of echoes per ROI. For this analysis, we fixed the window size to 4 pulse lengths (10λ , $3.2 \mu\text{s}$) and the ROI length to 16 pulse lengths (40λ , $12.8 \mu\text{s}$) and varied the number of echoes per ROI from 1 to 46 independent echoes. For every choice of number of echoes per ROI, one ROI was selected from each B-mode image so that the center of the ROI corresponds to the

center of the B-mode image. The attenuation coefficient was estimated in the selected ROI of each data set, and the error in the estimates was calculated according to equation (2.4). For every choice of number of echoes per ROI, the mean and standard deviation of the errors in the ACEs of the nine ROIs were then calculated.

Figure 6 shows plots of the mean and STD of the errors in the ACEs with respect to the number of echoes per ROI. It is apparent that both the mean and the STD of the errors in the ACEs decrease with increasing number of echoes per ROI. However, there is no decrease in the mean and STD of the errors in the ACEs for ROIs that contain more than 10 independent echo lines. It is also observed that ROIs that contain 10 echo lines or more guarantee that the mean and STD of the errors in the ACEs are less than 12% and 8% respectively. Based on these observations, we concluded that ROIs that contain 10 independent echo lines or more are optimal for attenuation estimation.

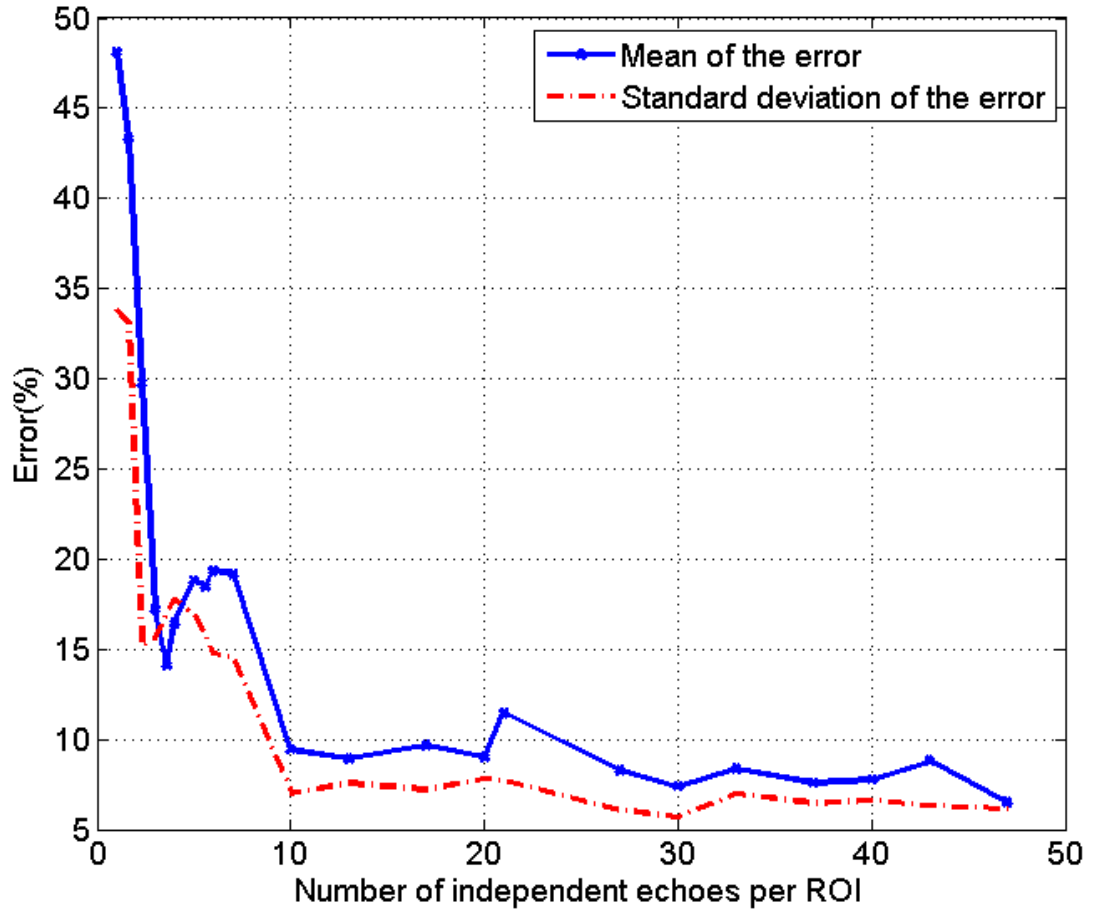


Figure 6 Plot of the mean and STD of the percent errors in the ACEs with respect the number of echoes per ROI

Using an ROI length of 16 pulse lengths (40λ , $12.8 \mu\text{s}$), a window size of 4 pulse lengths (10λ , $3.2 \mu\text{s}$), and 10 independent echo lines per ROI, the spectral difference algorithm was used to obtain an attenuation map in a B-mode image of phantom 1. To generate an attenuation map, a color is assigned to each value of attenuation, and the regions of the B-mode image are then colored according to their estimated value of attenuation. Figure 7 shows the resulting attenuation map. The mean and standard deviation of the

attenuation coefficient estimates of all ROIs in the B-mode image are 0.6437 dB/cm-MHz and 0.131 dB/cm-MHz, respectively (true attenuation coefficient = 0.64 dB/cm-MHz). We observed that the attenuation coefficients in the selected ROIs were estimated with high precision. Furthermore, the variance of the attenuation coefficient estimates across the B-mode image was small. Based on these observations, we concluded that the reference phantom algorithm can be used to estimate the attenuation throughout the entire field of view of a sample.

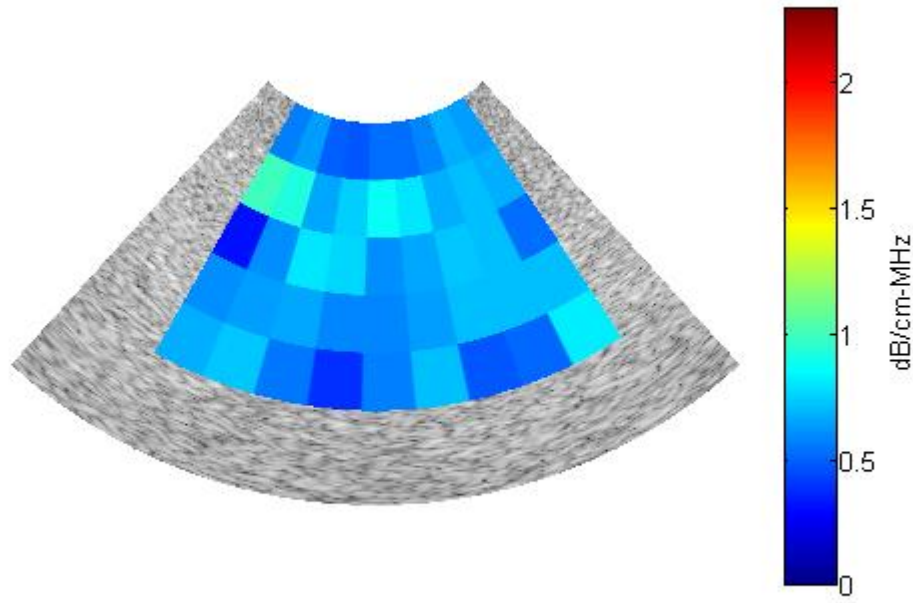


Figure 7 Attenuation map for a B-mode image from phantom 1 (0.64 dB/cm-MHz)

2.5 Results

Forty women participated in the study. Seven women delivered in less than 37 weeks gestation. Table 1 displays the characteristics of the women in the study.

Variable	All women Number = 40
Mean Maternal Age (range)	28 (19 – 42)
Gravidity, median (range)	2 (1-5)
History of preterm labor	7 (13%)
History of preterm delivery	7 (13%)
Mean gestation age at exam time(range)	22.5 (10-40)
Mean number of weeks to delivery (range)	14.6 (0-29)
Mean cervical length in cm (range)	3.7 (.6 -6.1)

Table 1 Characteristics of the 40 study participants by gestational age at the time of the cervical examination

The spectral difference method (described in Chapter 3) was used to estimate the local ultrasonic attenuation within each selected ROI of the patients' cervix images. The mean of the attenuation coefficient estimates of the selected ROIs in each patient image was chosen to be the attenuation value for that patient. All the ROIs were at least 16 pulse lengths long (40λ , $12.8\mu\text{s}$), and contain at least 10 independent echo lines. Figure 8 and Figure 9 show the B-mode image and the superimposed attenuation respectively, for the cervix of a pregnant patient with 38 weeks gestation. Figure 10 and Figure 11 show the B-mode image and the superimposed attenuation respectively, for the cervix of a pregnant patient with 14 weeks

gestation. In the two cases, the mean attenuation coefficient was greater in the 14 week (1.09 dB/cm-MHz) compared to the 38 week cervix (0.65 dB/cm-MHz).



Figure 8 B-mode image obtained from the cervix of a 14 week pregnant patient

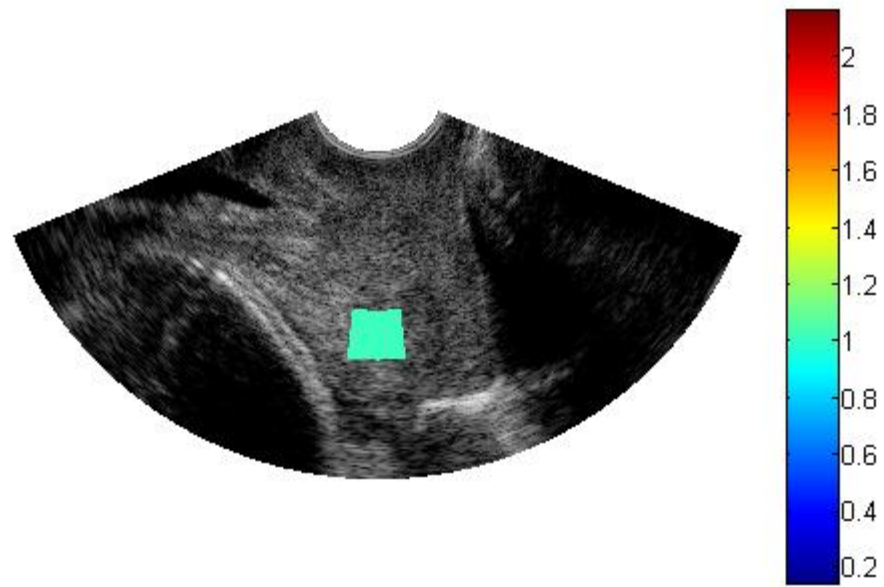


Figure 9 Superimposed attenuation estimate for the B-mode image obtained from the cervix of a 14 week pregnant patient



Figure 10 B-mode image obtained from the cervix of a 38 week pregnant patient

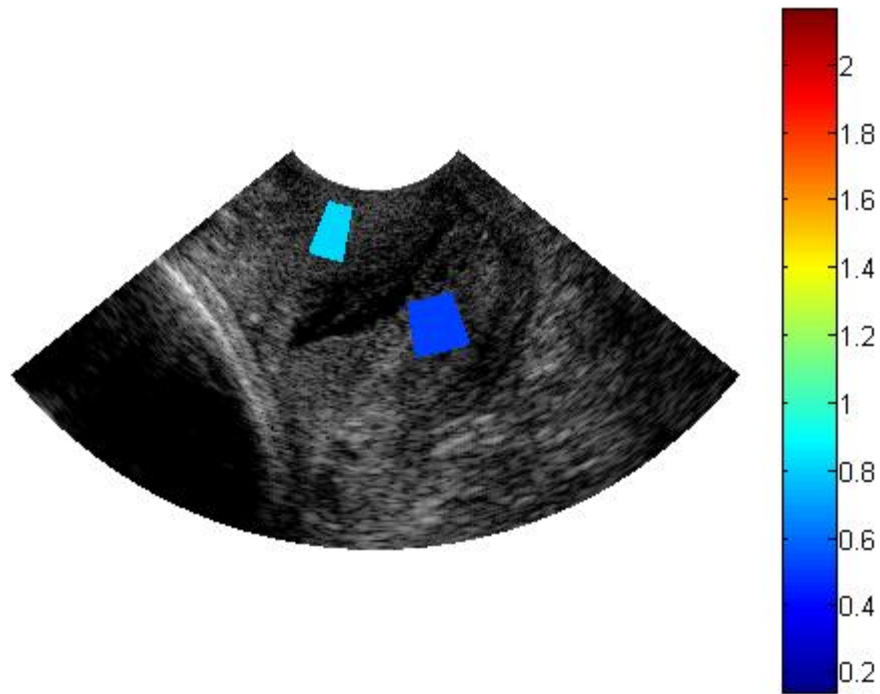


Figure 11 Superimposed attenuation for the B-mode image obtained from the cervix of a 38 week pregnant patient

Figure 12, Figure 13, and Figure 14 display scatter plot of the cervical attenuation coefficient estimates as a function of the number of weeks from ultrasonic examination to delivery, cervical length at the time of ultrasound examination, and gestation age at the time of ultrasound examination, respectively. The figures also show linear regression lines and 95 % confidence interval lines. One way analysis of variance (ANOVA) was performed to test the null hypotheses that there is no linear relationship between the attenuation coefficient estimates and: the number of weeks from ultrasonic examination to delivery, cervical length at the time of ultrasound examination, and gestation age at the time of ultrasound examination (i.e. the slope of the trend lines is equal to zero). A p values less than 0.05 is

considered significant. The analysis revealed that attenuation coefficients estimates were a predictor of the interval to delivery ($p = 0.011$), not a predictor of gestation age at time of examination ($p=0.15$), and not a predictor of cervical length ($p=0.65$). Figure 12 shows that although there is a large in-between patient variability, there is a relationship between the attenuation coefficient estimates and the interval to delivery, and that the results are statistically significant. The results of the relationship between the attenuation coefficient estimates and the cervix length, and the relationship between the attenuation coefficient estimate and gestation age are not statistically significant. However, Figure 13 and Figure 14 show that there is a trend for a decrease in the attenuation coefficient estimates with increasing gestation age and decreasing cervical length.

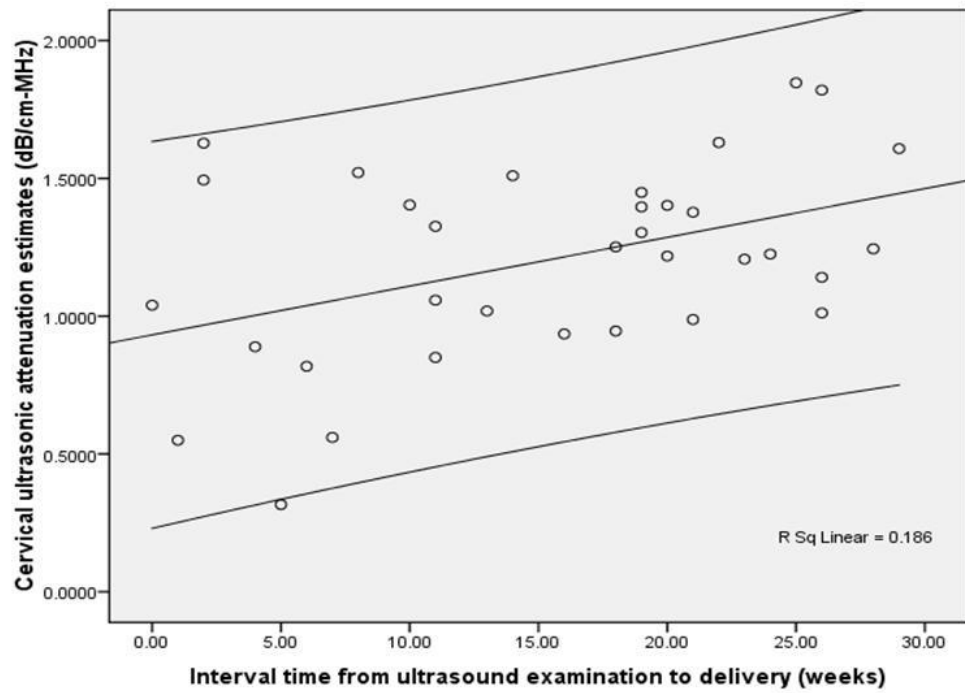


Figure 12 Scatter plot of the ultrasonic attenuation coefficient versus the interval time from the ultrasound examination to delivery

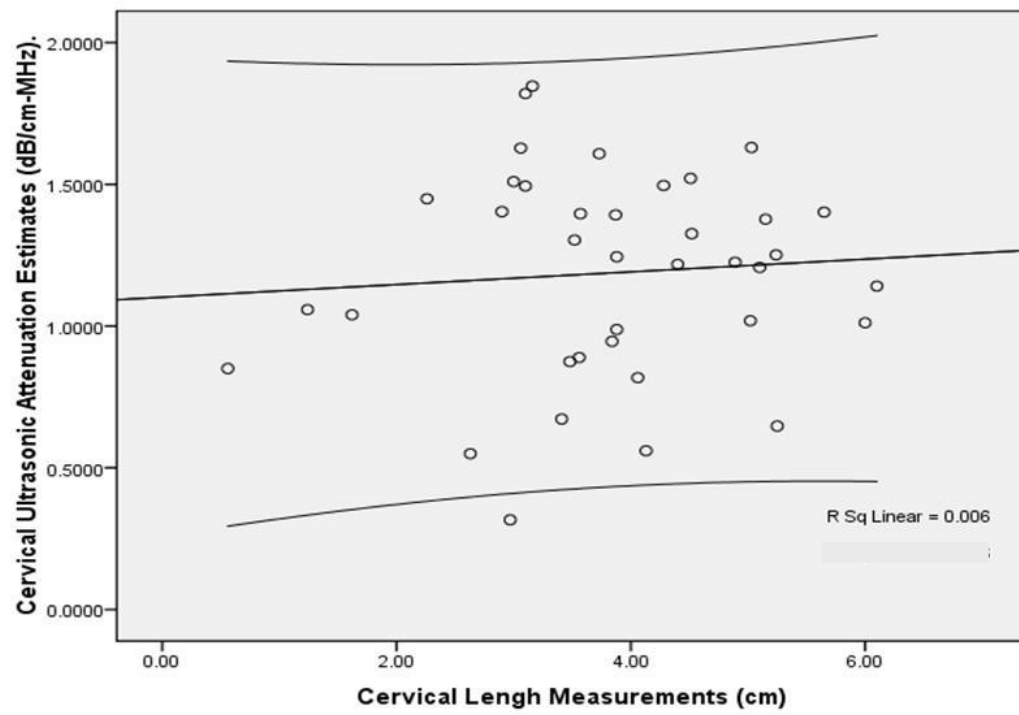


Figure 13 Scatter plot of the ultrasonic attenuation versus the cervical length at the ultrasound examination



Figure 14 Scatter plot of the ultrasonic attenuation versus the gestation age at the time of ultrasound examination

2.6 Discussion

The original goal of the research was to construct attenuation maps of the entire cervix or at least be consistent in sampling the internal and external portions of the cervix. However, because the spectral difference method requires that ROI to be homogeneous, only the ROIs that appeared homogeneous were selected. As a result, the same regions of the cervix were not compared in every patient and this may have increased the in-between subject variability. Furthermore, the under-sampling of the cervix is a major limitation because it does not allow different regions of the cervix to be analyzed. Different regions within the cervix may have

different tissue properties and different attenuation values. In order to obtain an attenuation map over the entire cervix, algorithms that are insensitive to variations in scattering properties within the ROI must be explored. Chapter 3 compares the accuracies and the limitations of three algorithms that are commonly used to estimate the attenuation coefficient based on a reference phantom.

The significant between subject variability in attenuation coefficient estimates could have also arisen from the biological variation in cervix tissue between different women. Previous rat experiments showed marked between subject variability. This suggests that a longitudinal study is required to detect changes in the attenuation coefficient estimates with increasing gestation on a patient specific basis as each patient may have her attenuation starting point.

Attenuation coefficient estimates alone may not be sufficient to detect changes in the cervix properties during cervical ripening. Other acoustic properties such as the backscatter coefficient, the scatterer number density, and the ratio of coherent to incoherent scattering intensity may be of interest. The backscatter coefficient has been shown to decrease with decreasing collagen concentration [35] and therefore the backscatter coefficient from the cervix may decrease as the cervix ripens and the collagen concentration decreases. The scatterer number density may decrease as the collagen fibril concentration decreases with increasing gestation. The collagen fibrils are highly organized at the beginning of pregnancy and they become more disorganized as the cervix ripens and prepares for delivery. This could lead to a lower ratio of coherent to incoherent scattering close to delivery compared to earlier stages of pregnancy. Estimating these parameters however, requires an algorithm for

estimating the total attenuation along the propagation path to the ROI. Two algorithms are proposed in this thesis and they are discussed in chapter 4.

3 COMPARISON OF LOCAL ATTENUATION ESTIMATION ALGORITHMS

3.1 Introduction

Accurate characterization of tissue pathologies using ultrasonic attenuation is strongly dependent on the accuracy of the algorithm that is used to obtain the attenuation coefficient estimates. One method for estimating the ultrasonic attenuation coefficient is the spectral shift technique [36-40]. This method assumes a Gaussian spectral shape of the propagating pulse and echo and estimates the attenuation coefficient slope by measuring the downshift in the center frequency with respect to depth. The downshift in the center frequency is caused by the higher attenuation of the high frequencies compared to the low frequencies. A number of time domain and frequency domain techniques were used to estimate the change in the center frequency with respect to depth. In the time domain, the number of sign changes per unit interval gives an estimate of the center frequency under the assumption of a narrow band signal [36-38]. In the frequency domain, the center frequency can be estimated by calculating the first moment of the power spectrum [41] or by fitting a Gaussian function to the spectrum and finding the mean frequency [40]. One disadvantage of the spectral shift method is that it does not normally correct for the effects of diffraction which leads to inaccurate estimates of the attenuation coefficient. While some corrections have been developed for spherically focused sources when the ROI is within the focal zone, these methods are challenging to implement in a clinical setting where array sources are used [40].

In order to correct for the diffraction effects, other methods for estimating the ultrasound attenuation coefficient have been developed. These methods use a tissue mimicking phantom (TMP) to obtain a reference power spectrum. The most common is the spectral difference

method which measures the decay of the power spectrum frequency components with respect to depth to estimate the attenuation coefficient as a function of frequency [22, 39, 41]. Another reference phantom technique is the spectral log difference method which assumes that the attenuation has a linear frequency dependence and obtains an estimate of the attenuation coefficient slope by calculating the slope of the straight line that fits the log ratio (difference between log spectra) of the two power spectra from the proximal and the distal segments of the region of interest (ROI) [23, 42-44]. The hybrid method is a recently developed technique that estimates the attenuation coefficient slope by measuring the downshift in the center frequency of the spectra that result from multiplying the power spectra, of windowed segments at various depths of the ROI, by a Gaussian filter [45]. The hybrid method and the spectral log difference method are theoretically not affected by variations in the backscatter that occur at boundaries.

In this chapter, we compare the accuracy and the precision of the spectral difference method, the spectral log difference method, and the hybrid which all use a tissue mimicking reference phantom to correct for the diffraction effects prior to estimating the ultrasonic attenuation. The three techniques have been used for estimating the attenuation in liver, kidney, cervix, rat tumors, etc... [1, 26, 34, 42, 43, 46]. The accuracy and the precision of these methods are strongly dependent on the ROI size (the number of independent echoes laterally and the number of pulse lengths axially) and on the level of homogeneity within the ROI. Previously, there has been no quantitative comparison of the minimum ROI size that is required for each method to obtain a specified accuracy and a specified precision in the attenuation coefficient estimates. Furthermore, the limitations of each technique have not been completely studied. Specifically, errors that result from in-homogeneities due to

differences in scatterer size have not been considered. In this study, we use computer simulations to generate ROIs that are homogeneous, ROIs that have the same scatterer size but different scatterer number densities, and ROIs that have the same scatterer number density but different scatterer sizes. The accuracy and precision of the three attenuation estimation techniques are then compared as a function of ROI size in all the simulation cases.

3.2 The spectral difference method

In order to estimate the ultrasonic attenuation in an ROI of a sample (material of interest), the same transducer and the same power settings are used to obtain backscattered signals from the tissue sample, and from a homogeneous TMP. The TMP has a known attenuation coefficient and a sound speed that closely matches the sound speed in soft tissue. Each RF echo line of the ROI is partitioned into several overlapping time gated windows. The Fourier Transform is applied to every window, and the power spectra of the windows that correspond to the same depth are averaged. The same procedure is performed on the region of the reference phantom that has the same compared depth as the ROI of the sample. In standard pulse echo imaging, the measured power spectrum of a windowed region in a statistically homogeneous tissue is given by [47]:

$$S_s(f, z) = P(f)D_s(f, z)A_s(f, z_0)B_s(f, z)e^{-4\alpha_s(f)z}$$

(3.1)

This equation assumes that the windows that are used to gate the echoes are small compared to the depth of focus of the transducer so that the variations of the field within each gated region could be ignored [27, 45]. The subscript s represents the sample. The distance from the surface of the transducer to the center of a particular time-gated window within the ROI

is denoted by z . The frequency is denoted by f . $P(f)$ represents the combined effect of the transmit pulse and the transducer sensitivity (electro-acoustic and acousto-electric transfer functions). $D_s(f, z)$ denotes the effects of diffraction that are related to the transducer geometry. $A_s(f, z_0)$ is the cumulative attenuation along the propagation path from the surface of the transducer to the depth z_0 which corresponds to the start of the ROI. $\alpha_s(f)$ is the attenuation coefficient within the ROI. $B_s(f, z)$ is a result of the scattering properties of the tissue within the gated window, namely the effective scatter size, the scatterer number density, and the mean square variation in acoustic impedance between the scatterers and the background. Similarly, the power spectrum of the backscattered signal from the reference phantom is

$$S_r(f, z) = P(f)D_r(f, z)A_r(f, z_0)B_r(f, z)e^{-4\alpha_r(f)z} \quad (3.2)$$

The subscript r represents the reference phantom. If the average sound speed in the TMP and in the tissue sample are assumed equal, the diffraction terms $D_s(f, z)$ and $D_r(f, z)$ are the same i.e.

$$D(f, z) = D_s(f, z) = D_r(f, z) \quad (3.3)$$

The spectral difference method makes a prior assumption that the tissue within the ROI is homogeneous and isotropic, i.e. the scattering term $B(f, z)$ doesn't vary with depth within the ROI, therefore:

$$\begin{aligned} B_s(f, z) &= B_s(f) \\ B_r(f, z) &= B_r(f) \end{aligned} \quad (3.4)$$

Dividing the power spectra of the sample by the power spectra of the reference phantom yields:

$$RS(f, z) = \frac{S_s(f, z)}{S_r(f, z)} = \frac{A_s(f, z_0)B_s(f, z)}{A_r(f, z_0)B_r(f, z)} \exp[4z\Delta\alpha(f)] \quad (3.5)$$

$$\text{where} \quad \Delta\alpha = [\alpha_r(f) - \alpha_s(f)] \quad (3.6)$$

Computing the natural logarithm yields:

$$\ln[RS(f, z)] = 4z\Delta\alpha(f) + \ln\left[\frac{A_s(f, z_0)B_s(f, z)}{A_r(f, z_0)B_r(f, z)}\right] \quad (3.7)$$

The attenuation coefficient of the sample (Np/cm) can be estimated at each frequency component by calculating γ , the slope of the straight line that fits the log ratio of the two spectra, i.e. the slope of the straight line that fits equation (3.7) versus depth. The estimated attenuation coefficient can be written as:

$$\alpha_s(f) = \alpha_r(f) - \frac{\gamma(f)}{4} \quad (3.8)$$

If the attenuation is assumed to increase linearly with frequency, then the attenuation coefficient slope (Np/cm-MHz) is used as a measure for the attenuation in the tissue of interest. The attenuation coefficient can be written as:

$$\alpha_s(f) = \beta f \quad (3.9)$$

where the single parameter β is the attenuation coefficient slope (Np/cm-MHz). $\alpha_s(f)$ can be estimated by finding the slope of the straight line that fits equation (3.9), or by dividing the attenuation coefficient by the frequency at each Fourier component and computing the average. Dividing by f and computing the average was the approach taken in our study.

3.3 The spectral log difference method

Unlike the spectral difference method which uses all the time gated windows within the ROI, the spectral log difference method uses the power spectra from only the proximal and the distal windows of the ROI. As in equation (3.5), dividing the power spectrum of the proximal window of the sample by the power spectrum of the proximal window of the TMP and computing the natural logarithm yields:

$$\ln \left[\frac{S_s(f, z_p)}{S_r(f, z_p)} \right] = \frac{e^{-4\alpha_s(f)z_p} B_s(f, z_p) A_s(f, z_0)}{e^{-4\alpha_r(f)z_p} B_r(f, z_p) A_r(f, z_0)} = 4z_p \Delta\alpha(f) + \ln \left[\frac{A_s(f, z_0) B_s(f, z_p)}{A_r(f, z_0) B_r(f, z_p)} \right] \quad (3.10)$$

The subscript p stands for proximal. z_p is the distance from the surface of the transducer to center of the proximal window of the ROI. Similarly, dividing the power spectrum of the distal window of the sample by the power spectrum of the distal window of the TMP and computing the natural logarithm yields:

$$\ln \left[\frac{S_s(f, z_d)}{S_r(f, z_d)} \right] = \frac{e^{-4\alpha_s(f)z_d} B_s(f, z_d)}{e^{-4\alpha_r(f)z_d} B_r(f, z_d)} = 4z_d \Delta\alpha(f) + \ln \left[\frac{A_s(f, z_0) B_s(f, z_d)}{A_r(f, z_0) B_r(f, z_d)} \right] \quad (3.11)$$

The subscript d stands for distal. z_d is the distance from the surface of the transducer to center of the distal window of the ROI. Computing the difference between the spectra from equations (3.10) and (3.11) yields:

$$S(f) = 4\Delta\alpha(z_p - z_d) + \ln \left[\frac{A_s(f, z_0) B_s(f, z_p)}{A_r(f, z_0) B_r(f, z_p)} \right] - \ln \left[\frac{A_s(f, z_0) B_s(f, z_d)}{A_r(f, z_0) B_r(f, z_d)} \right] \quad (3.12)$$

The TMP is homogeneous and isotropic, hence $B_r(f, z_p) = B_r(f, z_d)$. If the material within the proximal window has the same effective scatterer size as the material within distal window of the sample, we can write:

$$B_s(f, z_p) = c_s \times B_s(f, z_d) \quad (3.13)$$

where c_s is a multiplicative constant. Equation (3.13) is valid even if the material within the proximal window of the sample and the material within the distal window of the sample have different scatterer number densities and or different mean square variation in acoustic impedance between the scatterers and the background. Equation (3.12) becomes:

$$S(f) = 4\Delta\alpha(f)(z_p - z_d) + c \quad (3.14)$$

where c is a constant. The common parameterization of the attenuation coefficient is given by [36]:

$$\alpha_s(f) = \beta f^n \quad (3.15)$$

Equation (3.14) becomes:

$$S(f) = 4[\alpha_r(f) - \beta f^n](z_p - z_d) + c \quad (3.16)$$

The unknowns β , n , and c can be estimated by fitting a power function versus frequency to equation (3.16). If the attenuation is assumed to increase linearly with frequency as in equation (3.9), the attenuation coefficient slope can be estimated by fitting a straight line versus frequency to equation (3.16) which is the approach taken in this study.

3.4 The hybrid method

As in the spectral difference method, the hybrid method uses all of the time gated widows within the ROI. The hybrid method, as originally derived, makes a prior assumption that the local attenuation within the ROI and the cumulative attenuation, from the surface of the transducer to the depth that corresponds to the beginning of the ROI, increase linearly with frequency. Equations (3.1) and (3.2) become:

$$S_s(f, z) = P(f)D(f, z)B_s(f, z)e^{-4\beta_s f z}e^{-4\beta_{s-tot} f z_0} \quad (3.17)$$

$$S_r(f, z) = P(f)D(f, z)B_r(f, z)e^{-4\beta_r f z}e^{-4\beta_{r-tot} f z_0} \quad (3.18)$$

where β_{s-tot} and β_{r-tot} are the cumulative attenuation coefficient slopes of the sample and the reference, respectively. β_s and β_r are the local attenuation coefficient slopes within the ROIs of the sample and the reference, respectively. Dividing the power spectrum of the sample by the power spectrum of the reference yields:

$$RS(f, z) = \frac{S_s(f, z)}{S_r(f, z)} = \frac{B_s(f, z)}{B_r(f, z)} \exp[4f(z\Delta\beta + z_0\Delta\beta_{tot})] \quad (3.19)$$

where

$$\begin{aligned} \Delta\beta &= \beta_r - \beta_s \\ \Delta\beta_{tot} &= \beta_{r-tot} - \beta_{s-tot} \end{aligned} \quad (3.20)$$

The scattering term $B(f, z)$ is modeled as a power function of frequency and is expressed as an exponential form of the first two terms of the Taylor series expansion [45, 48]:

$$B(f) = cf^n \approx \exp\left[n\log(f_c) + n\log\left(1 + \frac{f - f_c}{f_c}\right)\right] \propto \exp\left[-\frac{n(f^2 - 4f_c f)}{2f_c^2}\right] \quad (3.21)$$

where c is a constant and f_c is the center frequency of the transmit pulse. Equation (3.19) becomes:

$$RS(f, z) \propto \exp\left[-\frac{(n_s - n_r)(f^2 - 4f_c f)}{2f_c^2}\right] \times \exp[4f(z\Delta\beta + z_0\Delta\beta_{tot})] \quad (3.22)$$

The subscripts s and r represent the sample and the reference, respectively. A Gaussian filter $G(f)$ with a center frequency f_c and a variance σ^2 is then applied to $RS(f, z)$. The Gaussian filtered intensity ratio is given by:

$$GRS(f, z) = G(f)RS(f, z) = \exp\left[-\frac{(f - f_c)^2}{2\sigma^2}\right] \exp\left[-\frac{(n_s - n_r)(f^2 - 4f_c f)}{2f_c^2}\right] \exp[4f(z\Delta\beta + z_0\Delta\beta_{tot})] \quad (3.23)$$

In the original implementation of the hybrid method, f_c was selected to be the center frequency of the transmit pulse and σ^2 was given by the bandwidth of the transmit pulse. However, we found a slight improvement in the accuracy of the algorithm when f_c was selected such that the frequency that corresponds to the spectral peak of $GRS(f, z)$ was in the middle of the usable frequency band. We also used the bandwidth of the received echoes from the unknown sample to set σ^2 as this only required processing the backscattered echo data. After manipulating equation (3.23), the center frequency of $GRS(f)$ at the depth z is given by:

$$f_c(z) = \frac{f_c + 4\sigma^2(\Delta\beta z + \Delta\beta_{tot} z_0) + \frac{\sigma^2(n_s - n_r)}{f_c^2}}{1 + \frac{\sigma^2(n_s - n_r)}{f_c^2}} \approx 4\sigma^2\Delta\beta z + (f_c + 4\sigma^2\Delta\beta_{tot} z_0) \quad (3.24)$$

The approximation $\frac{\sigma^2(n_s - n_r)}{f_c^2} \approx 0$ was made because the transmit center frequency is generally greater than the square root of the variance, and the parameter n for human tissue is

between 1 and 2. The attenuation coefficient slope of the sample is estimated by calculating the slope γ of the straight line that fits equation (3.24) versus depth. The estimated attenuation coefficient slope is given by:

$$\beta_s = \beta_r - \frac{\gamma}{4\sigma^2} \quad (\text{Np/cm-MHz}) \quad (3.25)$$

3.5 Simulation parameters and results

3.5.1 Simulation parameters

Computer simulations were used to obtain 4 different data sets of RF backscattered signals using a Gaussian focused beam with a 5 cm focal length, 10 MHz center frequency, 0.25 μs time pulse length (0.2 mm, 1.3 λ , see equation(2.2)), and a 50% -3 dB bandwidth. The first data set is obtained from a homogeneous region that has 10 μm radius spherical shell scatterers, and a scattering number density of 100 mm^{-3} . This data set was used to obtain the reference power spectrum. Spherical shell scatterers are used because most tissue mimicking phantoms consist of spherical glass bead scatterers imbedded in gelatin. The second data set is obtained from a homogeneous region which has 20 μm effective radius scatterers that have a Gaussian Form Factor, and a scattering density of 100 mm^{-3} . The third data is obtained from an inhomogeneous region which has 20 μm effective radius scatterers that have a Gaussian Form Factor and a 100 mm^{-3} scattering number density before the focal plane and a 200 mm^{-3} scattering number density beyond the focal plane axially. The fourth data set is obtained from an inhomogeneous sample which has a scattering number density of 100 mm^{-3} and scatterers that have a Gaussian Form Factor with a 20 μm effective radius before the focal plane and a 10 μm effective radius beyond the focal plane axially. The attenuation coefficients of the sample and the reference are 0.7 dB/cm-MHz and 0.5 dB-cm-

MHz, respectively. In the simulations, 3000 independent echo lines were generated for the sample data sets and 300 independent echo lines were generated for the reference data set. The focal plane was used as the center of the ROI. Each echo line within the ROI is gated using rectangular windows with 50% overlapping, each window containing 7 pulse lengths. We chose 7 pulse lengths in each time gated window because the full width half maximum (FWHM) bandwidth of the backscatter power spectrum doesn't change significantly for windows that contain more than 7 pulse lengths as shown in Figure 15.

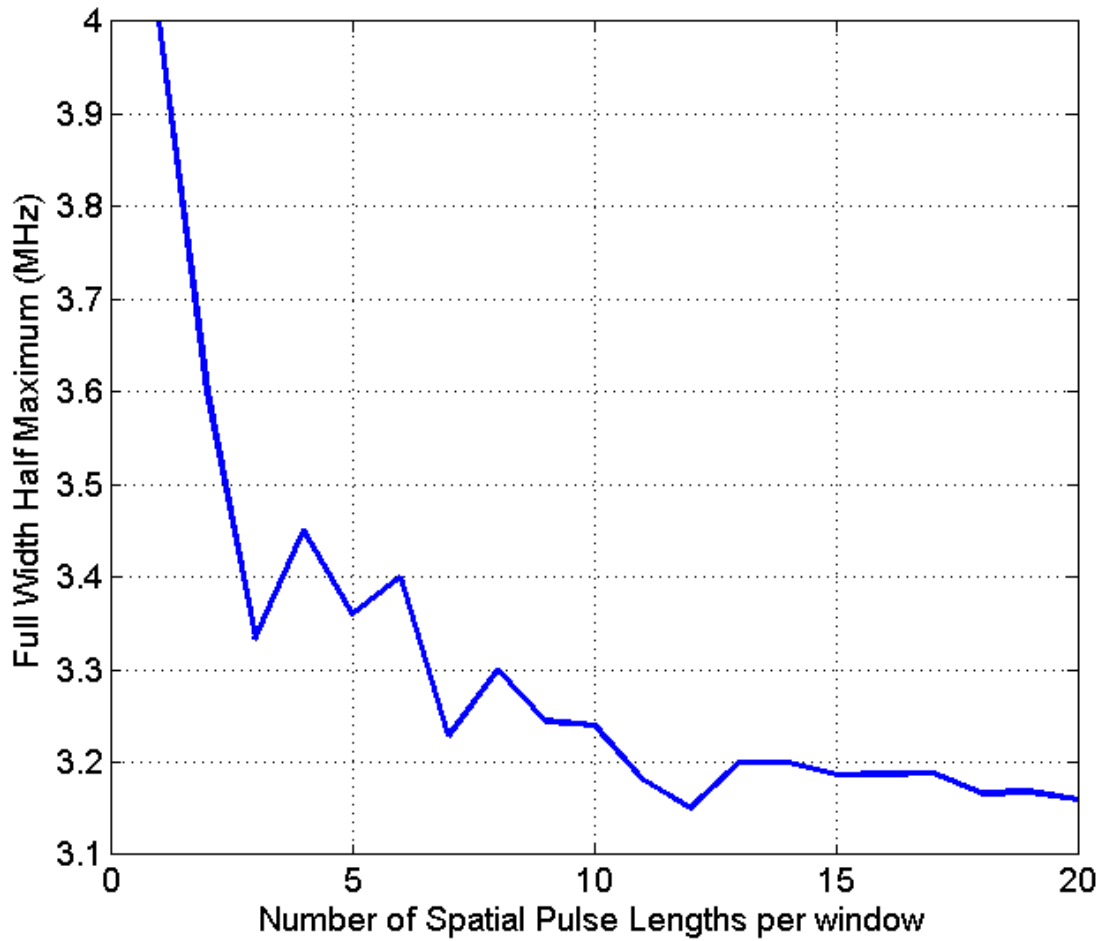


Figure 15 Plot of the Full Width Half Maximum bandwidth of the backscatter power spectrum of the reference phantom with respect to the size of the time gated windows in spatial pulse lengths

The power spectrum of each time gated window is approximated by taking the Fourier Transform of the RF data and squaring the magnitude of the result. The power spectra of the rectangular windows that correspond to the same depth are averaged. In order to operate above the noise floor, the usable frequency range was selected to be the frequencies common to the -20 dB bandwidths of the sample and the reference spectra. To find how the error in

the attenuation coefficient slope estimates (ACE) changes with respect to the ROI length axially and the ROI width laterally for the three sample cases that were simulated, we varied the length of the ROI from 2 overlapping rectangular windows to 9 overlapping rectangular windows (10.5 pulse lengths to 35 pulse lengths) and we varied the number of independent echoes per ROI from 5 to 100 with increments of 4 echo lines. We obtained 30 estimates for each combination using the three techniques. We then calculated the mean and STD of the percent in the ACEs. As mentioned earlier, we didn't calculate the MSE because our goal is to quantify the contribution of the bias and the contribution of the variance to the error in the ACEs, separately.

We varied the length of the ROI in terms of the number of pulse lengths instead of the number wavelengths because it was shown that the optimal ROI length depends on the number of pulse lengths per ROI and not on the center frequency of the transducer [49].

3.5.2 Homogeneous region of interest

The three attenuation estimation techniques were first tested on the RF data that is obtained from the homogeneous medium. Figure 16(a), Figure 17(a), and Figure 18(a) show the mean in the percent error of the ACEs that were obtained using the spectral difference method, the spectral log difference method, and the hybrid method respectively, versus the number of pulse lengths and the number of echoes per ROI. Figure 16(b), Figure 17(b), and Figure 18(b) show the standard deviation of the percent error in the ACEs that were obtained using the spectral difference method, the spectral log difference method, and the hybrid method, respectively, versus the number of pulse lengths and the number of echoes per ROI. Based on these plots, we observed that the mean and the standard deviation of the percent

error decrease with increasing ROI length axially and increasing number of echoes laterally for all the attenuation measurement techniques. The accuracy and the precision are higher in the spectral difference method, while they are comparable in the spectral log difference method and the hybrid method.

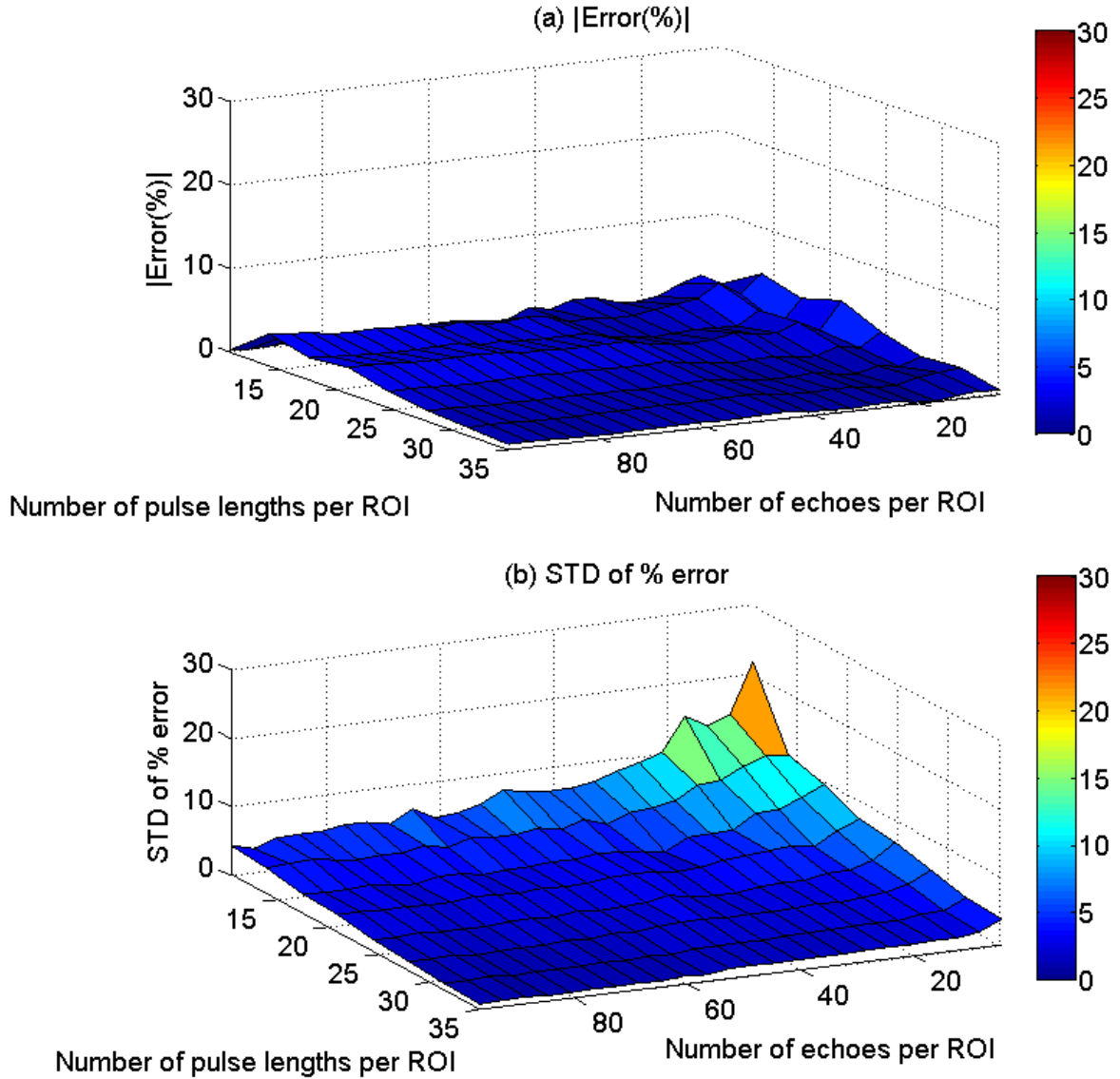


Figure 16 The mean (a) and (b) the standard deviation (STD) in the percent error of the attenuation coefficient estimates that were obtained using the spectral difference method

from the homogeneous sample, versus the number of pulse lengths and the number of echoes per ROI

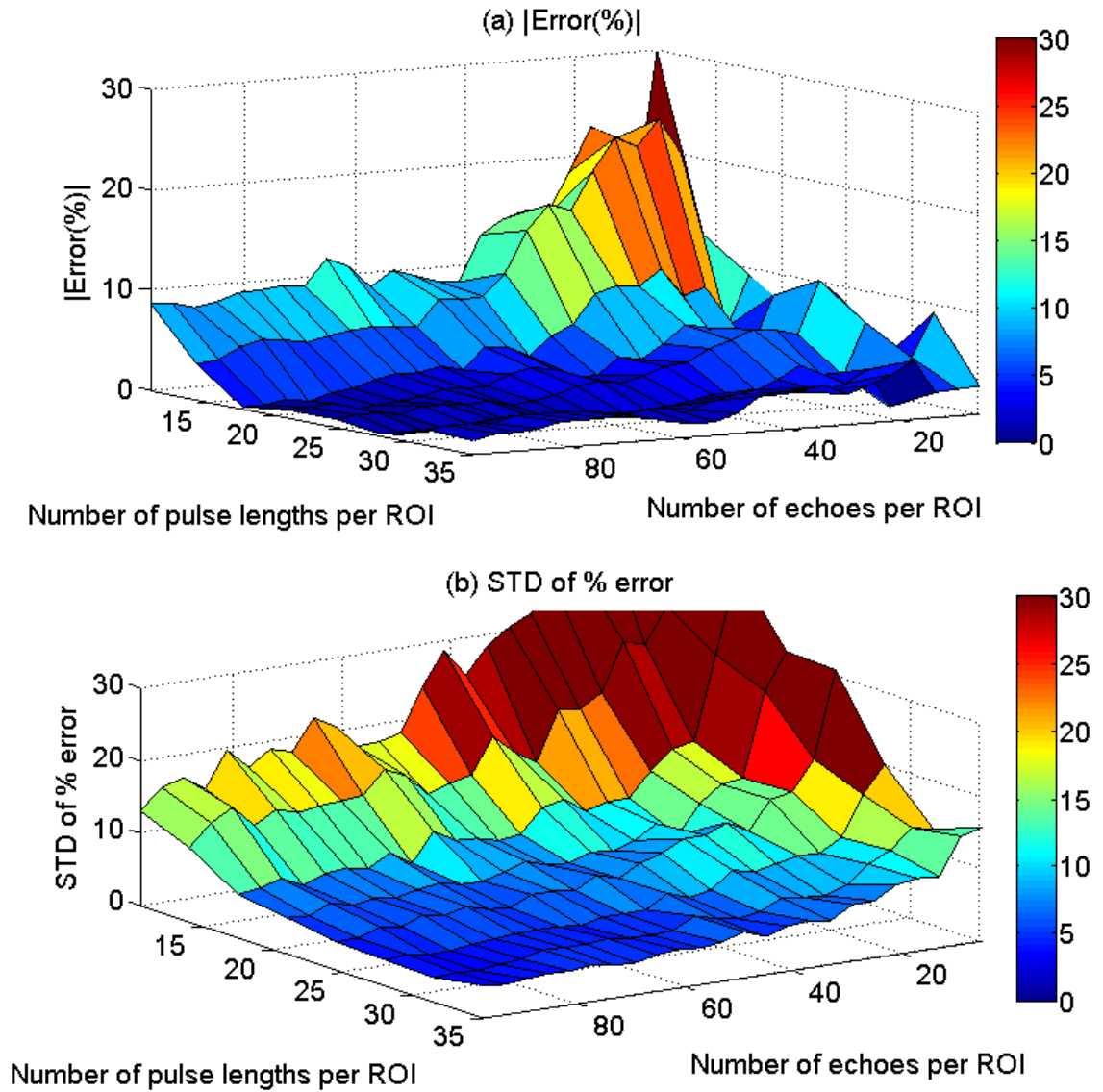


Figure 17 The mean (a) and (b) the standard deviation (STD) in the percent error of the attenuation coefficient estimates that were obtained using the spectral log difference method from the homogeneous sample, versus the number of pulse lengths and the number of echoes per ROI

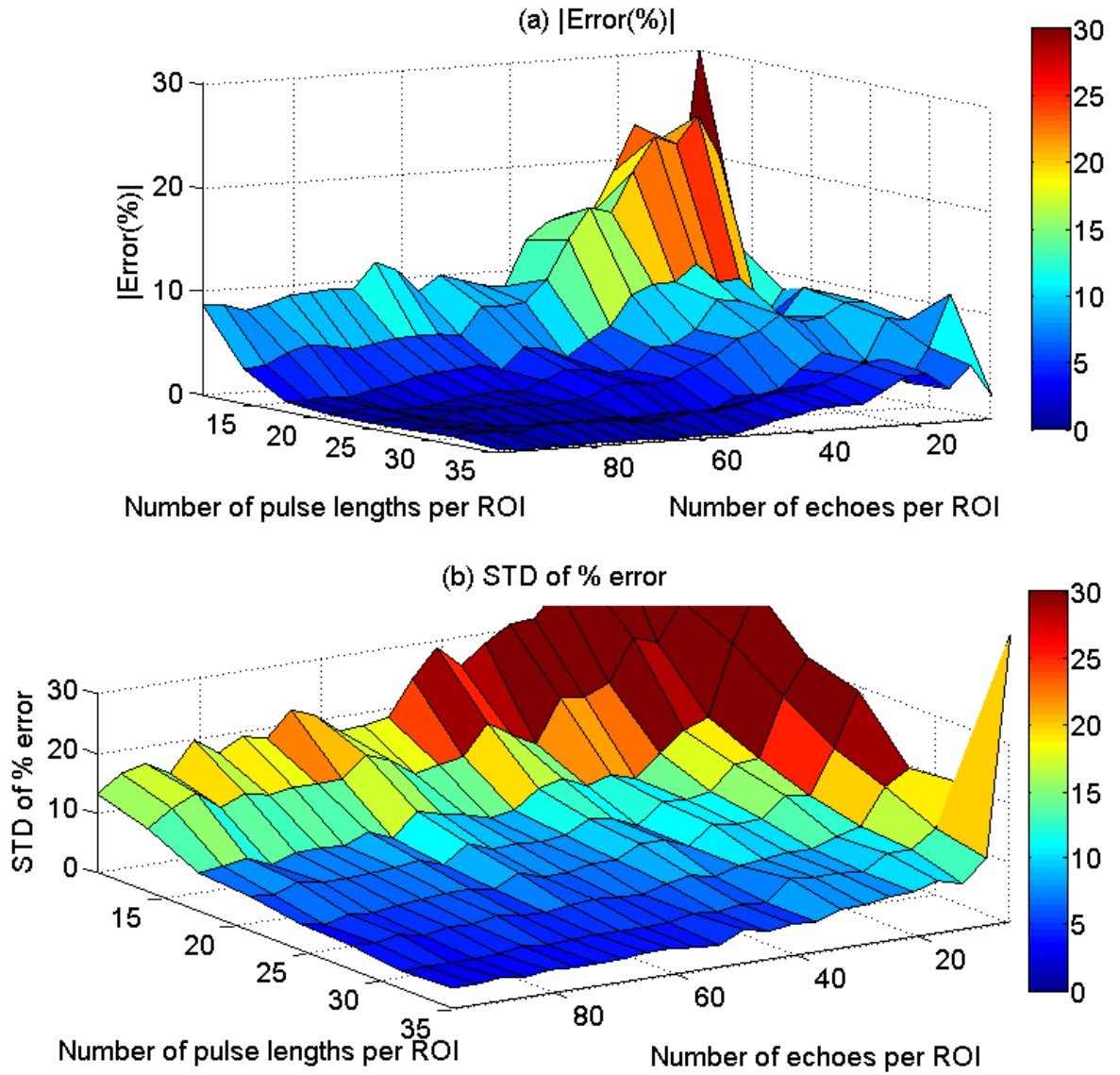


Figure 18 The mean (a) and (b) the standard deviation (STD) in the percent error of the attenuation coefficient estimates that were obtained using the hybrid method from the homogeneous sample, versus the number of pulse lengths and the number of echoes per ROI

3.5.3 In-homogeneous region of interest with varying scatterer number density

The three attenuation estimation techniques were then tested on the RF data that is obtained from the inhomogeneous medium with varying scatterer number densities. Figure 19(a), Figure 20(a), and Figure 21(a) show the mean in the percent error of the ACEs that were obtained using the spectral difference method, the spectral log difference method, and the hybrid method, respectively, versus the number of pulse lengths and the number of echoes per ROI. Figure 19(b), Figure 20(b), and Figure 21(b) show the standard deviation of the percent error in the ACEs that were obtained using the spectral difference method, the spectral log difference method, and the hybrid method, respectively, versus the number of pulse lengths and the number of echoes per ROI. Based on Figure 19(a), Figure 20(a), and Figure 21(a), the spectral difference method completely fails while the improved spectral log difference method and the hybrid method have comparable accuracy and precision. In both the spectral log difference method and the hybrid method, the accuracy and the precision increase with increasing ROI length and increasing ROI width (number of independent echoes per ROI).

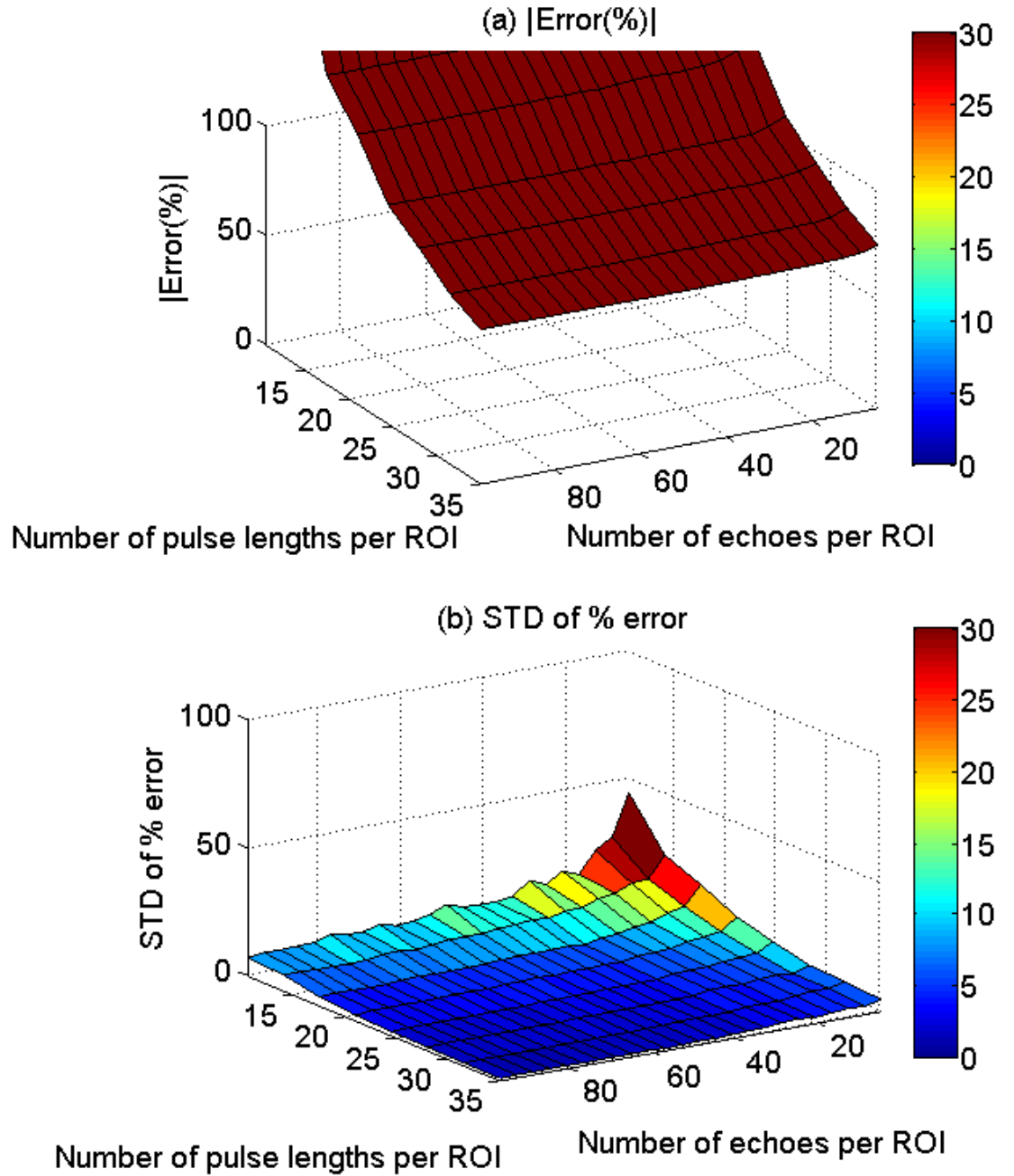


Figure 19 The mean (a) and (b) the standard deviation (STD) in the percent error of the attenuation coefficient estimates that were obtained using the spectral difference method from the inhomogeneous sample that has the same effective scatterer size but different scatterer number densities, versus the number of pulse lengths and the number of echoes per ROI

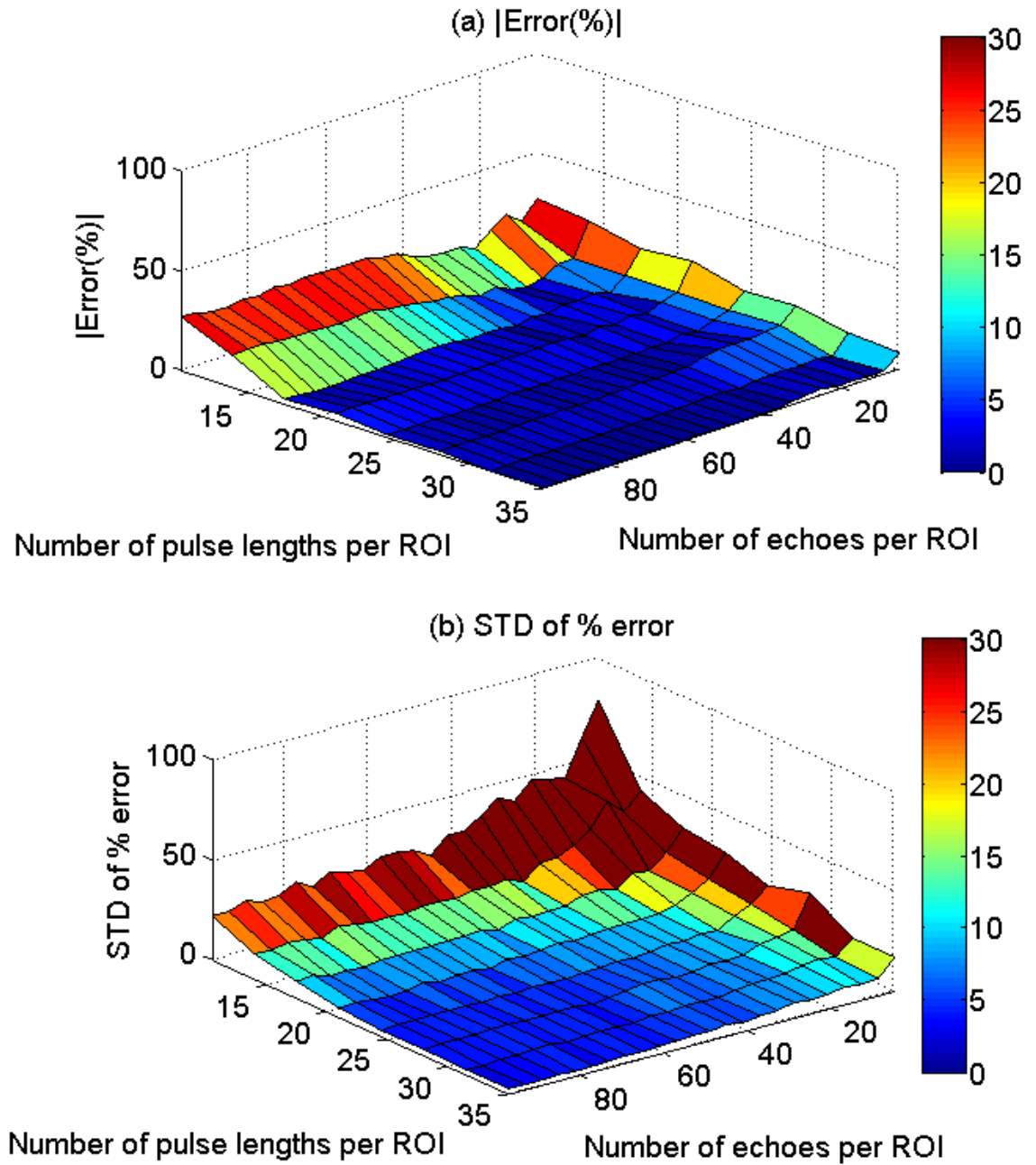


Figure 20 The mean (a) and (b) the standard deviation (STD) in the percent error of the attenuation coefficient estimates that were obtained using the spectral log difference method from the inhomogeneous sample that has the same effective scatterer size but different

scatterer number densities, versus the number of pulse lengths and the number of echoes per ROI

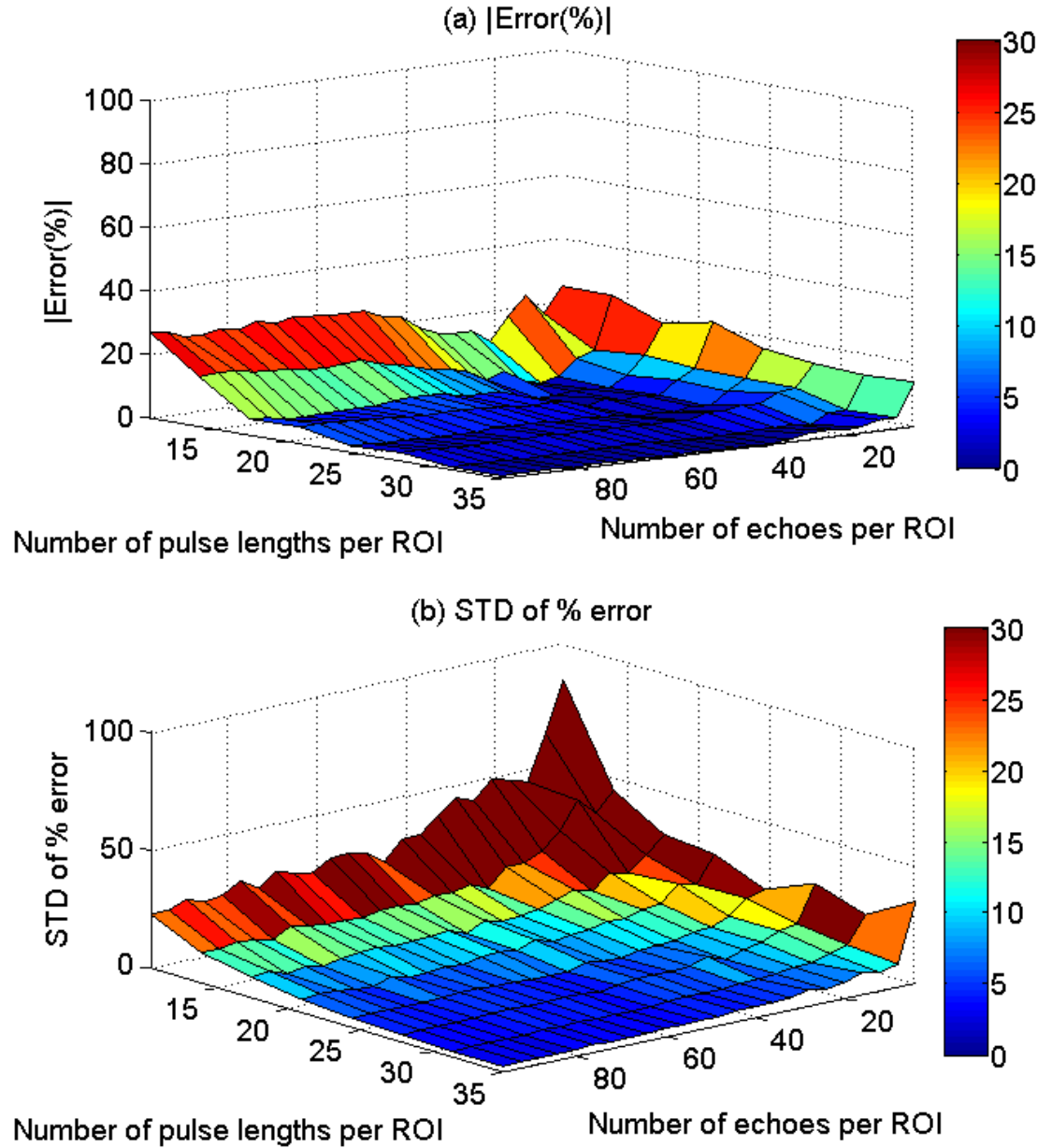


Figure 21 The mean (a) and (b) the standard deviation (STD) in the percent error of the attenuation coefficient estimates that were obtained using the hybrid method from the inhomogeneous sample that has the same effective scatterer size but different scatterer number densities, versus the number of pulse lengths and the number of echoes per ROI

3.5.4 Inhomogeneous region of interest with varying scatterer size

The three attenuation estimation techniques were then tested on the RF data that is obtained from the inhomogeneous medium with varying scatterer sizes. Figure 22 (a) and Figure 23(a) show the mean in the percent error of the ACEs that were obtained using the spectral log difference method, and the hybrid method, respectively, versus the number of pulse lengths and the number of echoes per ROI. Figure 22 (b) and Figure 23(b) show the standard deviation of the percent error in the ACEs that were obtained using the spectral log difference method, and the hybrid method, respectively, versus the number of pulse lengths and the number of echoes per ROI. The spectral difference method completely failed in estimating the local attenuation within the ROI, a result that was expected based on the assumptions that were taken when the algorithm was derived. For this reason, the mean and the standard deviation of the percent error in the ACEs wasn't plotted for the spectral difference method. Based on Figures 6 and 7, we observed that the spectral log difference method and the hybrid method didn't completely fail in estimating the attenuation; however, the accuracy and the precision are poor. The accuracy is within 25% for large ROI sizes in both methods. The precision in the ACEs increases with increasing number of echoes and increasing ROI length.

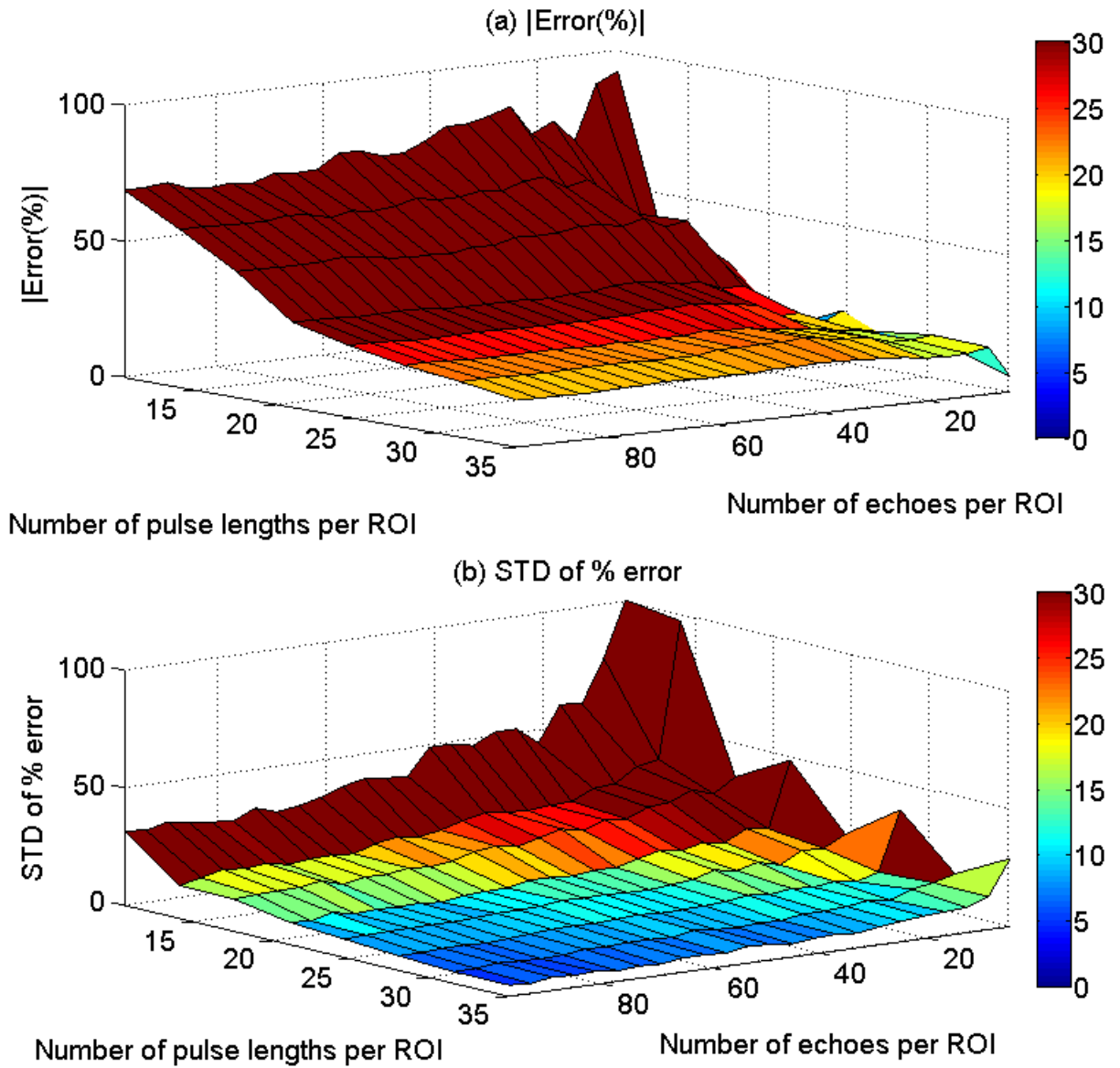


Figure 22 The mean (a) and (b) the standard deviation (STD) in the percent error of the attenuation coefficient estimates that were obtained using the spectral log difference method from the inhomogeneous sample that has the same scatterer number density but different effective scatterer size, versus the number of pulse lengths and the number of echoes per ROI

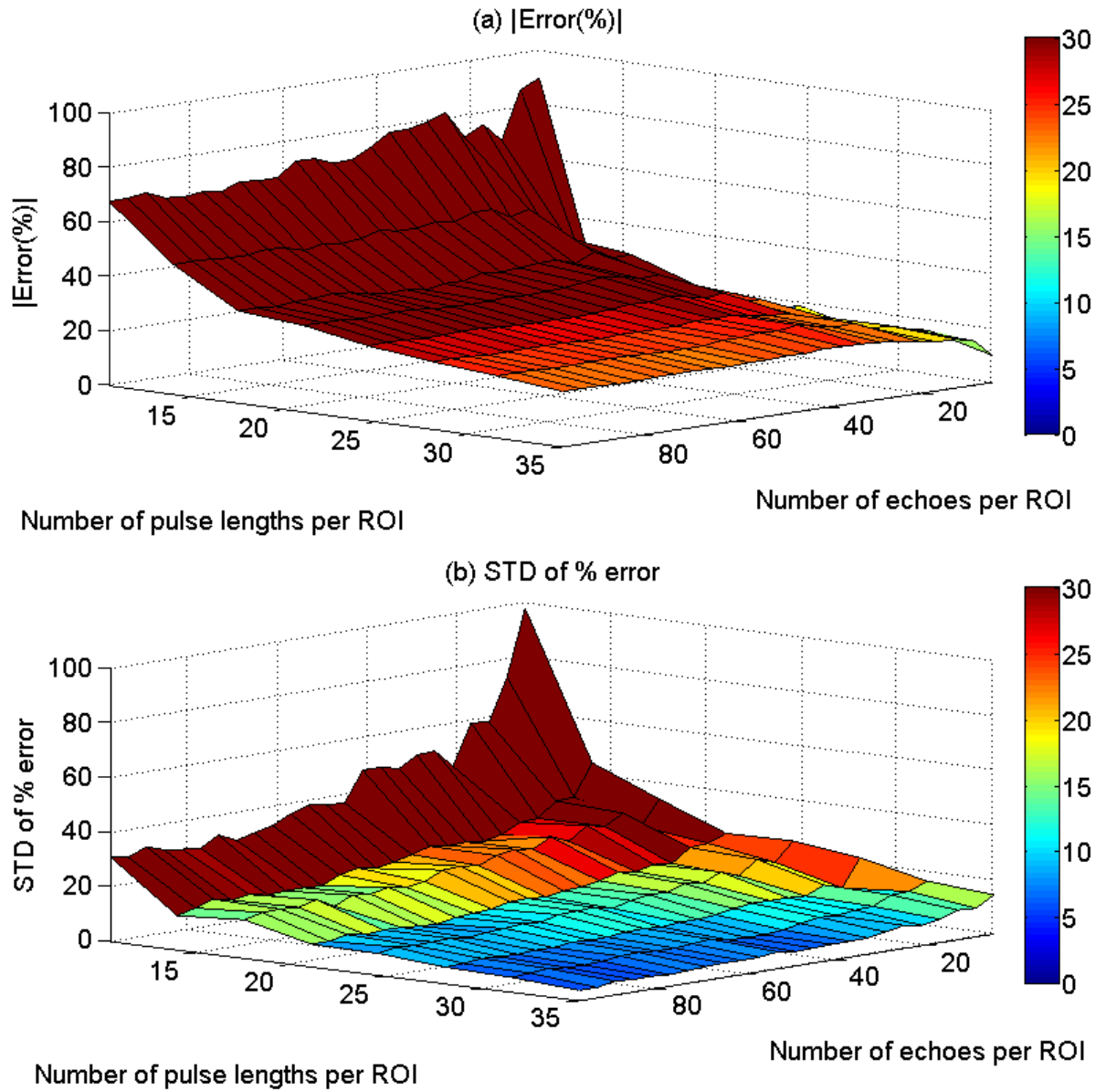


Figure 23 The mean (a) and (b) the standard deviation (STD) in the percent error of the attenuation coefficient estimates that were obtained using the hybrid method from the inhomogeneous sample that has the same scatterer number density but different effective scatterer size, versus the number of pulse lengths and the number of echoes per ROI

3.6 Tissue mimicking phantom results

We used a clinical array transducer (~ 5.5 MHz, L8-3 Linear Array Transducer) driven by a clinical ultrasound system (z.one Ultrasound System, ZONARE Medical Systems, Inc.) to obtain 10 RF data sets from a 0.7 dB/cm-MHz tissue mimicking phantom and 1 RF data set from 0.5 dB/cm-MHz tissue mimicking phantom. Each set has 250 echo lines. To determine the number of uncorrelated A-lines in the ROI, the correlation coefficient was measured among adjacent A-lines using equation (2.1). The correlation coefficient was less than 0.2 for every fourth A-line. Thus with a 20% criterion for de-correlation, we used every fourth A-line of the 250 echo lines obtained per data set. Using a hydrophone, we measured the time pulse length of the transducer to be approximately $0.8 \mu\text{s}$ as shown in Figure 24 (b). We also employed the correlation coefficient technique that was described in section 2.4 to measure the spatial pulse length of the transducer as shown in Figure 24 (a). Based on Figure 24 (a) and (b), the pulse length is approximately the time for which the absolute value of the correlation coefficient is above 0.2. The spatial pulse length can be calculated using equation (2.2) and is equal to 0.616 mm (2.2λ , $0.8 \mu\text{s}$).

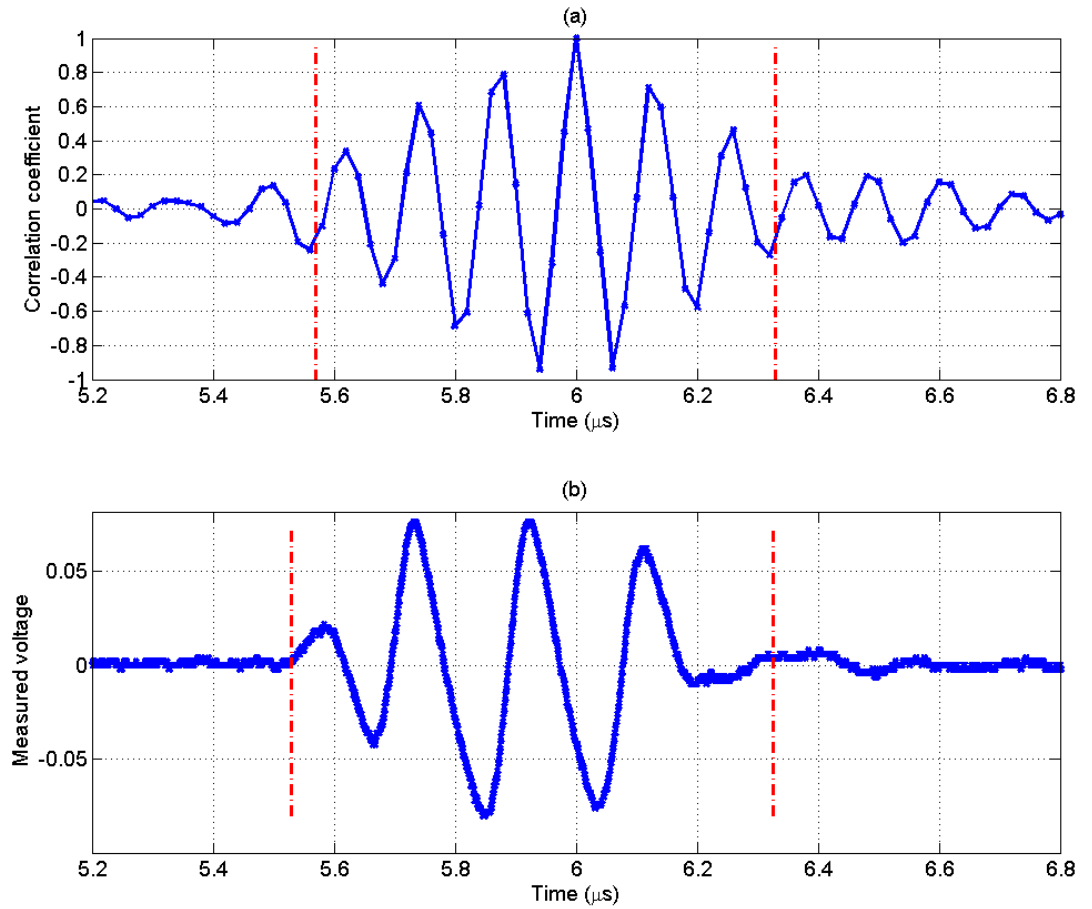


Figure 24 (a) The correlation coefficient of the time sample at 12 μs with the rest of the time samples of the RF echo lines of the reference phantom and (b) the hydrophone measured pulse length of the clinical array transducer

To find how the error in the attenuation coefficient estimates (ACEs) changes with respect to the ROI size and the number of independent echoes per ROI, we varied the size of the ROI from 2 overlapping rectangular windows to 9 overlapping rectangular windows (10.5 pulse lengths to 35 pulse lengths) and we varied the number of independent echoes per ROI from 5 to 59 with increments of 2 echo lines. We obtained 10 estimates for each combination using the three techniques. Figure 25 (a), Figure 26(a), and Figure 27(a) show

surface plots of the percent error of the mean in the ACEs that are obtained using the spectral difference method, the modified spectral log difference method and the hybrid method respectively, versus the number of pulse lengths and number of echoes per ROI. Figure 25 (b), Figure 26(b), and Figure 27(b) show surface plots of the percent error of the standard deviation in the ACEs that are obtained using the spectral difference method, the modified spectral log difference method and the hybrid method respectively, versus the number of pulse lengths and the number of echoes per ROI. Based on these plots, we observed that the percent error in the mean decreases with increasing ROI size. The percent error in the standard deviation decreases with increasing ROI size and increasing number of echoes per ROI for all attenuation measurement techniques. The accuracy and precision is higher in the spectral difference method, followed by the modified spectral log difference method and the hybrid method respectively. Furthermore, the spectral difference method doesn't require large ROI sizes or large number of echoes per ROI to obtain highly accurate and precise estimates. Based on these results, we concluded that the spectral difference method will be optimal for use in the future longitudinal study of the pregnant patient cervix data. Using small ROIs within the cervix, the spectral difference method can be used to obtain an attenuation map of the entire cervix. Each individual small ROI within the cervix can assumed homogeneous, even though the cervix may be heterogeneous as a whole.

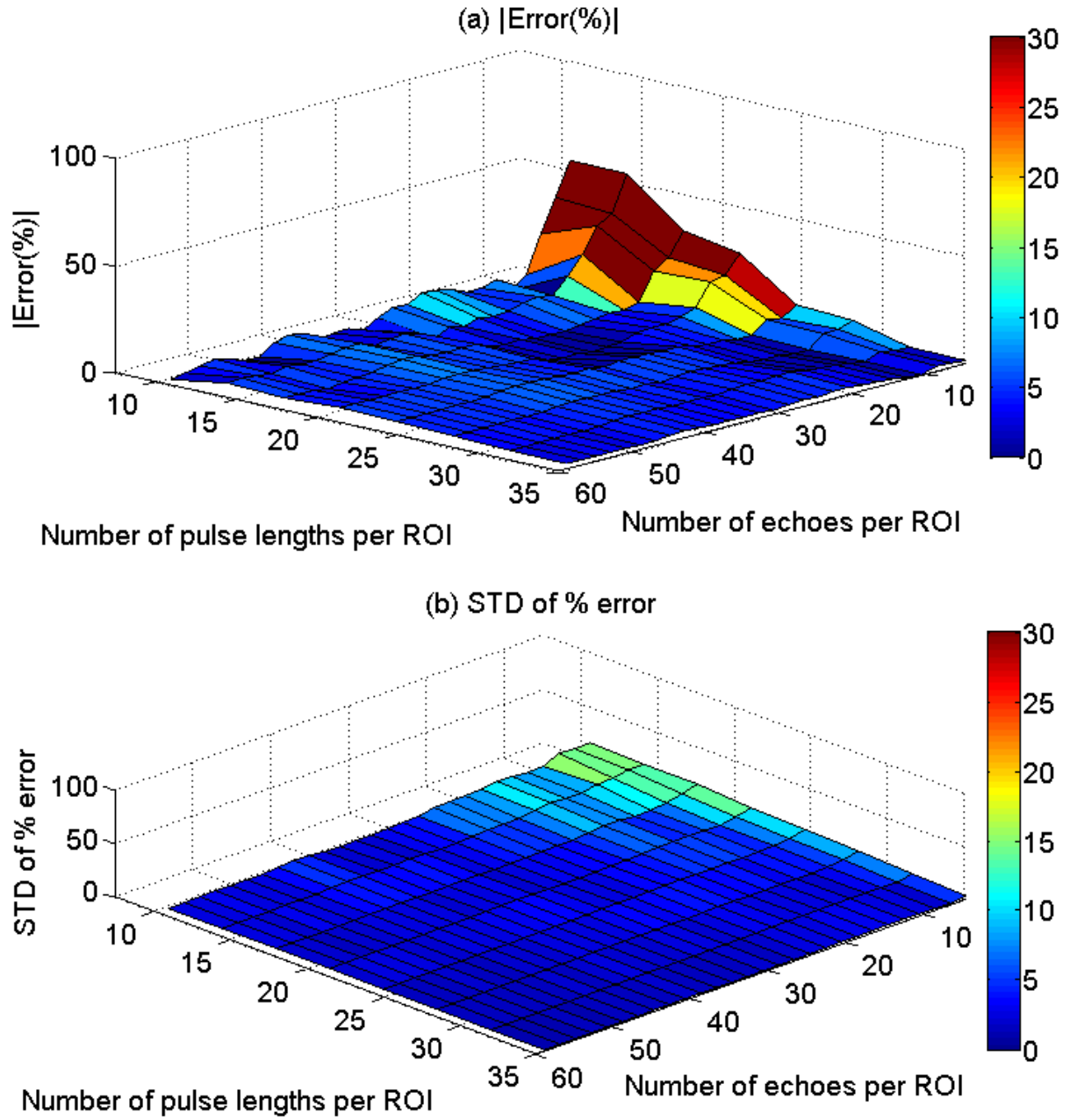


Figure 25 Plot of percent error in the mean of attenuation slope versus the number of independent echoes and number of pulse lengths per ROI for the spectral difference method

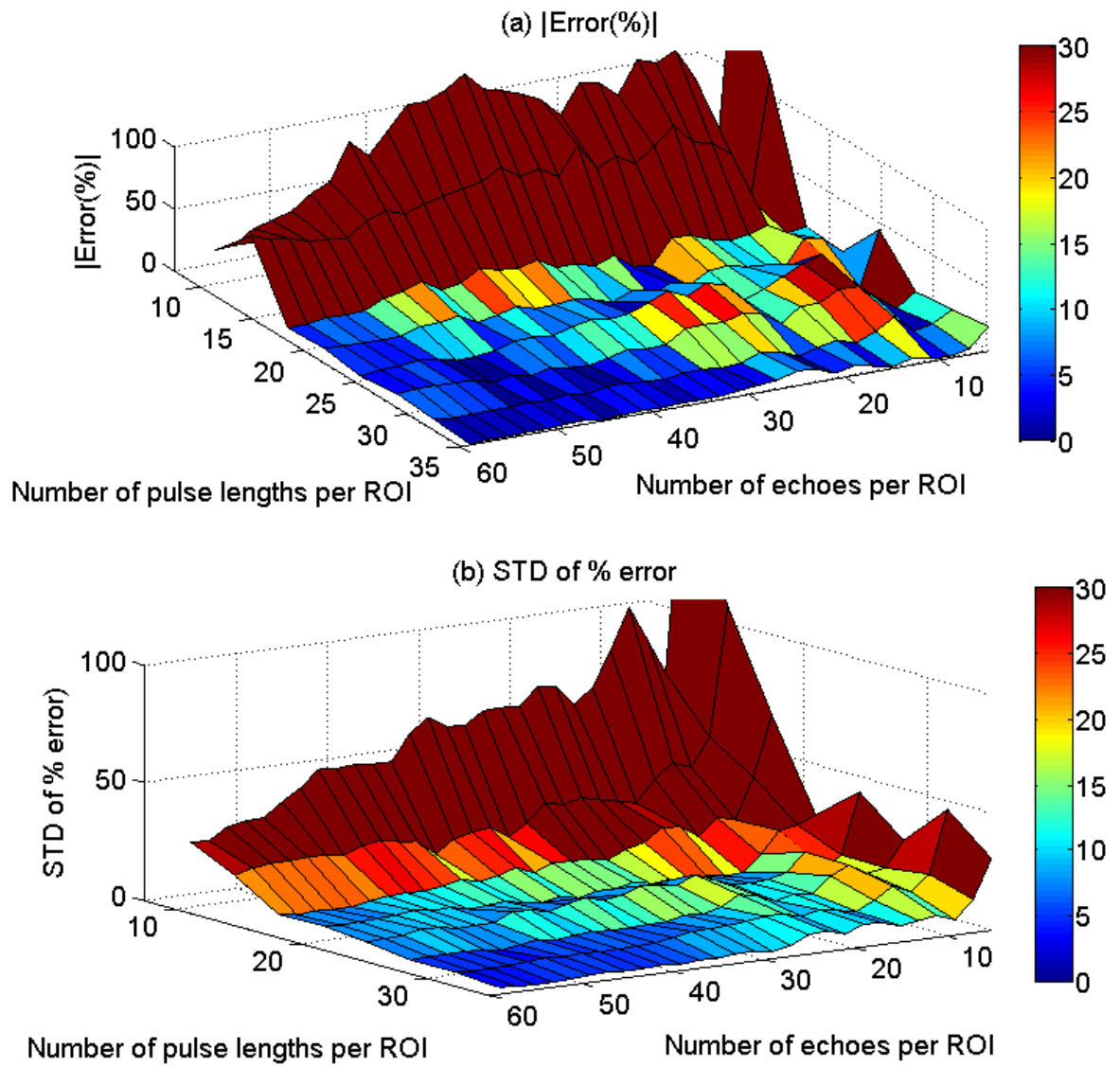


Figure 26 Plot of percent error in the mean of attenuation slope versus the number of independent echoes and number of pulse lengths per ROI for the spectral log difference method

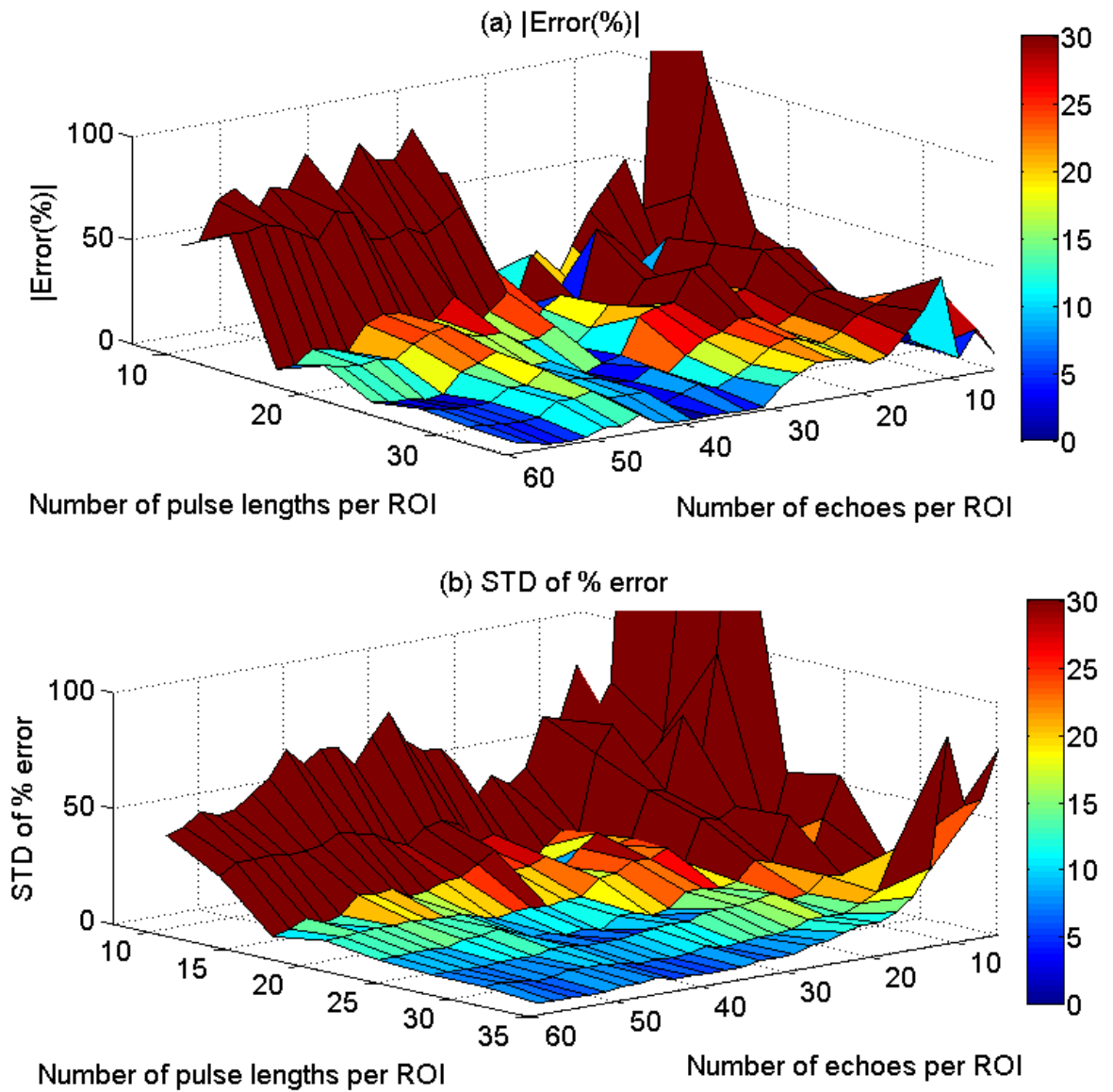


Figure 27 Plot of percent error in the mean of attenuation slope versus the number of independent echoes and number of pulse lengths per ROI for the hybrid method

3.7 Discussion

Based on the above results, the spectral difference method gave accurate attenuation coefficient estimates when the tissue was homogeneous, however it failed completely when the scatterer number densities and or the effective scatterer radii are different within the ROI. These results were expected from the derivation of the algorithm. The spectral log difference method and the hybrid method gave accurate attenuation estimates when the ROI was homogeneous, and when the ROI had the same scatterer size but different scatter number densities, with both methods having a comparable accuracy and precision. However, because there was no correction for variations in the scatterer size during the derivation of the two algorithms, it was surprising that these two methods gave only a 25% error when the ROI had the same scatterer number densities but different effective scatterer size.

In order to quantify how the error in the ACEs depends on the variations in the scatterer size within the ROI, we modeled the backscatter coefficient $B(f, z)$ with a Gaussian scattering model [50] and re-derived the spectral log difference method and the hybrid method. The term $B_s(f, z)$ in equations (3.12) and (3.17) can be written as:

$$B(f, z) = M(z) f^4 \exp\left(-\frac{32.6496 a_{eff}^2(z) f^2}{c^2}\right) \quad (3.26)$$

where $M(z)$ is a function of the scatterer number density and mean square variation in acoustic impedance, a_{eff} is the effective scatter radius, and c is the average sound speed. In the spectral log difference method, equation (3.12) becomes:

$$S(f) = 4f\Delta\beta\Delta z - \frac{32.649f^2\Delta a_{eff}^2}{c^2} + const \quad (3.27)$$

where, $\Delta\beta = (\beta_r - \beta_s)$, $\Delta z = (z_p - z_d)$, and $\Delta a_{eff}^2 = [a_{eff-s-p}^2(z) - a_{eff-s-d}^2(z)]$, the subscripts s and r denote the sample and the reference, respectively. p and d stand for proximal and distal, respectively. Taking the derivative of $S(f)$ with respect to frequency, we obtain:

$$\frac{\delta}{\delta f} S(f) = 4\Delta\beta\Delta z - \frac{65.298f\Delta a_{eff}^2}{c^2} \quad (3.28)$$

If we approximate the frequency f by the middle frequency of the usable frequency range f_{mid} , we find that the estimated attenuation coefficient slope of the sample is given by:

$$\beta_s \cong \beta_s + \frac{\overbrace{16.32f_{mid}\Delta a_{eff}^2}^{Error \ Term}}{c^2\Delta z} \quad (3.29)$$

Equation (3.29) shows that the error in the attenuation coefficient slope of the sample increases with increasing scatterer size difference between the proximal and distal windows of the ROI, and decreases with increasing range between the proximal and distal windows of the ROI.

Similarly, in the hybrid method, equation (3.23) becomes:

$$GRS(f, z) = \frac{S_s(f, z)}{S_r(f, z)} = \exp\left[-\frac{(f - f_c)^2}{2\sigma^2}\right] \left[\frac{M_s(z)}{M_r(z)}\right] \exp\left\{-\frac{5.19f^2[a_{eff-s}^2(z) - a_{eff-r}^2(z)]}{c}\right\} \exp[4z\Delta\beta f] \quad (3.30)$$

After manipulating equation (3.30), it was shown that center frequency of $GRS(f)$ at the depth z can be expressed as [49]:

$$f_c(z) = -4z\Delta\beta\sigma^2 + f_c \left\{ 1 + \frac{65.298}{c^2} \sigma^2 [a_{eff-s}^2(z) - a_{eff-r}^2(z)] \right\} \quad (3.31)$$

where

$$\sigma^2 = \sigma^2 \left\{ 1 + \frac{65.298}{c^2} \sigma^2 [a_{eff-s}^2(z) - a_{eff-r}^2(z)] \right\} \cong \sigma^2 \quad (3.32)$$

In the hybrid method, $\Delta\beta$ is estimated by dividing the slope the straight line that fits equation (3.31) with respect to depth. However, if we take the derivative of $f_c(z)$ with respect to depth, we obtain:

$$\begin{aligned} \frac{\delta}{\delta z} f_c(z) = \\ -4\Delta\beta\sigma^2 + \frac{65.298f_c\sigma^2}{c^2} \frac{\delta}{\delta z} [a_{eff-s}^2(z) - a_{eff-r}^2(z)] = -4\Delta\beta\sigma^2 + \frac{65.298f_c\sigma^2}{c^2} \frac{\delta}{\delta z} a_{eff-s}^2(z) \end{aligned} \quad (3.33)$$

If we approximate $\frac{\delta}{\delta z} a_{eff-s}^2(z)$ by $\frac{[a_{eff-s-p}^2(z) - a_{eff-s-d}^2(z)]}{(z_p - z_d)} = \frac{\Delta a_{eff}^2}{\Delta z}$, we find that the

estimated attenuation coefficient slope of the sample is given by:

$$\beta \cong \beta_s + \overbrace{\frac{16.32f_c\Delta a_{eff}^2}{c^2\Delta z}}^{\text{Error Term}} \quad (3.34)$$

Equations (3.34) and (3.29) show that the error in the attenuation coefficient slope of the sample is very similar between the hybrid method and the spectral log difference method. To test the expressions given by equations (3.29) and (3.34) for the difference in scatterer size, 4

cases were simulated using an ROI that contains 35 pulse lengths in the axial direction and 100 independent echo lines in the lateral direction. The first case (Case 1 in Figure 23) was a homogeneous sample which had 20 μm effective radius scatterers that have a Gaussian Form Factor, and a scattering density of 100 mm^{-3} . The second case (Case 2 in Figure 23) was an inhomogeneous sample which had scatterers that have a Gaussian Form Factor and 20 μm effective radii before the focal plane and 10 μm effective radii beyond the focal plane axially. The third case (Case 3 in Figure 23) was an inhomogeneous sample which had scatterers that have Gaussian Form Factor and 40 μm effective radii before the focal plane and 10 μm effective radii beyond the focal plane axially. The fourth case (Case 4 in Figure 23) was an inhomogeneous sample which had scatterers that have a Gaussian Form Factor and 60 μm effective radii before the focal plane and 10 μm effective radii beyond the focal plane axially. Figure 28 shows the expected percent error and the measured percent error in the attenuation coefficient slope estimate that is obtained using the hybrid method and the modified spectral log difference method for the four cases. We observe that the percent error in the attenuation estimate increases with increasing difference of scatterer size between the top half and bottom half of the ROI. Also, the expected error and measured error are comparable in both the hybrid and the modified spectral log difference method confirming our derived error terms in equation (3.29) and (3.34).

The main goal of this chapter was to test whether the three attenuation estimation methods are sensitive to variations in backscatter within the ROI. For this reason, we only used a simple step function for varying the backscatter properties within the ROI. Depending on the tissue of interest, the in-homogeneities can take many different forms. Therefore in

order to obtain a quantitative measure of the error in the attenuation coefficient estimates using each method, tissue specific models for variations in backscatter should be used.

The results of this chapter demonstrate that in order to obtain a specific accuracy and precision in the ACEs for homogeneous ROIs, the spectral difference method requires much smaller ROIs compared to the spectral log difference or the hybrid method. The spectral difference method however, fails when there are variations in scatterer number density or scatterer size within the ROI. The hybrid method and the spectral log difference method only fail when there exists variation in scatter size within the ROI. In real tissue however, a change in scatterer number density is usually accompanied by a change in the scatterer size. Therefore, in inhomogeneous tissue, the hybrid method and the spectral log difference method are also expected to yield errors in the ACEs. This error however, will not be as significant as that obtained using the spectral difference method especially if the ROI is large and the variations in the scatterer size within the ROI are not large. One way to minimize the bias in the ACEs (on the expense of large variance) is to divide the region of interest in tissue into multiple smaller sub-ROIs. These ROIs could be assumed homogeneous, and the spectral difference method can be used to estimate the attenuation coefficient within each sub-ROI. The mean of the estimates should approximate the attenuation coefficient of the original ROI. The variance of the estimates however, will be high because the sub-ROIs are small.

In the study of the pregnant patient cervix data (chapter 2), we selected what appeared to be homogeneous ROIs (reasonably large ROIs) and obtained an attenuation coefficient using the spectral difference method. This however yielded a large variance in the estimates of different regions of the cervix for the same patient. Although it is possible that different

regions in the cervix tissue have different attenuation values, it is unlikely that the difference in the attenuation between the different regions is high. Therefore, the high variance in the attenuation estimates of different regions in the cervix for a specific patient is a result of the in-homogeneities with the ROI. In future studies of human pregnant patients, we will divide the cervix into small ROIs that can be assumed homogeneous and obtain an attenuation map of the entire cervix. The variance in the estimates is expected to be high due to small ROIs, however the mean value of the estimates should approach the true value of the attenuation coefficient.

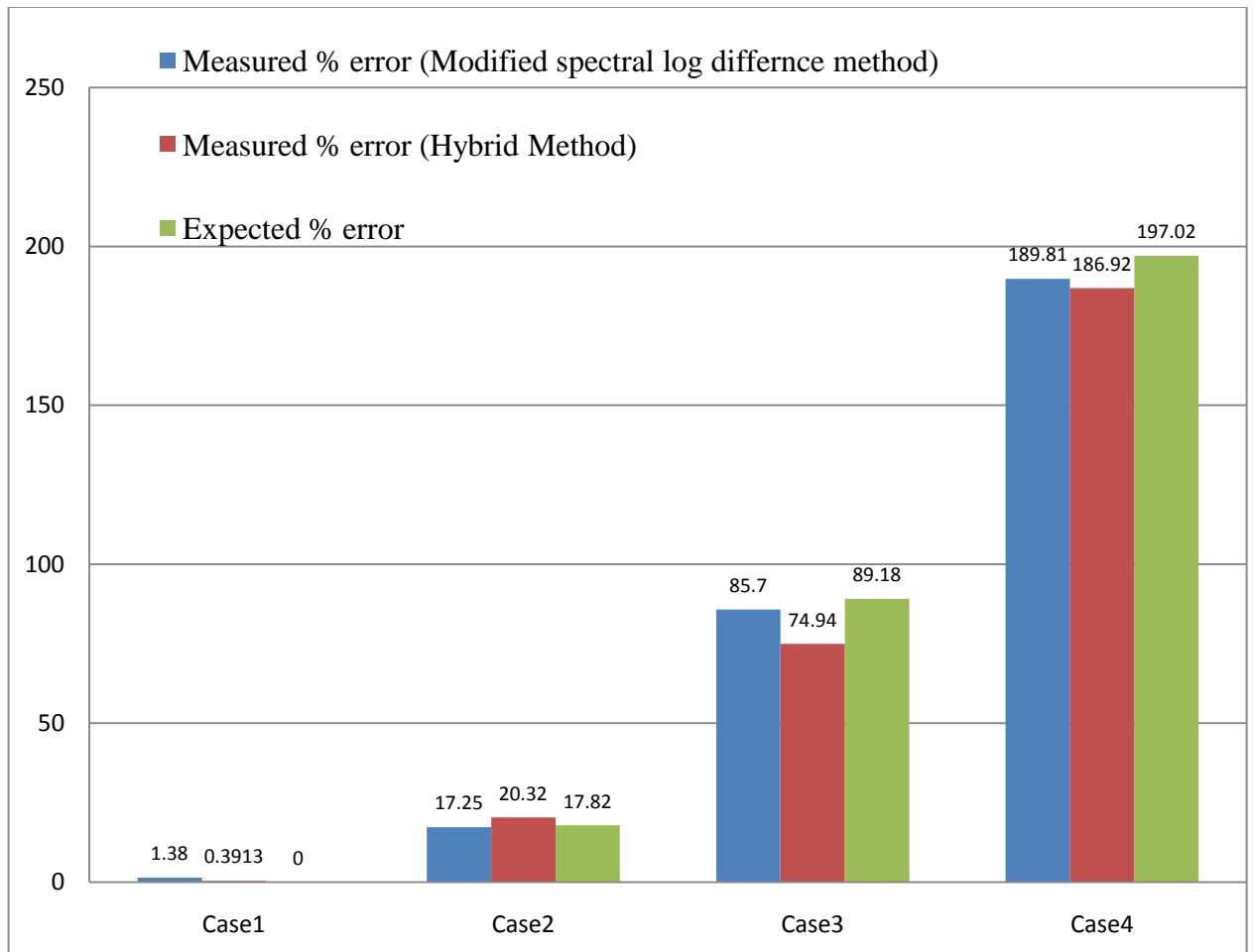


Figure 28 The expected percent error and the measured percent error in the attenuation coefficient slope of the sample using the hybrid method and the modified spectral log difference method for the four simulated cases.

4 DERIVATION AND VALIDATION OF THE TWO PROPOSED ALGORITHMS FOR TOTAL ATTENUATION ESTIMATION

4.1 Introduction

Knowing the total ultrasonic attenuation along the propagation path from the transducer surface to the ROI in the sample is essential in many medical ultrasound applications. In the area of ultrasonic tissue characterization, accurate estimates of the scatterer size and the backscatter coefficient can only be obtained if the total attenuation is known [1-3]. In ultrasound therapy applications, the total attenuation is used to calculate the intensity of ultrasound that reaches the region of interest (ROI) and hence quantify the amount of heating that is produced [51, 52]. In ultrasonic imaging, time gain compensation can be done more accurately if the total attenuation is known, and therefore eliminating shadowing and enhancement regions in the image [48]. In acoustic radiation force imaging, the total attenuation is used to quantify the amount of radiation force applied to the ROI [53, 54]. Therefore many areas of clinical medical ultrasound would benefit from an accurate estimate of the total attenuation along the propagation path.

Traditionally, the total attenuation was estimated by measuring changes in the backscatter intensity with depth [55, 56]. However, this method is inaccurate because the attenuation, the backscatter, and the diffraction effects modify the power spectrum of the backscattered RF signals. Some investigators estimated the local attenuation and thickness of the overlying tissues along the propagation path and then performed a weighted sum of these estimates to calculate the total attenuation [4, 57]. These methods, however, are prone to

error accumulation with propagation depth. Furthermore, they require the identification of the different overlying tissues, a process that may require manual intervention.

Recently, two methods for estimating the total attenuation estimation have been developed by Bigelow [28, 58]. Both methods use a planar reflector to compensate for the effects of diffraction, the transducer transfer function, and the transmit pulse transfer function. The first approach, named the spectral fit algorithm, assumed a Gaussian Form Factor and estimated the total attenuation and the scatterer size simultaneously [28]. The second approach, named the multiple filter algorithm, has a smaller dependence on the Form Factor and estimates the total attenuation by processing the spectra that result from multiplying the backscatter power spectrum by Gaussian filters [58].

In this study, the two algorithms that were used by Bigelow for total attenuation estimation [28, 29, 58] were modified by employing a tissue mimicking reference phantom (TMP) instead of a planar reflector to compensate for the transfer function of the transducer and the diffraction effects that result from focusing. The TMP has a known attenuation coefficient and a propagation sound speed that closely matches the sound speed in soft tissue. The method of using a reference phantom to compensate for the electromechanical properties of the transducer and the diffraction effects has been demonstrated before, and was used in measuring the backscatter coefficient and the local ultrasonic attenuation within a ROI in soft tissue using clinical array sources [22, 59]. Using a tissue mimicking reference phantom makes the two algorithm practical for use in clinical settings where beam formed echoes are obtained from array sources.

4.2 Derivation of the proposed algorithms

4.2.1 Derivation of the modified spectral fit algorithm

In order to estimate the total ultrasonic attenuation from the surface of the transducer to an ROI in a sample, the same transducer and power settings are used to obtain backscattered signals from the sample, and from a tissue mimicking reference phantom. The TMP has a known attenuation coefficient and a propagation sound speed that closely matches the sound speed in soft tissue. Each RF echo line is windowed at the ROI to form multiple adjacent time gated windows. The Fourier Transform is applied to every window, and the power spectra of the windows are averaged. The same procedure is performed on the region of the reference phantom that has the same compared depth as the ROI of the sample. In standard pulse echo imaging, the measured power spectrum of a windowed region in a statistically homogeneous tissue is given by:

$$S_s(f, d) \propto A_s(f) \times D_s(d, f) \times F_s(f) \times H(f) \times F_{att}(d, f, \alpha_1, \alpha_2, \dots, \alpha_N) \quad (4.1)$$

This equation assumes that the windows that are used to gate the echoes are small compared to the depth of focus of the transducer so that the variations of the field within each gated region could be ignored [40]. The subscript s denotes the sample. d is the distance from the surface of the transducer to depth that corresponds to the center of the time gated window. $A_s(f)$ is the power spectrum of the transmitted pulse. $D_s(d, f)$ is a diffraction term that results from focusing. $F_s(f)$ is a frequency dependent term that results from the scattering properties of the ROI. $H(f)$ is the transfer function of the ultrasound source. Lastly, F_{att} is the total frequency-dependent attenuation along the path and can be written as:

$$F_{att}(d, f, \alpha_1, \alpha_2, \dots, \alpha_i, \dots, \alpha_N) = \exp(-4\alpha_1 d_1 f^{n_1}) \times \exp[-4\alpha_2 (d_2 - d_1) f^{n_2}] \times \dots \\ \times \exp[-4\alpha_i (d_i - d_{i-1}) f^{n_i}] \times \dots \times \exp[-4\alpha_{N-1} (d_N - d_{N-1}) f^{n_{N-1}}] \quad (4.2)$$

where d_i is the distance from the surface of the transducer to the end of the i^{th} intervening tissue layer and $(\alpha_1, \alpha_2, \dots, \alpha_N)$ are the attenuation coefficient slopes of the intervening tissues each having a frequency dependence of n_i . The total frequency dependent attenuation along the propagation path can be assumed linearly dependent on frequency. This is a reasonable assumption over the frequency range of most transducers [60]. Hence, the attenuation coefficient can be written as:

$$\alpha = \alpha_s f \quad (4.3)$$

Where α_s is the total attenuation coefficient slope. The total frequency-dependent attenuation along the path can be written as:

$$F_{att}(d, f, \alpha_1, \alpha_2, \dots, \alpha_i, \dots, \alpha_N) \simeq \exp(-4\alpha_s df) \quad (4.4)$$

Similarly, the power spectrum of the backscattered signal from the reference phantom is:

$$S_r(f, d) \propto A_r(f) \times D(d, f) \times F_r(f) \times H(f) \times \exp(-4\alpha_r df) \quad (4.5)$$

The subscript r denotes the reference phantom. The transfer function of the transmitted pulse in the sample is equal to the transfer function of the transmitted pulse in the reference phantom if the transmission coefficient of the front surface of the sample is the same as the transmission coefficient of the front surface of the phantom. However, if the transmission coefficients are different, we have:

$$A_s(f) = cA_r(f) \quad (4.6)$$

where c is constant. The Diffraction terms $D_s(d, f)$ and $D_r(d, f)$ in equations (4.1) and (4.5) are equal if we assume that the sound speed is the same in the sample and the reference. Dividing the power spectrum of the sample by the power spectrum of the reference phantom yields:

$$S(f) = \frac{S_s(f)}{S_r(f)} \propto \frac{F_s(f)}{F_r(f)} \times \exp(-4df \Delta\alpha) \quad (4.7)$$

where
$$\Delta\alpha = (\alpha_s - \alpha_r). \quad (4.8)$$

Insana [50, 61] showed that the scattering terms can be written as:

$$F_s(f) \propto f^4 \times F_{\gamma_s}(f, a_{\text{eff}_s}) \quad (4.9)$$

$$F_r(f) \propto f^4 \times F_{\gamma_r}(f, a_{\text{eff}_r}). \quad (4.10)$$

$F_{\gamma_s}(f, a_{\text{eff}_s})$ and $F_{\gamma_r}(f, a_{\text{eff}_r})$ are the form factors of the sample and the reference, respectively. a_{eff_s} and a_{eff_r} are the effective scatterer sizes of the sample and the reference, respectively. If the form factors of both the sample and the reference are approximated by a Gaussian Form Factor, we have:

$$\begin{aligned} F_s(f, a_{\text{eff}_s}) &\propto \exp(-B_s f^2) \\ F_r(f, a_{\text{eff}_r}) &\propto \exp(-B_r f^2) \end{aligned} \quad (4.11)$$

where B is proportional to the correlation length. Equation (4.7) becomes:

$$\begin{aligned} S(f) &= \frac{S_s}{S_r} \propto \frac{\exp(-B_s f^2)}{\exp(-B_r f^2)} \exp(-4df \Delta\alpha) \\ S(f) &\propto \exp(-\Delta B f^2) \exp(-4df \Delta\alpha) \end{aligned} \quad (4.12)$$

where $\Delta B = B_s - B_r$. By taking the natural algorithm of (4.12) we get:

$$S_{\ln}(f) = \ln[S(f)] = -\Delta B f^2 - 4df \Delta \alpha + c \quad (4.13)$$

Equation (4.13) is linear in the unknowns $\Delta \alpha$, ΔB , and c , so least linear squares can be used

to estimate the unknown $\Delta \alpha$ [62]:

$$\begin{aligned} \Delta \alpha &= \frac{1}{\Delta} \begin{vmatrix} L & \sum_{i=1}^L S_{\ln}(f_i) & \sum_{i=1}^L f_i^2 \\ \sum_{i=1}^L f_i & \sum_{i=1}^L f_i S_{\ln}(f_i) & \sum_{i=1}^L f_i^3 \\ \sum_{i=1}^L f_i^2 & \sum_{i=1}^L f_i^2 S_{\ln}(f_i) & \sum_{i=1}^L f_i^4 \end{vmatrix} = \frac{1}{\Delta} \left[L \begin{vmatrix} \sum_{i=1}^L f_i S_{\ln}(f_i) & \sum_{i=1}^L f_i^3 \\ \sum_{i=1}^L f_i^2 S_{\ln}(f_i) & \sum_{i=1}^L f_i^4 \end{vmatrix} - \sum_{i=1}^L S_{\ln}(f_i) \begin{vmatrix} \sum_{i=1}^L f_i & \sum_{i=1}^L f_i^3 \\ \sum_{i=1}^L f_i^2 & \sum_{i=1}^L f_i^4 \end{vmatrix} + \sum_{i=1}^L f_i^2 \begin{vmatrix} \sum_{i=1}^L f_i & \sum_{i=1}^L f_i S_{\ln}(f_i) \\ \sum_{i=1}^L f_i^2 & \sum_{i=1}^L f_i^2 S_{\ln}(f_i) \end{vmatrix} \right] \\ \Delta &= \begin{vmatrix} L & \sum_{i=1}^L f_i & \sum_{i=1}^L f_i^2 \\ \sum_{i=1}^L f_i & \sum_{i=1}^L f_i^2 & \sum_{i=1}^L f_i^3 \\ \sum_{i=1}^L f_i^2 & \sum_{i=1}^L f_i^3 & \sum_{i=1}^L f_i^4 \end{vmatrix} = L \begin{vmatrix} \sum_{i=1}^L f_i^2 & \sum_{i=1}^L f_i^3 \\ \sum_{i=1}^L f_i^3 & \sum_{i=1}^L f_i^4 \end{vmatrix} - \sum_{i=1}^L f_i \begin{vmatrix} \sum_{i=1}^L f_i & \sum_{i=1}^L f_i^3 \\ \sum_{i=1}^L f_i^2 & \sum_{i=1}^L f_i^4 \end{vmatrix} + \sum_{i=1}^L f_i^2 \begin{vmatrix} \sum_{i=1}^L f_i & \sum_{i=1}^L f_i^2 \\ \sum_{i=1}^L f_i^2 & \sum_{i=1}^L f_i^3 \end{vmatrix} \end{aligned} \quad (4.14)$$

where f_i are the discrete frequencies of the power spectrum and L is the total number of frequencies in the usable frequency range. L depends on the size of the time gated window and the usable frequency range. Equation (4.14) can be simplified as:

$$\begin{aligned} \Delta \alpha &= \frac{L}{\Delta} \left[\left(\sum_{i=1}^L f_i S_{\ln}(f_i) \right) \left(\sum_{i=1}^L f_i^4 \right) - \left(\sum_{i=1}^L f_i^3 \right) \left(\sum_{i=1}^L f_i^2 S_{\ln}(f_i) \right) \right] - \\ &\frac{\sum_{i=1}^L S_{\ln}(f_i)}{\Delta} \left[\left(\sum_{i=1}^L f_i \right) \left(\sum_{i=1}^L f_i^4 \right) - \left(\sum_{i=1}^L f_i^3 \right) \left(\sum_{i=1}^L f_i^2 \right) \right] + \\ &\frac{\sum_{i=1}^L f_i^2}{\Delta} \left[\left(\sum_{i=1}^L f_i \right) \left(\sum_{i=1}^L f_i^2 S_{\ln}(f_i) \right) - \left(\sum_{i=1}^L f_i S_{\ln}(f_i) \right) \left(\sum_{i=1}^L f_i^2 \right) \right] \end{aligned} \quad (4.15)$$

Once $\Delta\alpha$ is known, the slope of the total attenuation coefficient in the unknown sample can be determined using equation (4.8).

4.2.2 Derivation of the modified multiple filter algorithm

The multiple filter algorithm also assumes a Gaussian Form Factor as given by equation (4.11). If we multiply (4.12) by a Gaussian Filter with a center frequency f_c and a variance σ_c^2 , we obtain:

$$\begin{aligned}
 S_{Gauss}(f) &\propto \exp(-\Delta B f^2) \exp(-4df \Delta\alpha) \exp\left[\frac{(f - f_c)^2}{2\sigma_c^2}\right] \\
 S_{Gauss}(f) &\propto \exp\left[f^2\left(\frac{1-2\Delta B\sigma_c^2}{2\sigma_c^2}\right) - 2f\left(2d\Delta\alpha + \frac{f_c}{2\sigma_c^2}\right) + \left(\frac{f_c^2}{2\sigma_c^2}\right)\right] \\
 S_{Gauss}(f) &\propto \exp\left[f^2\left(\frac{1-2\Delta B\sigma_c^2}{2\sigma_c^2}\right) - 2f\left(2d\Delta\alpha + \frac{f_c}{2\sigma_c^2}\right)\right] \\
 S_{Gauss}(f) &\propto \exp\left[\frac{f^2 - 2f\left(\frac{2\sigma_c^2}{1-2\Delta B\sigma_c^2}\right)\left(2d\Delta\alpha + \frac{f_c}{2\sigma_c^2}\right)}{\left(\frac{2\sigma_c^2}{1-2\Delta B\sigma_c^2}\right)}\right] \\
 S_{Gauss}(f) &\propto \exp\left[\frac{(f - \tilde{f}_c)^2}{2\tilde{\sigma}_c^2}\right]
 \end{aligned}$$

(4.16)

where

$$\begin{aligned}\tilde{\sigma}_c^2 &= \frac{\sigma_c^2}{1-2\Delta B\sigma_c^2} \\ \tilde{f}_c &= \left(\frac{2\sigma_c^2}{1-2\Delta B\sigma_c^2} \right) \left(2d\Delta\alpha + \frac{f_c}{2\sigma_c^2} \right) = \left(\frac{1}{1-2\Delta B\sigma_c^2} \right) f_c + 4\tilde{\sigma}_c^2 d\Delta\alpha\end{aligned}\quad (4.17)$$

Equation (4.17) shows that the resulting spectrum is also Gaussian with a new center frequency \tilde{f}_c which is a function of the scattering properties, attenuation, and the center frequency of the Gaussian filter. By using multiple Gaussian filters with different center frequencies f_c , $\Delta\alpha$ can be estimated by finding the intercept of the line that fits the new center frequencies \tilde{f}_c with respect to the center frequencies of the Gaussian filters. Once $\Delta\alpha$ is known, the slope of the total attenuation coefficient in the unknown sample can be determined using equation (4.8).

4.3 Statistical analysis of the total attenuation estimation algorithms

In the derivation of the spectral fit and the multiple filter algorithms, it was assumed that the power spectra $S(f)$ are the expected power spectra of the time gated regions. However, because of the random nature of the backscattered signals, the magnitude squared of the Fourier Transform of the time gated window (periodogram) is a random process. Therefore, the estimate of the total attenuation coefficient is a random variable. Statistical analysis on each algorithm will quantify the variance in the total attenuation estimate and reveal its dependence on the bandwidth, and the size of ROI. By comparing the variance in the total attenuation estimates from each algorithm, one can infer which algorithm is superior to the other.

4.3.1 Statistical analysis of the power spectrum

Neglecting windowing effects, variances in the power spectra are given by [63]:

$$\text{var}[S(f)] \approx S(f)^2 \quad (4.18)$$

where $S(f)$ is the measured power spectrum and $S(f)$ is the expected value of the power spectrum. In addition, the selection of harmonic frequencies (frequencies which are multiple frequencies of $1/NT$) $f_1 = m/NT$ and $f_2 = n/NT$, such that $m \neq n$, results in zero covariance [64].

$$\text{cov}[S(f_1), S(f_2)] = 0 \quad (4.19)$$

That is the values of the power spectrum separated by $1/NT$ Hz are uncorrelated. Here N is the number of time samples in the gated window and T is the time interval between two adjacent time samples. Applying the above results to the power spectra obtained from the gated region of the sample and the gated region of the reference phantom, we have:

$$\begin{aligned} \text{var}[S_s(f)] &\approx S_s(f)^2 \\ \text{var}[S_r(f)] &\approx S_r(f)^2 \end{aligned} \quad (4.20)$$

If N_s independent spectra are averaged to obtain an estimate of the power spectrum of the sample $S_s(f)$ and N_r independent spectra are averaged to obtain an estimate of the power spectrum of the reference $S_r(f)$, equation (4.20) becomes [22]:

$$\begin{aligned}\text{var}\left[S_s(f)\right] &\approx \frac{S_s(f)^2}{N_s} \\ \text{var}\left[S_r(f)\right] &\approx \frac{S_r(f)^2}{N_r}\end{aligned}\tag{4.21}$$

In both the spectral fit algorithm and the multiple filter algorithm, we divide the estimated power spectrum of the sample by the estimated power spectrum of the reference in order to eliminate the characteristics of the transducer and the transmit pulse. However, because this operation involves the ratio of two random variables, it is necessary to quantify the variance of this ratio. It can be shown that if we have a functional dependence such that $x = f(u, v, \dots)$, we have [62]:

$$\sigma_x^2 \approx \sigma_u^2 \left(\frac{\partial x}{\partial u} \bigg|_{\bar{u}} \right)^2 + \sigma_v^2 \left(\frac{\partial x}{\partial v} \bigg|_{\bar{v}} \right)^2 \tag{4.22}$$

where u and v are uncorrelated random variables with mean \bar{u} and \bar{v} , respectively and variances σ_u^2 and σ_v^2 , respectively. Given equation (4.7) and the results of equations (4.21) and (4.22) we have:

$$\begin{aligned}
S(f) &= \frac{S_s(f)}{S_r(f)} \\
\text{var}[S(f)] &\approx \text{var}[S_s(f)] \left(\left. \frac{\partial S(f)}{\partial S_s(f)} \right|_{(S_s(f), S_r(f))} \right)^2 + \text{var}[S_r(f)] \left(\left. \frac{\partial S(f)}{\partial S_r(f)} \right|_{(S_s(f), S_r(f))} \right)^2 \\
\text{var}[S(f)] &\approx \frac{S_s(f)^2}{N_s} \left(\frac{1}{S_r(f)} \right)^2 + \frac{S_r(f)^2}{N_r} \left[-\frac{S_s(f)}{S_r(f)^2} \right]^2 \\
\text{var}[S(f)] &\approx \frac{S_s(f)^2}{N_s S_r(f)^2} + \frac{S_s(f)^2}{N_r S_r(f)^2} \\
\text{var}[S(f)] &\approx \frac{(N_s + N_r)}{N_s N_r} \frac{S_s(f)^2}{S_r(f)^2} \\
\text{var}[\widehat{S(f)}] &\approx \frac{(N_s + N_r)}{N_s N_r} S(f)^2
\end{aligned} \tag{4.23}$$

The result of equation (4.23) is essential to calculating the variance in the total attenuation coefficient slope estimate that is obtained by both the spectral fit method and the multiple filter method. This equation will also allow us to quantify the dependence of the variance on the number of averaged independent power spectra (lateral resolution), the size of the gated window (axial resolution), and the bandwidth of the transducer (usable frequency range).

4.3.2 Statistical analysis of the modified spectral fit method

In order to obtain an expression for the variance in the total attenuation coefficient estimate that is obtained using the spectral fit method, we start with equation (4.13) and rewrite it as:

$$S_{\ln}(f_i) = \ln \left[\frac{S_s(f_i)}{S_r(f_i)} \right] = \ln[S(f_i)] = af_i^2 + bf_i + c_i \tag{4.24}$$

where $a = -\Delta B$ and $b = -4d\Delta\alpha$, and f_i are the individual frequency components of the spectrum. We apply the result of equation (4.22) to obtain the variance in $S_{\ln}(f)$:

$$\begin{aligned} \text{var}\left[S_{\ln}(f_i)\right] &\approx \text{var}\left[S(f_i)\right] \left(\left. \frac{\partial S_{\ln}(f_i)}{\partial S(f_i)} \right|_{S(f_i)} \right)^2 \\ \text{var}\left[S_{\ln}(f_i)\right] &\approx \text{var}\left[S(f_i)\right] \left(\frac{1}{S(f_i)} \right)^2 = \frac{(N_s + N_r)}{N_s N_r} S(f_i)^2 \left(\frac{1}{S(f_i)} \right)^2 \\ \text{var}\left[S_{\ln}(f_i)\right] &\approx \frac{(N_s + N_r)}{N_s N_r} \end{aligned} \quad (4.25)$$

Equation (4.25) shows that the variance in $S_{\ln}(f_i)$ depends only on the number of averaged independent power spectra of the sample and the reference. This result is important because the variance in $S_{\ln}(f_i)$ is independent of the expected power spectra of the sample and reference. Equation (4.24) is linear in the coefficients a , b , and c . Therefore, we can use least linear squares to calculate \hat{b} , the estimated value of the coefficient b . According to Bevington, \hat{b} can be written as [62]:

$$\begin{aligned}
\hat{b} &= \frac{\begin{vmatrix} L & \sum_{i=1}^L S_{\ln}(f_i) & \sum_{i=1}^L f_i^2 \\ \sum_{i=1}^L f_i & \sum_{i=1}^L f_i S_{\ln}(f_i) & \sum_{i=1}^L f_i^3 \\ \sum_{i=1}^L f_i^2 & \sum_{i=1}^L f_i^2 S_{\ln}(f_i) & \sum_{i=1}^L f_i^4 \end{vmatrix}}{\begin{vmatrix} L & \sum_{i=1}^L f_i & \sum_{i=1}^L f_i^2 \\ \sum_{i=1}^L f_i & \sum_{i=1}^L f_i^2 & \sum_{i=1}^L f_i^3 \\ \sum_{i=1}^L f_i^2 & \sum_{i=1}^L f_i^3 & \sum_{i=1}^L f_i^4 \end{vmatrix}} = \frac{1}{\Delta} \begin{vmatrix} L & \sum_{i=1}^L S_{\ln}(f_i) & \sum_{i=1}^L f_i^2 \\ \sum_{i=1}^L f_i & \sum_{i=1}^L f_i S_{\ln}(f_i) & \sum_{i=1}^L f_i^3 \\ \sum_{i=1}^L f_i^2 & \sum_{i=1}^L f_i^2 S_{\ln}(f_i) & \sum_{i=1}^L f_i^4 \end{vmatrix} \\
\hat{b} &= \frac{L}{\Delta} \left[\left(\sum_{i=1}^L f_i S_{\ln}(f_i) \right) \left(\sum_{i=1}^L f_i^4 \right) - \left(\sum_{i=1}^L f_i^3 \right) \left(\sum_{i=1}^L f_i^2 S_{\ln}(f_i) \right) \right] \\
&\quad - \frac{\sum_{i=1}^L S_{\ln}(f_i)}{\Delta} \left[\left(\sum_{i=1}^L f_i \right) \left(\sum_{i=1}^L f_i^4 \right) - \left(\sum_{i=1}^L f_i^3 \right) \left(\sum_{i=1}^L f_i^2 \right) \right] \\
&\quad + \frac{\sum_{i=1}^L f_i^2}{\Delta} \left[\left(\sum_{i=1}^L f_i \right) \left(\sum_{i=1}^L f_i^2 S_{\ln}(f_i) \right) - \left(\sum_{i=1}^L f_i S_{\ln}(f_i) \right) \left(\sum_{i=1}^L f_i^2 \right) \right]
\end{aligned} \tag{4.26}$$

where L is the number of frequency components of the usable frequency range. The variance

in \hat{b} was also given by Bevington, and can be expressed as [62]:

$$\begin{aligned}
\text{var}(\hat{b}) &\approx \sum_{i=1}^L \text{var} S_{\ln}(f_i) \left(\frac{\partial \hat{b}}{\partial S_{\ln}(f_i)} \right)^2 \\
\text{var}(\hat{b}) &\approx \frac{1}{\Delta^2} \frac{(N_s + N_r)}{N_s N_r} \sum_{i=1}^L \left\{ L \left[f_i \left(\sum_{i=1}^L f_i^4 \right) - f_i^2 \left(\sum_{i=1}^L f_i^3 \right) \right] - \left[\left(\sum_{i=1}^L f_i \right) \left(\sum_{i=1}^L f_i^4 \right) - \left(\sum_{i=1}^L f_i^3 \right) \left(\sum_{i=1}^L f_i^2 \right) \right] \right. \\
&\quad \left. + \sum_{i=1}^L f_i^2 \left[f_i^2 \left(\sum_{i=1}^L f_i \right) - f_i \left(\sum_{i=1}^L f_i^2 \right) \right] \right\}^2
\end{aligned} \tag{4.27}$$

where

$$\Delta = L \left[\left(\sum_{i=1}^L f_i^2 \right) \left(\sum_{i=1}^L f_i^4 \right) - \left(\sum_{i=1}^L f_i^3 \right)^2 \right] - \sum_{i=1}^L f_i \left[\left(\sum_{i=1}^L f_i \right) \left(\sum_{i=1}^L f_i^4 \right) - \left(\sum_{i=1}^L f_i^3 \right) \left(\sum_{i=1}^L f_i^2 \right) \right] + \sum_{i=1}^L f_i^2 \left[\left(\sum_{i=1}^L f_i \right) \left(\sum_{i=1}^L f_i^3 \right) - \left(\sum_{i=1}^L f_i^2 \right)^2 \right] \quad (4.28)$$

As expected, the variance in \hat{b} and hence in $\Delta\alpha$ is a function of the number of averaged independent power spectra in the sample and the reference and the number of frequency components in the usable frequency range. The number of frequency components in the usable frequency range is a function of the transducer bandwidth, the size of the time gated window (ROI length in the axial direction), and the difference in the attenuation coefficient of the sample and the attenuation coefficient of the reference. If the attenuation coefficient of the sample is large compared to the attenuation coefficient of the reference, the spectrum of the sample will experience a larger shift towards the lower frequencies compared to the spectrum of the reference and this leads to a small usable frequency range, even if the bandwidth is large. The same effect would occur if the attenuation coefficient of the reference is large compared to the attenuation coefficient of the sample.

Given a tissue mimicking phantom with a constant attenuation coefficient and an ultrasound system with a fixed bandwidth, the only parameter that affects the variance of the estimate $d\alpha_s$ is the ROI size. The lateral dimension of the ROI depends on the number of averaged periodograms of the sample and the reference, and the axial dimension of the ROI depends on the size of the time gated window.

4.3.3 Statistical analysis of the modified multiple filter algorithm

In order to obtain an expression for the variance in the total attenuation coefficient estimate that is obtained using the multiple filter method, we start with equation (4.16) and rewrite it as:

$$S_{Gauss}(f_i) = S(f) \exp\left[\frac{(f_i - f_c)^2}{2\sigma_c^2}\right] = c \times \exp\left[-\frac{(f_i - \tilde{f}_c)^2}{2\tilde{\sigma}_c^2}\right] \quad (4.29)$$

Using equation (4.23), we can write the variance in $S_{Gauss}(f)$ as follows [65]:

$$\begin{aligned} \text{var}\left(S_{Gauss}(f_i)\right) &= \text{var}\left[S(f_i)\right] \left\{ \exp\left[\frac{(f_i - f_c)^2}{2\sigma_c^2}\right] \right\}^2 \\ \text{var}\left(S_{Gauss}(f)\right) &= \frac{(N_s + N_r)}{N_s N_r} S(f_i)^2 \exp\left[\frac{(f_i - f_c)^2}{\sigma_c^2}\right] \\ \text{var}\left(S_{Gauss}(f_i)\right) &= \frac{(N_s + N_r)}{N_s N_r} S_{Gauss}(f_i)^2 \end{aligned} \quad (4.30)$$

If we take the natural logarithm of equation (4.16), we obtain:

$$S_{Gauss-\ln}(f_i) = \ln\left(S_{Gauss}(f_i)\right) = \left[\ln(c) - \frac{\tilde{f}_c^2}{2\tilde{\sigma}_c^2} \right] - \frac{f_i^2}{2\tilde{\sigma}_c^2} + \frac{\tilde{f}_c}{\tilde{\sigma}_c^2} f_i \quad (4.31)$$

By applying equation (4.22), we obtain:

$$\begin{aligned}
\text{var}\left(S_{\text{Gauss}-\ln}(f_i)\right) &\approx \text{var}\left[S_{\text{Gauss}}(f_i)\right] \left(\left. \frac{\partial S_{\text{Gauss}-\ln}(f_i)}{\partial S_{\text{Gauss}}(f_i)} \right|_{S_{\text{Gauss}}(f)} \right)^2 \\
\text{var}\left(S_{\text{Gauss}-\ln}(f)\right) &\approx \frac{(N_s + N_r)}{N_s N_r} S_{\text{Gauss}}(f)^2 \left(\frac{1}{S_{\text{Gauss}}(f)^2} \right) \\
\text{var}\left(S_{\text{Gauss}-\ln}(f)\right) &\approx \frac{(N_s + N_r)}{N_s N_r}
\end{aligned} \tag{4.32}$$

If we add $\frac{f_i^2}{2\tilde{\sigma}_c^2}$ to $S_{\text{Gauss}-\ln}(f_i)$ in equation (4.31), we obtain:

$$\begin{aligned}
S_{\text{new}}(f_i) &= S_{\text{Gauss}-\ln}(f_i) + \frac{f_i^2}{2\tilde{\sigma}_c^2} = \frac{\tilde{f}_c}{\tilde{\sigma}_c^2} f_i + \left[\ln(c) - \frac{\tilde{f}_c^2}{2\tilde{\sigma}_c^2} \right] \\
S_{\text{new}}(f_i) &= af_i + b
\end{aligned} \tag{4.33}$$

where $a = \frac{\tilde{f}_c}{\tilde{\sigma}_c^2}$ and $b = \left[\ln(c) - \frac{\tilde{f}_c^2}{2\tilde{\sigma}_c^2} \right]$. At each frequency component, $\frac{f_i^2}{2\tilde{\sigma}_c^2}$ is a constant,

therefore the variance of $S_{\text{new}}(f_i)$ is given by:

$$\text{var}\left(S_{\text{new}}(f_i)\right) = \text{var}\left(S_{\text{Gauss}-\ln}(f)\right) \approx \frac{(N_s + N_r)}{N_s N_r} \tag{4.34}$$

We can calculate a , the estimate of the coefficient a by performing least linear squares to equation (4.33). According to Bevington [62], the variance in the estimate a is given by:

$$\begin{aligned}
\text{var}(a) &= \frac{M \text{var}\left(S_{\text{new}}(f_i)\right)}{M \sum_{i=1}^M f_i^2 - \left(\sum_{i=1}^M f_i\right)^2} = \frac{(N_s + N_r)}{N_s N_r} \frac{M}{M \sum_{i=1}^M f_i^2 - M^2 f_c^2} \\
\text{var}(a) &= \frac{(N_s + N_r)}{N_s N_r} \frac{1}{\sum_{i=1}^M (f_i - f_c)^2}
\end{aligned} \tag{4.35}$$

where M is the number of frequency components in the spectrum $S_{Gauss}(f_i)$. If L is the total number frequencies of the spectrum $S(f)$ and K is the number of non-overlapping Gaussian filters that are multiplied by the spectrum $S(f)$, we have:

$$L = KM \quad (4.36)$$

Using $a = \frac{\tilde{f}_c}{\tilde{\sigma}_c^2}$, equation (4.17) can be written as:

$$\begin{aligned} \tilde{f}_c(j) &= \left(\frac{1}{1 - 2\Delta B \sigma_c^2} \right) f_c(j) + 4\tilde{\sigma}_c^2 d\Delta\alpha \\ a(j) &= \frac{\tilde{f}_c(j)}{\tilde{\sigma}_c^2} = \left(\frac{1}{\tilde{\sigma}_c^2 (1 - 2\Delta B \sigma_c^2)} \right) f_c(j) + 4d\Delta\alpha \\ a(j) &= \chi f_c(j) + \gamma \end{aligned} \quad (4.37)$$

where j is the index of the Gaussian filter. i.e. j varies from 1 to K Gaussian filters.

Therefore, we can find and estimate for $\gamma = 4d\Delta\alpha$ by performing least linear squares to equation (4.37). The variance in the estimate γ is given by [62]:

$$\begin{aligned} \text{var}(\gamma) &= \frac{1}{\Delta} \sum_{j=1}^K \frac{f_c(j)^2}{\text{var}(a(j))} \\ \Delta &= \sum_{j=1}^K \frac{1}{\text{var}(a(j))} \sum_{j=1}^K \frac{f_c(j)^2}{\text{var}(a(j))} - \left(\sum_{j=1}^K \frac{f_c(j)}{\text{var}(a(j))} \right)^2 \end{aligned} \quad (4.38)$$

Using equation (4.35), we can write $\text{var}(\gamma)$ as:

$$\begin{aligned}
\text{var}(\gamma) &= \frac{\sum_{j=1}^K \frac{f_c(j)^2}{(N_s + N_r)} \frac{1}{N_s N_r \sum_{i=1}^M (f_i - f_c(j))^2}}{\left(\sum_{j=1}^K \frac{1}{(N_s + N_r)} \frac{1}{N_s N_r \sum_{i=1}^M (f_i - f_c(j))^2} \sum_{j=1}^K \frac{f_c(j)^2}{(N_s + N_r)} \frac{1}{N_s N_r \sum_{i=1}^M (f_i - f_c(j))^2} - \left(\sum_{j=1}^K \frac{f_c(j)}{(N_s + N_r)} \frac{1}{N_s N_r \sum_{i=1}^M (f_i - f_c(j))^2} \right)^2 \right)} \\
\text{var}(\gamma) &= \frac{(N_s + N_r)}{N_s N_r} \frac{\sum_{j=1}^K \left\{ \left[\sum_{i=1}^M (f_i - f_c(j))^2 \right] f_c(j)^2 \right\}}{\left\{ \sum_{j=1}^K \left[\sum_{i=1}^M (f_i - f_c(j))^2 \right] \right\} \left\{ \sum_{j=1}^K f_c(j)^2 \left[\sum_{i=1}^M (f_i - f_c(j))^2 \right] \right\} - \left\{ \sum_{j=1}^K \left[\sum_{i=1}^M (f_i - f_c(j))^2 \right] f_c(j) \right\}^2} \\
\widehat{\text{var}(\gamma)} &= \frac{(N_s + N_r)}{N_s N_r} \frac{1}{\left\{ \sum_{j=1}^K \left[\sum_{i=1}^M (f_i - f_c(j))^2 \right] \right\} - \frac{\left\{ \sum_{j=1}^K \left[\sum_{i=1}^M (f_i - f_c(j))^2 \right] f_c(j) \right\}^2}{\sum_{j=1}^K \left\{ \left[\sum_{i=1}^M (f_i - f_c(j))^2 \right] f_c(j)^2 \right\}}} \\
&\quad (4.39)
\end{aligned}$$

The variance in γ and hence in $\Delta\alpha$ is a function of the number of averaged power spectra in the sample and the reference, the size of the time gated window, the number of frequency components in the usable frequency range and the number of Gaussian filters.

4.4 Validation of statistical analysis results using computer simulations

4.4.1 Simulation Procedure

Computer simulations with a sampling frequency of 100 MHz were used to obtain two different data sets of RF backscattered signals using a Gaussian focused beam (5 cm focal

length, 0.62 mm beam width, 7.5 MHz center frequency, and 50% -3dB bandwidth on transmit). One data set was used as a sample while the other was used as reference. The sample and reference had attenuation coefficients of 0.7 dB/cm-MHz and 0.5 dB-cm-MHz, respectively. The sample scatterers had a Gaussian Form Factor with a 20 μm effective radius. The reference had spherical shell scatterers with 10 μm radii. The spatial pulse length is 0.2 mm (0.25 μs , 1λ). Both the sample and the reference had a scattering density of 100 mm^{-3} , corresponding to approximately 10 scatterers per resolution cell, which is adequate for fully developed speckle [27].

In the simulations, 3000 independent echo lines were generated for the sample and the reference. Each RF echo line was gated with a rectangular window centered at the focus. The power spectrum of each time gated window is approximated by taking the Fourier Transform of the RF data and squaring the magnitude of the result. In order to operate above the noise floor, the usable frequency range was selected to be the frequencies common to the -20 dB bandwidths of the sample and reference spectrum as is illustrated Figure 29.

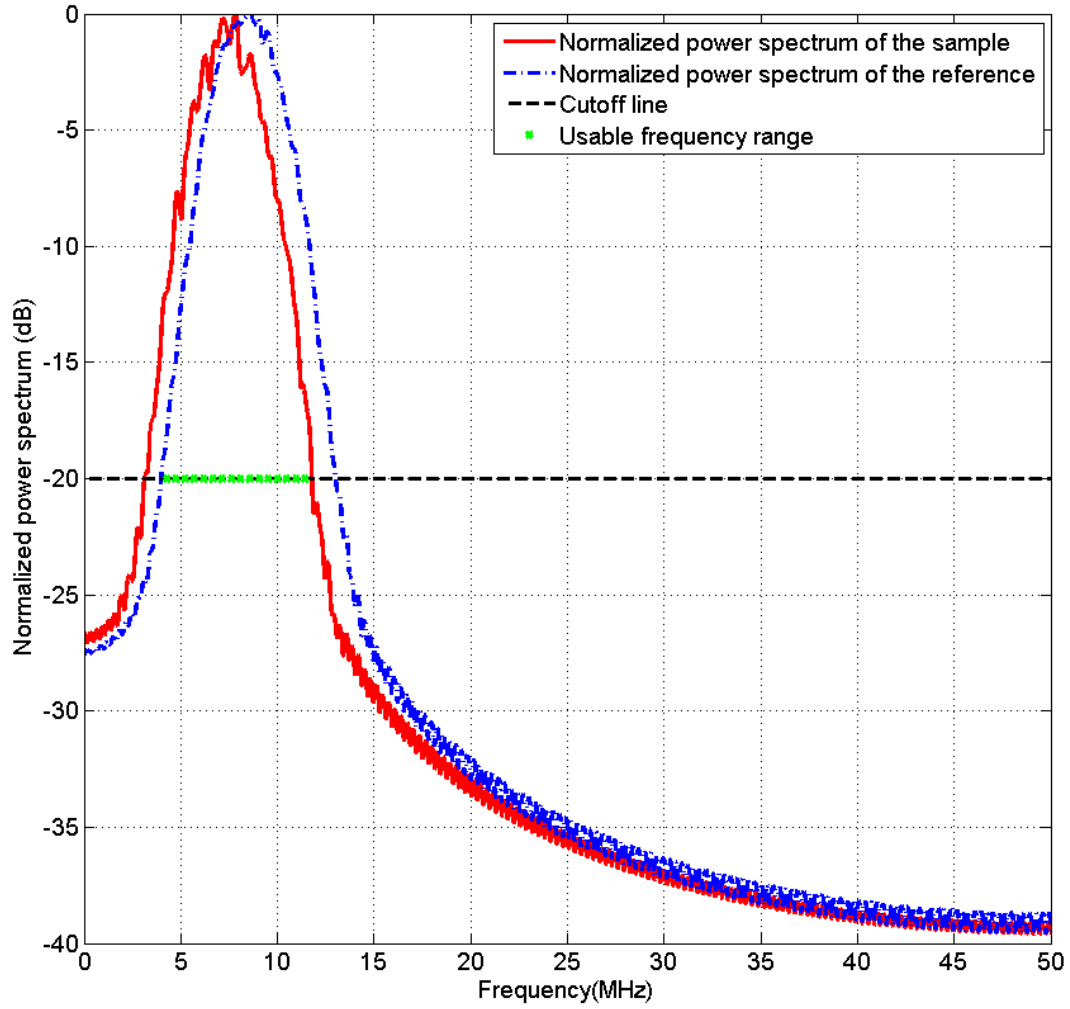


Figure 29 A plot of the normalized power spectrum obtained from averaging 50 power spectra from the sample and the reference in the simulations

4.4.2 Validation of the power spectrum statistical analysis

In this section, each time gated window contains 15 pulse lengths. In order to determine the validity of equation (4.18) i.e. $\text{var}[S(f)] \approx S(f)^2$ which states that the variance of the periodogram (magnitude square of the Fourier Transform of the time gate window) is equal

to the expected power spectrum, we calculated the square of the mean of 100 periodograms at each frequency component to estimate $S(f)^2$, and we calculated the variance in the 100 periodograms to estimate $\text{var}[S(f)]$. As shown in Figure 30, the variance in the power spectrum is closely approximated by the square of the expected power spectrum. This confirms equation (4.18).

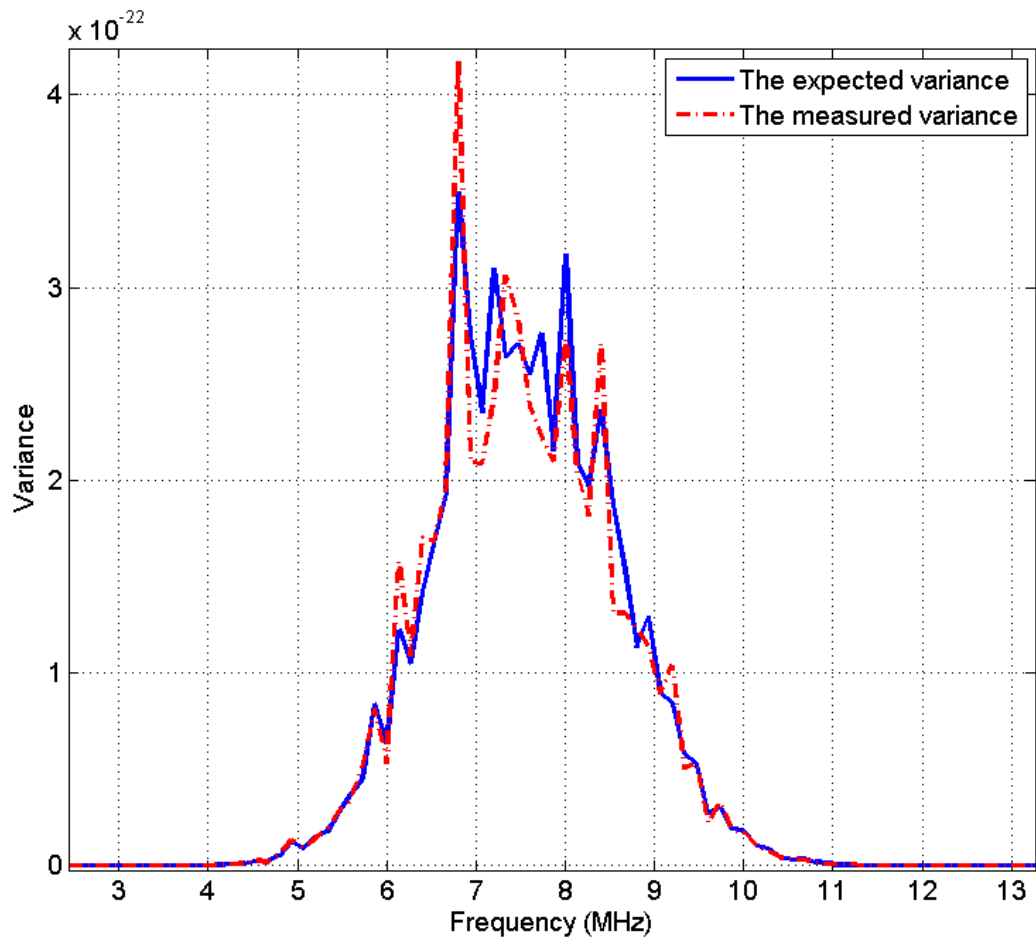


Figure 30 Plot of the square of the mean and the variance of 100 power spectra obtained from the sample

To show the validity of equation (4.19) i.e. $\text{cov}[S(f_1), S(f_2)] = 0$, we calculated the correlation coefficient, $\rho(m, n)$, between the value of the power spectrum at frequencies m and n of the usable frequency range according to the following equation:

$$\rho(m, n) = \frac{\sum_{i=1}^{100} \{ [S_i(f_m) - S(f_m)] [S_i(f_n) - S(f_n)] \}}{\sqrt{\sum_{i=1}^{100} \{ [S_i(f_m) - S(f_m)]^2 [S_i(f_n) - S(f_n)]^2 \}}} \quad (4.40)$$

where $S_i(f_m)$ is the measured value of the i^{th} power spectrum at frequency m , and $S_i(f_m)$ is the mean of the values of the 100 power spectra at frequency m . Figure 31 shows a plot of the correlation coefficient of the power spectrum at frequency 7.5 MHz with the rest of the frequency components in the usable frequency range. We observe that there is no correlation between the values of the power spectrum at frequencies m and n such that $m \neq n$. These results confirm equation (4.19).

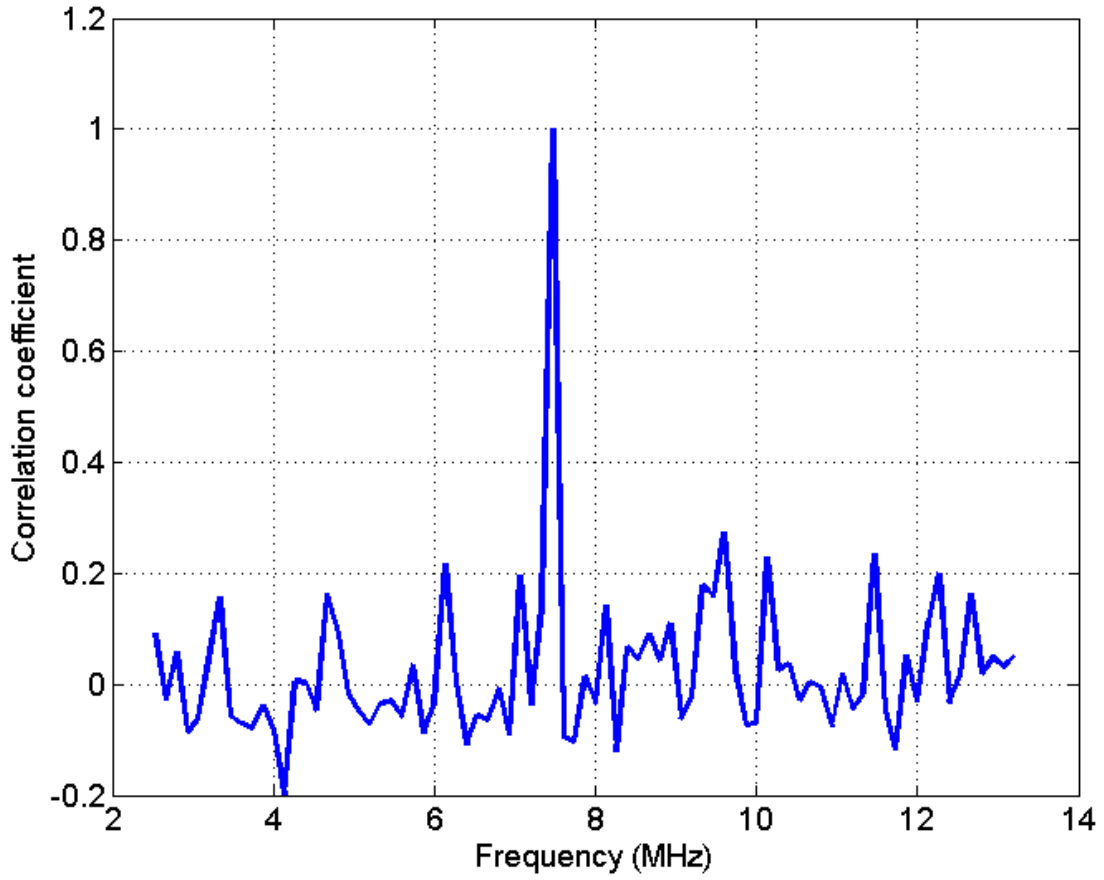


Figure 31 plot of the correlation coefficient of the power spectrum at frequency 7.5 MHz with the rest of the frequency components in the usable frequency range.

Equation (4.21), i.e. $\text{var}[S_s(f)] \approx \frac{S_s(f)^2}{N_s}$ states that at each frequency component, the

variance of the values of the power spectrum that is obtained by averaging N_s periodograms (magnitude square of the Fourier Transform of the gated window) is given by the square of the expected value of the power spectrum divided by N_s . To show the validity of this equation, we calculated the variance of 30 spectra, each of which was obtained by averaging

N_s periodograms. We also estimated $\frac{S_s(f)^2}{N_s}$ by averaging 100 periodograms and dividing the result by N_s . Figure 32 (a) and (b) show the results obtained when $N_s = 10$ and $N_s = 25$, respectively. Based on this figure, the expected variance $\frac{S_s(f)^2}{N_s}$ closely approximates the measured variance. It is also apparent the variance is smaller in the case where $N_s = 25$ compared the case where $N_s = 10$.

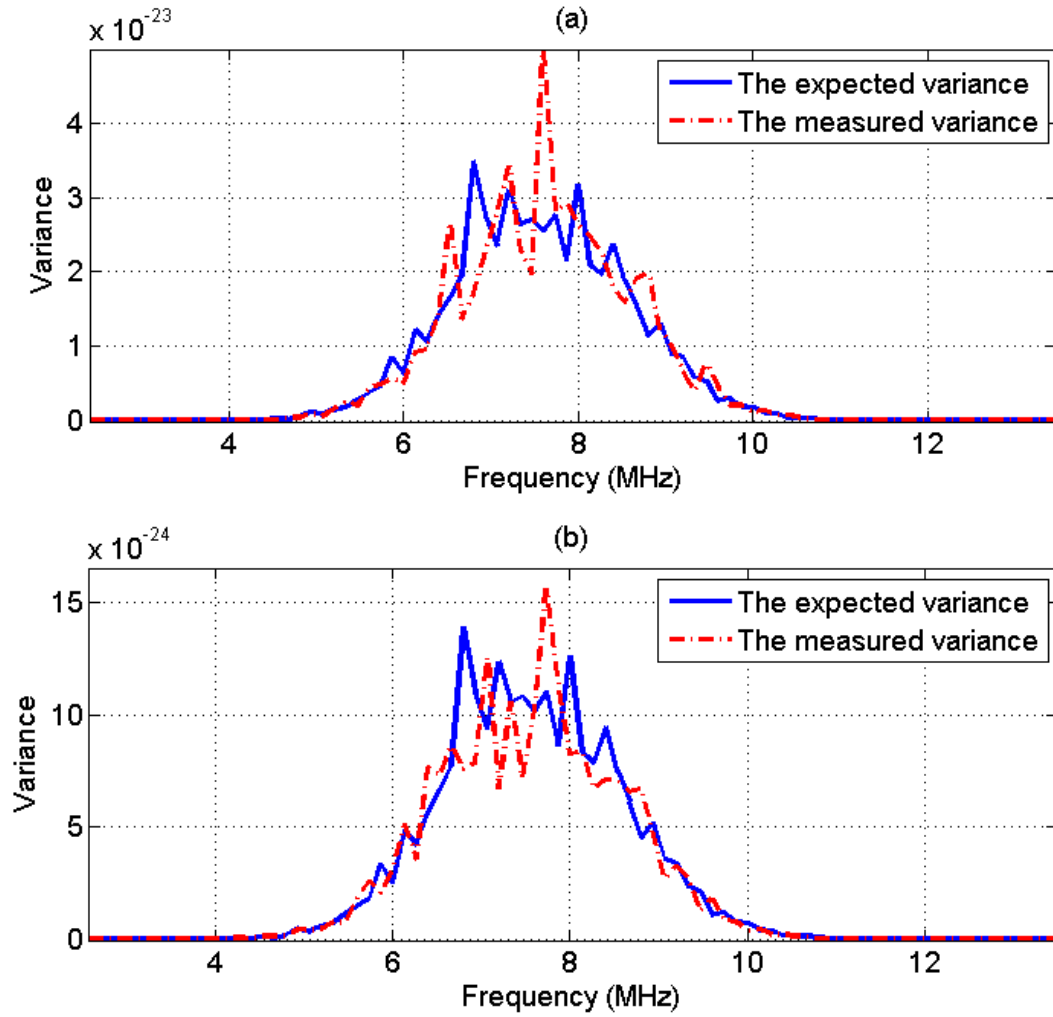


Figure 32 Plot of the expected variance and the measured variance of the power spectrum that is obtained by averaging (a) 10 periodograms and (b) 25 periodograms.

Equation (4.23) i.e. $\text{var}[S(f)] \approx \frac{(N_s + N_r)}{N_s N_r} S(f)^2$ states that the variance of the power

spectrum that is calculated by dividing the spectrum that is obtained from N_s averaged periodograms of the sample by the spectrum that is obtained from N_r averaged

periodograms of the reference, is equal to $\frac{(N_s + N_r)}{N_s N_r}$ multiplied by the square of the ratio of the expected power spectrum of the sample to the expected power spectrum of the reference. To show the validity of this equation, we calculated the variance of 30 spectra, each of which was obtained by dividing the spectrum of N_s averaged periodograms of the sample by the spectrum of N_r averaged periodograms of the reference. We estimated the ratio of the expected power spectrum of the sample by the expected power spectrum of the reference $S_s(f)^2$, by dividing the spectrum from 100 averaged periodograms of the sample by the spectrum of 100 averaged periodograms of the reference. Figure 33 (a) and (b) show the results obtained for when $N_s = N_r = 25$ and $N_s = N_r = 50$, respectively. Based on this figure, the expected variance $\frac{(N_s + N_r)}{N_s N_r} S(f)^2$ closely approximates the measured variance. It is also apparent the variance is smaller for when $N_s = N_r = 50$ compared the case when $N_s = N_r = 25$.

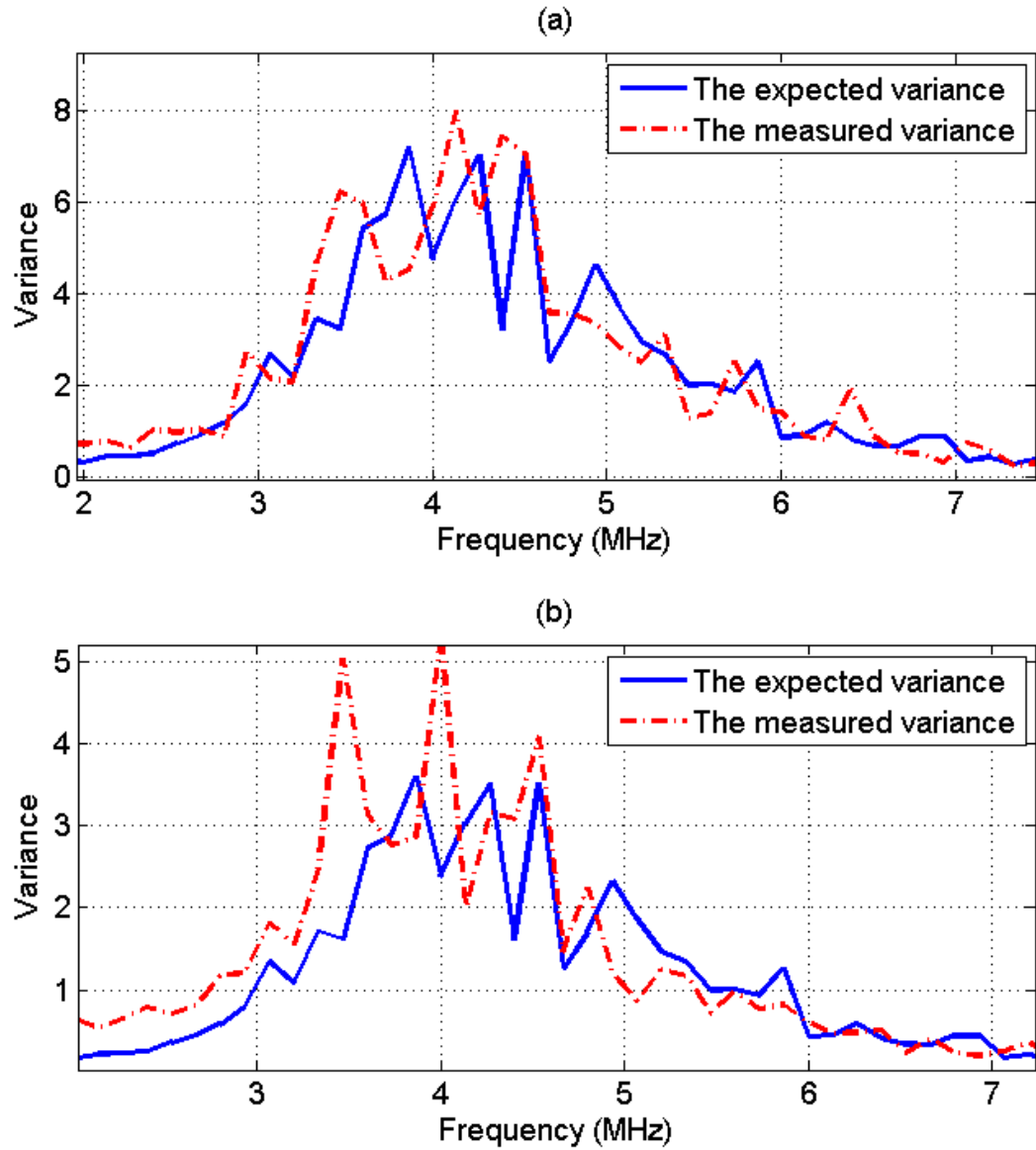


Figure 33 Plot of the expected variance and the measured variance of the power spectrum that is obtained by taking the ratio of (a) 25 averaged periodograms of the sample and 25 averaged periodograms of the reference (b) 50 averaged periodograms of the sample and 50 averaged periodograms of the reference

4.4.3 Validation of the spectral fit statistical analysis

Equation (4.25) i.e. $\text{var}\left[S_{\ln}(f_i)\right] \approx \frac{(N_s + N_r)}{N_s N_r}$ states that the variance of the power

spectrum that is obtained by taking the natural logarithm of the ratio of the averaged power spectrum of the sample (N_s periodograms) to the averaged power spectrum of the reference (N_r periodograms) is given by $\frac{(N_s + N_r)}{N_s N_r}$. To show the validity of this equation, we

calculated the variance of 30 spectra, each of which was obtained by dividing the spectrum from N_s averaged periodograms of the sample by the spectrum of N_r averaged periodograms of the reference and taking the natural logarithm of the result. Each periodogram is obtained from a time gated window that is 15 pulse lengths long. We estimated the ratio of the expected power spectrum of the sample by the expected power spectrum of the reference, by dividing the spectrum from 100 averaged periodograms of the sample by the spectrum of 100 averaged periodograms of the reference. Figure 34 (a) and (b) show the results obtained for when $N_s = N_r = 25$ and $N_s = N_r = 50$, respectively. Based on this figure, the expected variance $\frac{(N_s + N_r)}{N_s N_r}$ closely approximates the measured variance. It is also apparent that the variance is smaller for when $N_s = N_r = 50$ compared the case when $N_s = N_r = 25$.

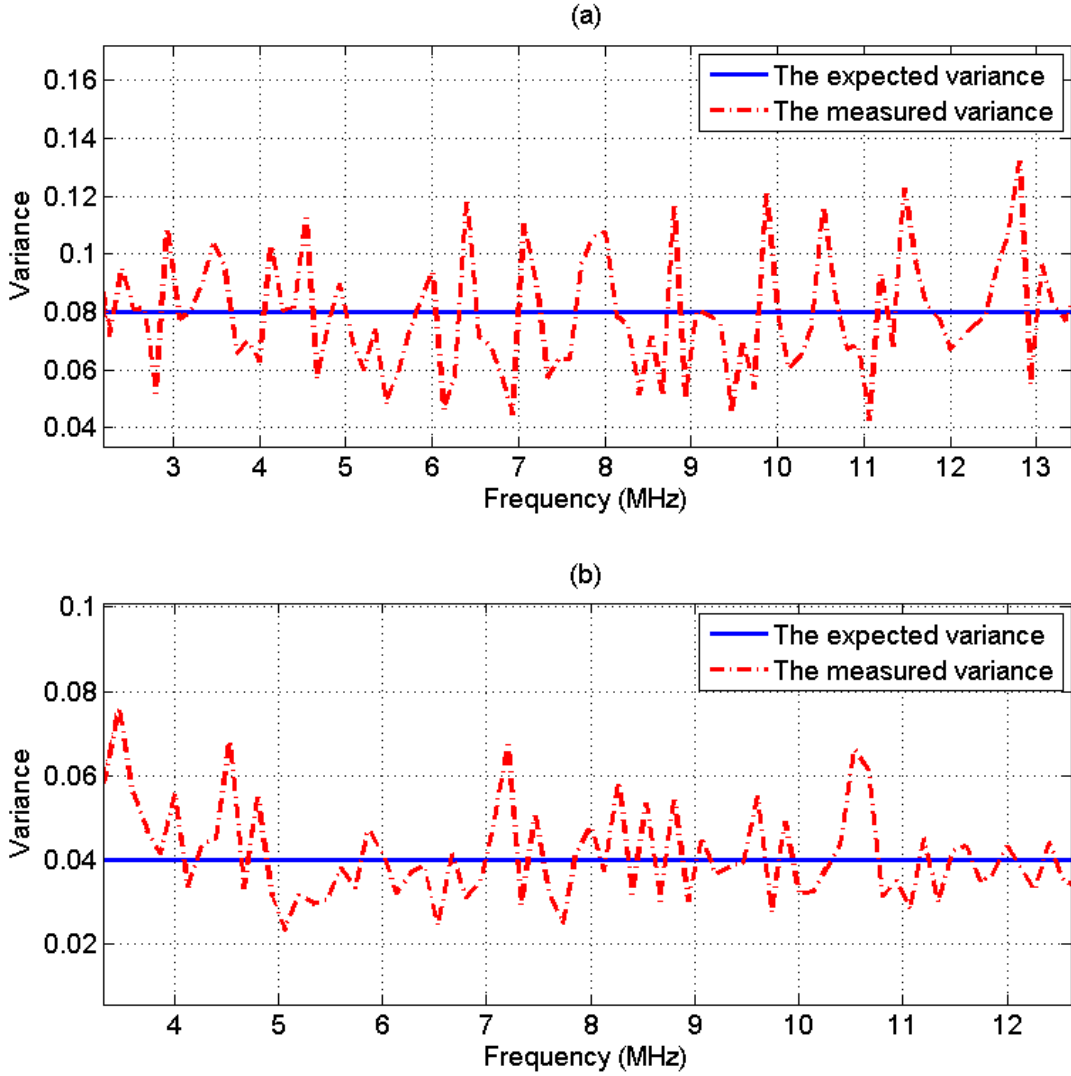


Figure 34 Plot of the expected variance and the measured variance of the power spectrum that is obtained by taking the natural logarithm of the ratio of (a) 25 averaged periodograms of the sample and 25 averaged periodograms of the reference (b) 50 averaged periodograms of the sample and 50 averaged periodograms of the reference

The variance in $d\alpha_s$, the estimate of the attenuation coefficient in the sample multiplied by the distance from the transducer to the center of the ROI, is equal to the variance in $d\Delta\alpha$ which is given by equation (4.27). As discussed before, given a tissue mimicking phantom

with a constant attenuation coefficient and an ultrasound system with a fixed bandwidth, the only parameter that affects the variance of the estimate $d\alpha_s$ is the ROI size, i.e. the number of averaged periodograms in the sample and the reference, and the size of the time gated window. To prove the validity of equation (4.27), we varied the ROI width from 10 to 100 independent echo lines in steps of 10 echo lines i.e. $N_s = N_r = 10:10:100$, and varied the ROI length from 1 to 20 pulse lengths in steps of 1 pulse length, and we obtained 30 estimates for each combination. At each combination of ROI length and ROI width, we used the measured usable frequency range to calculate the theoretical variance of the estimate $d\alpha_s$ using equation (4.27). The theoretical standard deviation (dB/MHz) is obtained by taking the square root of the result. At each combination of ROI length and ROI width, we compared the standard deviation of the 30 estimates of $d\alpha_s$ to the theoretical standard deviation. Figure 35 (a), (b), (c), and (d) shows plots of the measured and theoretical standard deviation of the estimate $d\alpha_s$ with respect to the number of independent of echoes per ROI for an ROI length of 5, 10, 15, and 20 pulse lengths, respectively. Based on this figure, the theoretical standard deviation in the estimate $d\alpha_s$ is very similar to the measured standard deviation. The slight difference between the measured and the theoretical standard deviation in Figure 35 (a) is probably due to the windowing effects which are more apparent at small time gated windows. These results validate equation (4.27).

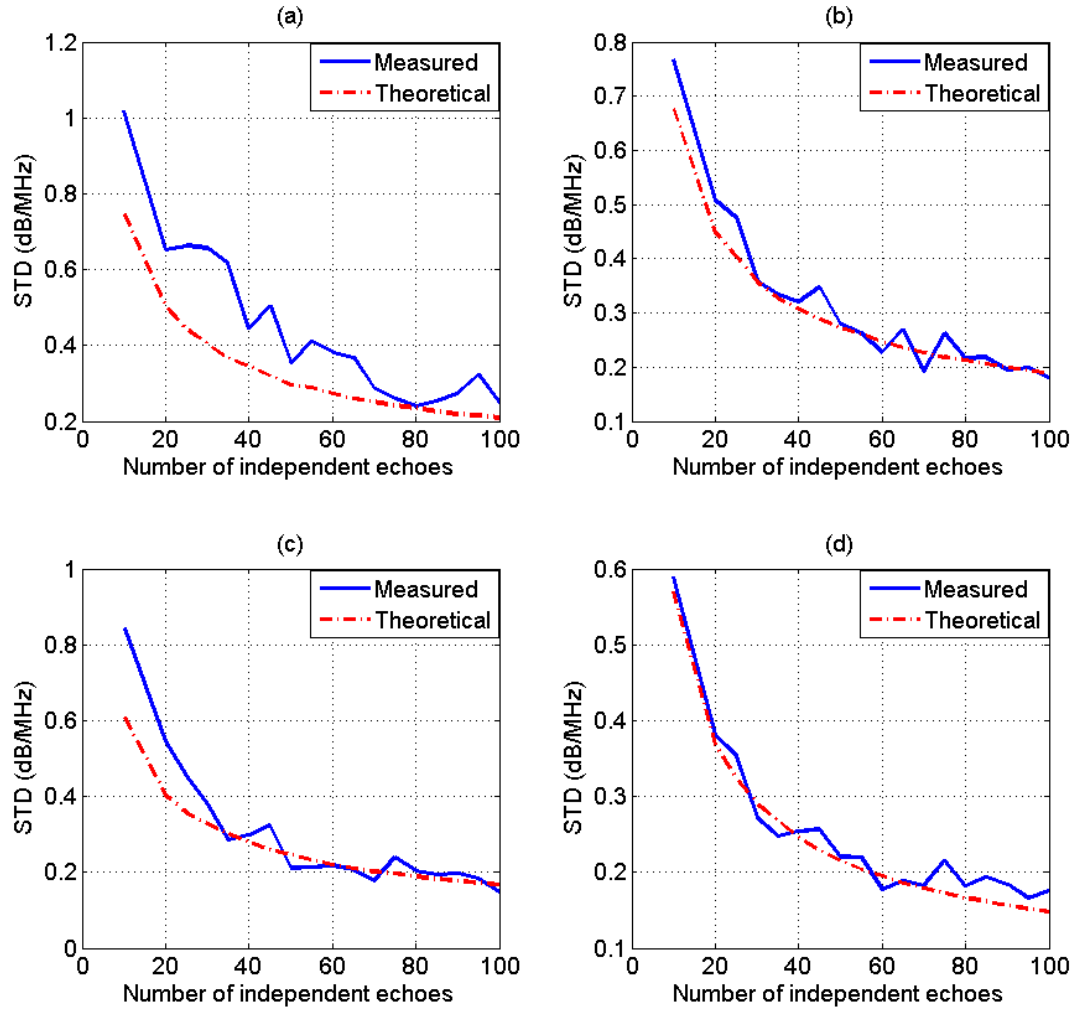


Figure 35 Plots of the measured and theoretical standard deviation of the estimate $d\alpha_s$, which was obtained using the spectral fit method with an ROI length of (a) 5 pulse lengths (b) 10 pulse lengths (c) 15 pulse lengths (d) 20 pulse lengths, with respect to the number of independent of echoes per ROI

4.4.4 Validation of the multiple filter statistical analysis

As discussed before, given a tissue mimicking phantom with a constant attenuation coefficient and an ultrasound system with a fixed bandwidth, the only parameter that affects

the variance of the estimate $d\alpha_s$ using the multiple filter method are the number of averaged periodograms of the sample and the reference, the size of the time gated window, and the number of Gaussian filters. The validation of equation (4.30) i.e.

$$\text{var}\left(S_{Gauss}(f_i)\right) = \frac{(N_s + N_r)}{N_s N_r} S_{Gauss}(f_i)^2 \quad \text{follows from equation (4.25) i.e.}$$

$$\text{var}\left[S_{\ln}(f_i)\right] \approx \frac{(N_s + N_r)}{N_s N_r} \text{ and the following equation [62]:}$$

$$\text{var}(aX) = a^2 \text{var}(X) \quad (4.41)$$

That is the variance of a random variable X multiplied by a constant a is simply the variance of the random variable multiplied by the constant squared. The validation of equation (4.32) is similar to the validation of equation (4.25) which was described in section 4.4.3.

To test the validity of equation (4.39), we varied the ROI width from 10 to 100 independent echo lines i.e. $N_s = N_r = 10:10:100$, the ROI length from 1 to 20 pulse lengths, and the number of Gaussian filters from 2 to 10 filters, and we obtained 30 estimates of $d\alpha_s$ for each combination. At each combination of ROI length, ROI width, and number of Gaussian filters, we used the measured usable frequency range to calculate the theoretical variance of the estimate $d\alpha_s$ using equation (4.39). The theoretical standard deviation (dB/MHz) is obtained by taking the square root of the result. At each combination of ROI length and ROI width, and number of Gaussian filters, we compared the standard deviation of the 30 estimates of $d\alpha_s$ to the theoretical standard deviation. Figure 36 (a), (b), (c), and (d) shows plots of the measured and theoretical standard deviation of the estimate $d\alpha_s$ with

respect to the number of independent of echoes per ROI for an ROI length of 5, 10, 15, and 20 pulse lengths, respectively and with 2 Gaussian filters. Figure 37 (a), (b), (c), and (d) shows plots of the measured and theoretical standard deviation of the estimate $d\alpha_s$ with respect to the number of independent of echoes per ROI for an ROI length of 5, 10, 15, and 20 pulse lengths, respectively and with 4 Gaussian filters. Based on these figures, the theoretical standard deviation in the estimate $d\alpha_s$ is very similar to the measured standard deviation. As mentioned before, the slight difference between the measured and the theoretical standard deviation in plots (a) is probably due to the windowing effects which are more apparent at small time gated windows.

By comparing Figure 36 and Figure 37, we observe that for a specific of ROI length and ROI width, the variance in the estimate of $d\alpha_s$ is smaller when the number of Gaussian filters is 2 compared to when the number of Gaussian filters is 4. To test the dependence of the multiple filter algorithm on the number of Gaussian filters, we fixed the ROI length to 15 pulse lengths, the ROI width to 60 independent echo lines, and we plotted the measured and theoretical standard deviation of the estimate $d\alpha_s$ with respect to the number of Gaussian filters as shown in Figure 38. Based on this figure, we observe that standard deviation in the estimate $d\alpha_s$ increases with increasing number of Gaussian filters. Therefore, the optimal number of independent Gaussian filters for the multiple filter algorithm is equal to 2.

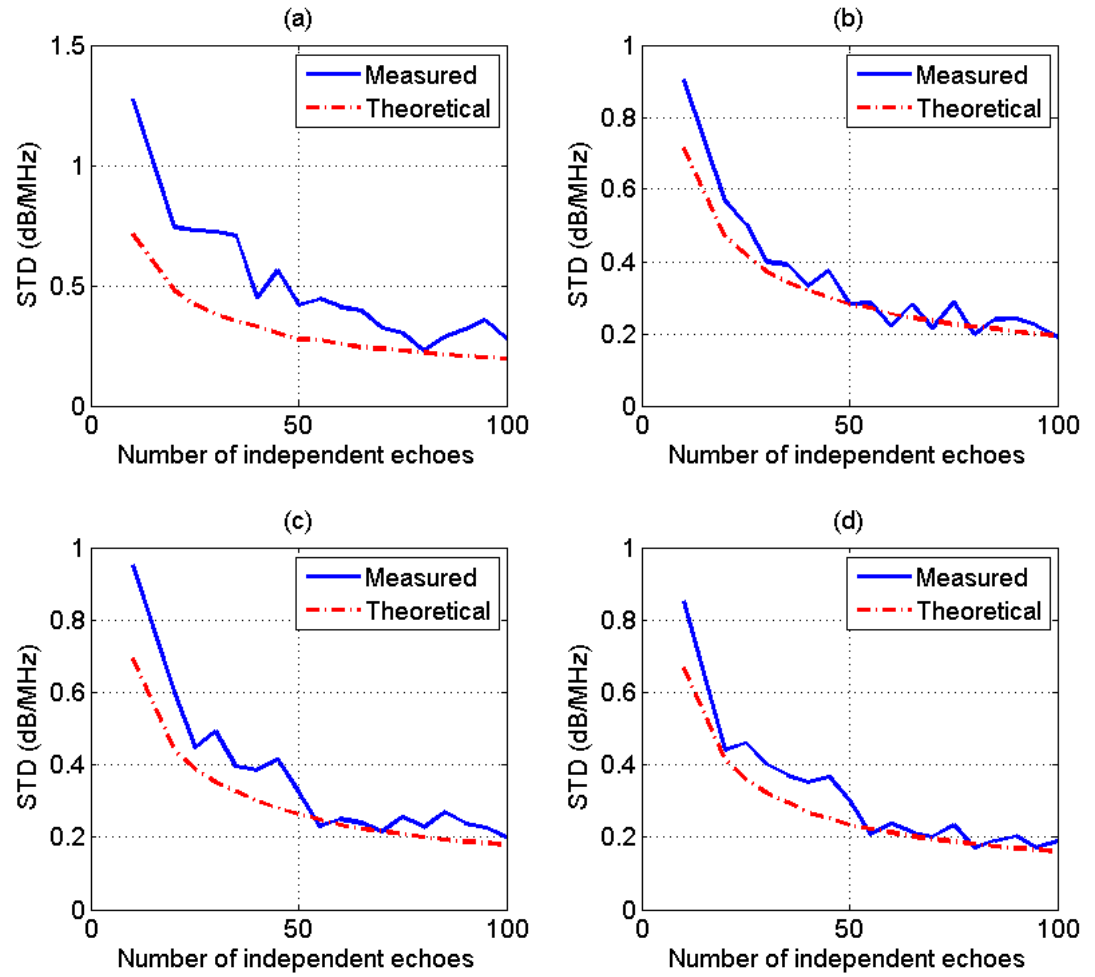


Figure 36 Plots of the measured and theoretical standard deviation of the estimate $d\alpha_s$, which was obtained using the multiple filter method with 2 Gaussian filters and an ROI length of (a) 5 pulse lengths (b) 10 pulse lengths (c) 15 pulse lengths (d) 20 pulse lengths, with respect to the number of independent of echoes per ROI

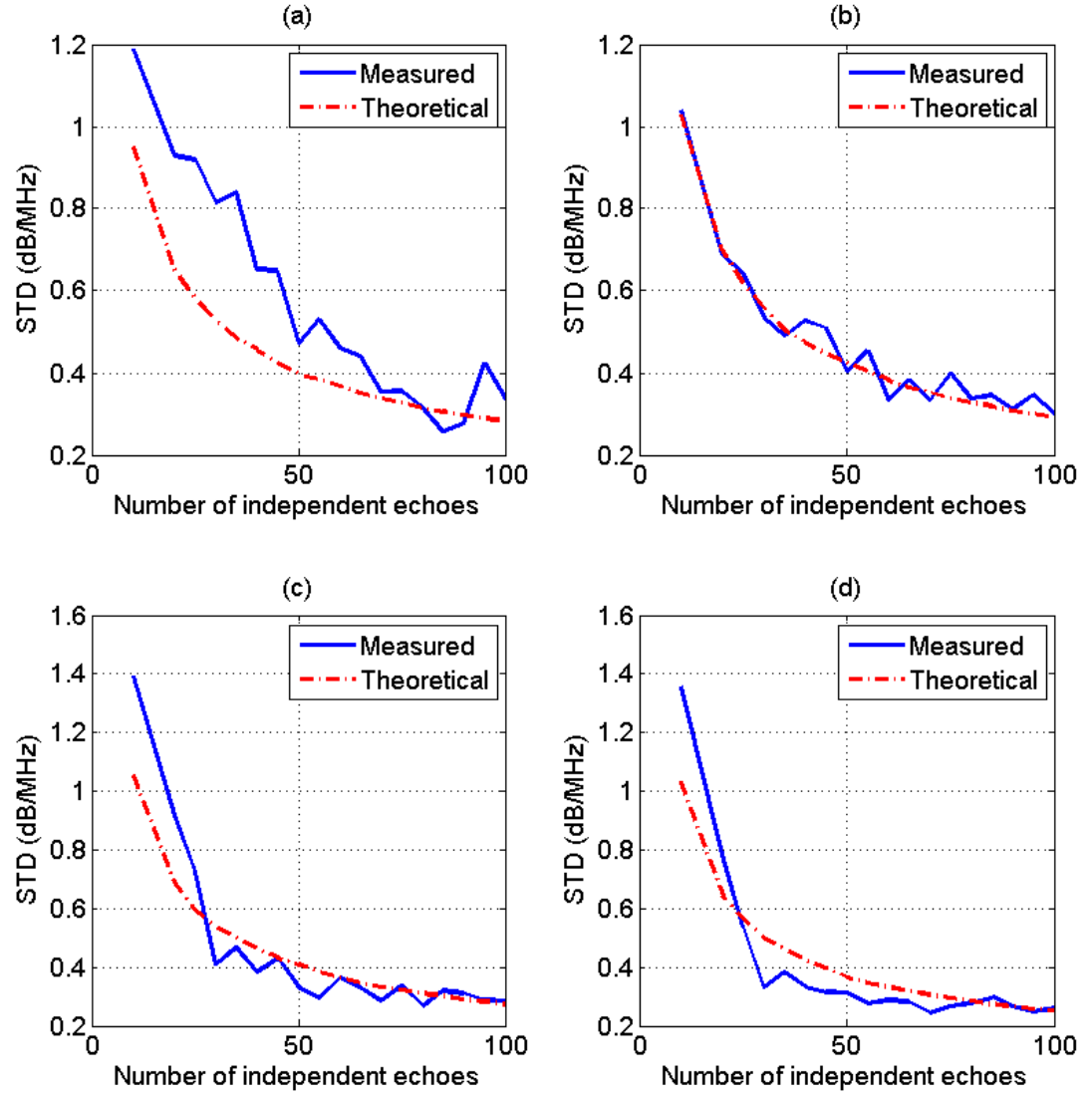


Figure 37 Plots of the measured and theoretical standard deviation of the estimate $d\alpha_s$, which was obtained using the multiple filter method with 4 Gaussian filters and an ROI length of (a) 5 pulse lengths (b) 10 pulse lengths (c) 15 pulse lengths (d) 20 pulse lengths, with respect to the number of independent of echoes per ROI

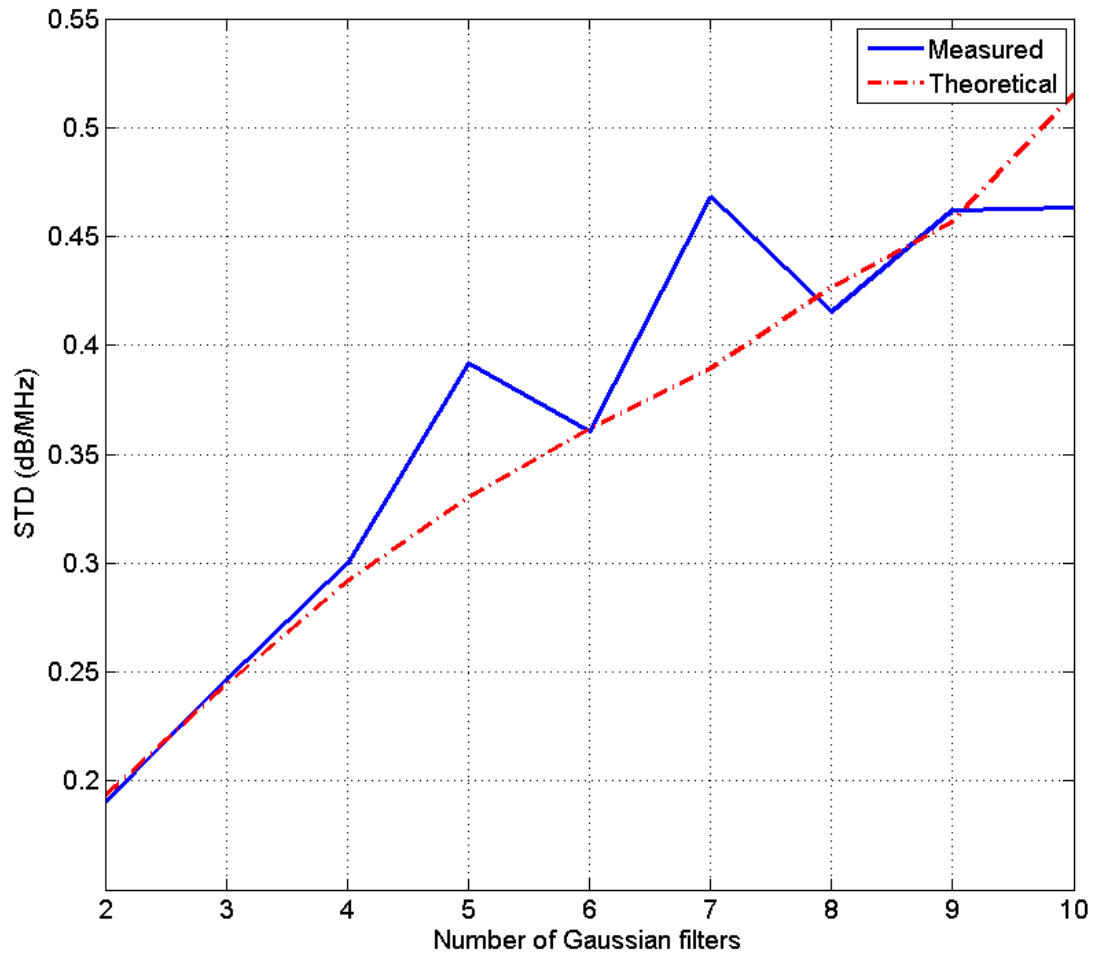


Figure 38 Plots of the measured and theoretical standard deviation of the estimate $d\alpha_s$, which was obtained using the multiple filter method with an ROI length of 10 pulse lengths and an ROI width of 60 independent echo lines, with respect to the number of Gaussian filters.

5 COMPARISON OF THE TWO PROPOSED ALGORITHMS FOR TOTAL ATTENUATION ESTIMATION

5.1 Comparison based on theory

The derived expressions for the variance in the ACEs that are obtained using the spectral fit method (equation (4.27)) and the multiple filter method (equation (4.39)) are not in closed form. In order to compare these two equations, we used the simulation data that was described in section 4.1.1 and we varied the axial ROI size from 5 pulse lengths to 20 pulse lengths, and the lateral ROI size from 10 to 100 independent echo lines. For each ROI, the corresponding parameters (the number of averaged spectra and the number of usable frequency components) were used in equation (4.27) and equation (4.39) to obtain the theoretical variance in the ACEs. Figure 5.1 shows plots of the theoretical standard deviation of the estimates $d\alpha_s$ versus the number of independent echoes per ROI for an axial ROI size of 5 pulse lengths, 10 pulse lengths, 15 pulse lengths, and 20 pulse lengths, respectively. Based on Figure 5.1, The STD in the ACEs that are obtained using the spectral fit method is comparable to STD in the ACEs that are obtained using the multiple filter method. Figure 5.1 also shows that for both attenuation estimation algorithms, the variance in the ACEs has a larger dependence on the lateral ROI size than the axial ROI size. For example, if the axial ROI size is doubled there is less than a 10% decrease in the STD of the ACEs, however; if the lateral ROI size is doubled the STD in the ACEs decreases by nearly 40%.

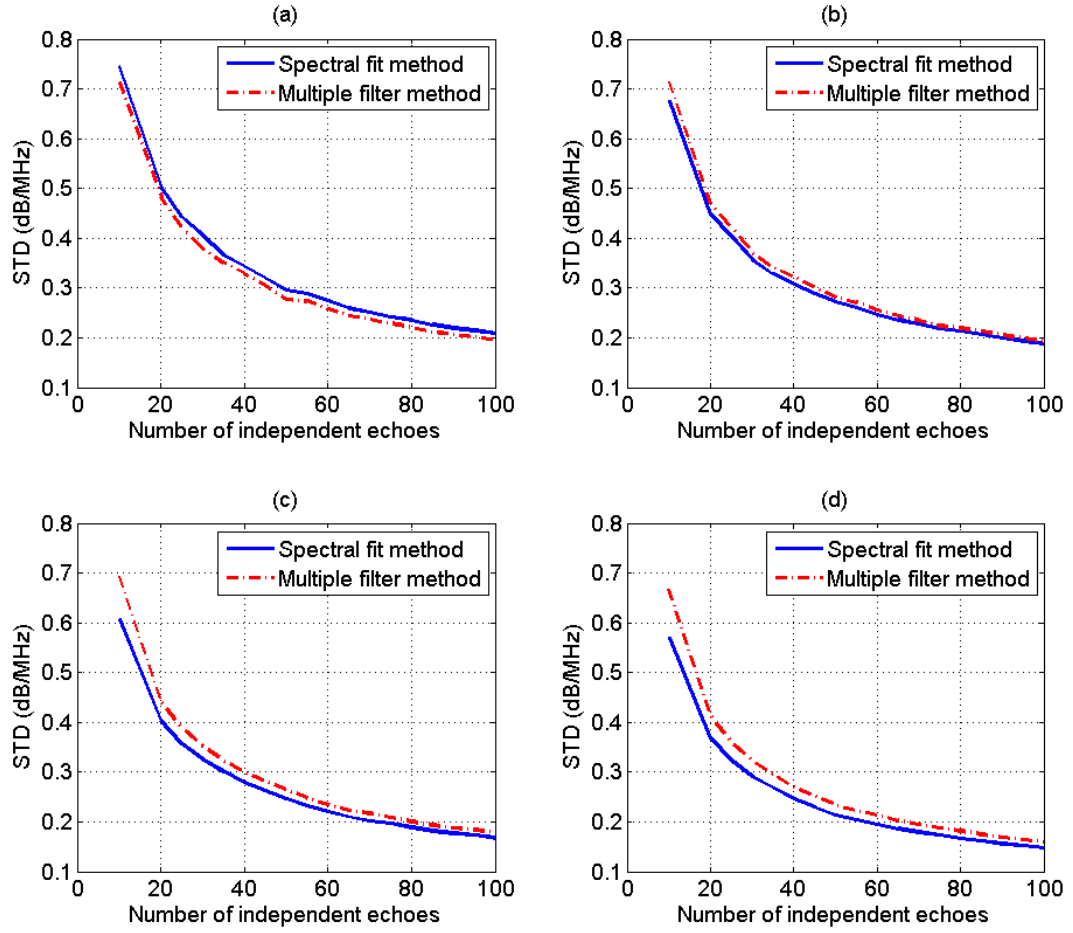


Figure 39 Plots of the theoretical standard deviation of the estimate $d\alpha_s$, which was obtained using spectral fit method and the multiple filter method with 2 Gaussian filters with an ROI length of (a) 5 pulse lengths (b) 10 pulse lengths (c) 15 pulse lengths (d) 20 pulse lengths, with respect to the number of independent of echoes per ROI

5.2 Comparison using simulations

In this section we use computer simulations to compare the spectral fit method and the multiple filter method. In section 4.4.4, we concluded that for the multiple filter method, the optimal number of independent Gaussian filters is 2. However, using overlapping Gaussian filters with large bandwidths may give better results than using only two independent

Gaussian filters. Due to the correlation in the spectra that results from using overlapping Gaussian filters, it is difficult to obtain an expression for the variance in the ACEs. This variance however, can be explored using computer simulations.

We used the simulation data that was described in section 4.1.1 and we varied the lateral ROI size from 10 to 100 independent echo lines i.e. $N_s = N_r = 10:10:100$, the axial ROI size from 1 to 20 pulse lengths, and we obtained 30 estimates of $d\alpha_s$ using the spectral fit method, the multiple filter method with 2 independent Gaussian filters, and the multiple filter method with 4 overlapping Gaussian filters. In the latter case which was used by Bigelow in previous total attenuation studies [29, 66, 67], three of the four Gaussian filters have center frequencies that form 4 equally spaced intervals within the usable frequency range. The three Gaussian filters have the same 3-dB percent bandwidth. The 3-dB percent bandwidth was chosen such that the minimum frequency in the usable frequency range corresponds to -15dB of the power spectrum that results from multiplying the power spectrum by the Gaussian filter that has the smallest center frequency. The fourth Gaussian filter spans the entire usable frequency range and has a center frequency that corresponds to the middle of the usable frequency range, and a variance that corresponds to the variance of a Gaussian function that fits the power spectrum of the sample. Using each method and at each combination of ROI length and ROI width, we compared the bias, the standard deviation, and the MSE in the 30 estimates of $d\alpha_s$ that are obtained using each method. In this study, we calculated the MSE in order to determine the overall performance of the algorithms. Knowing the expected MSE for a specific ROI size gives insight into how well we can trust the total attenuation coefficient estimate if only one ROI is available.

Figure 40 (a), (b), and (c) shows plots of the bias, STD, and MSE, respectively, of the estimates $d\alpha_s$ versus the number of independent echoes per ROI for and ROI length of 10 pulse lengths. Similarly, Figure 41 (a), (b), and (c) shows plots of the bias, STD, and MSE, respectively, of the estimates $d\alpha_s$ versus the number of pulse lengths per ROI for and ROI that contains 50 independent echo lines. Based on these 2 figures, the MSE is comparable for both the spectral fit method and the multiple filter method with 2 independent Gaussian filters, with the spectral fit method having a slightly smaller STD and a slightly larger bias compared to the 2 independent filter method. These two figures also show in the multiple filter method, using 3 overlapping Gaussian filters and a fourth filter that spans the entire usable frequency range gives better results than using only 2 independent Gaussian filters. This latter result demonstrates that the multiple filter method could potentially be improved to yield smaller errors in the ACEs. This will be discussed further in the discussion section.

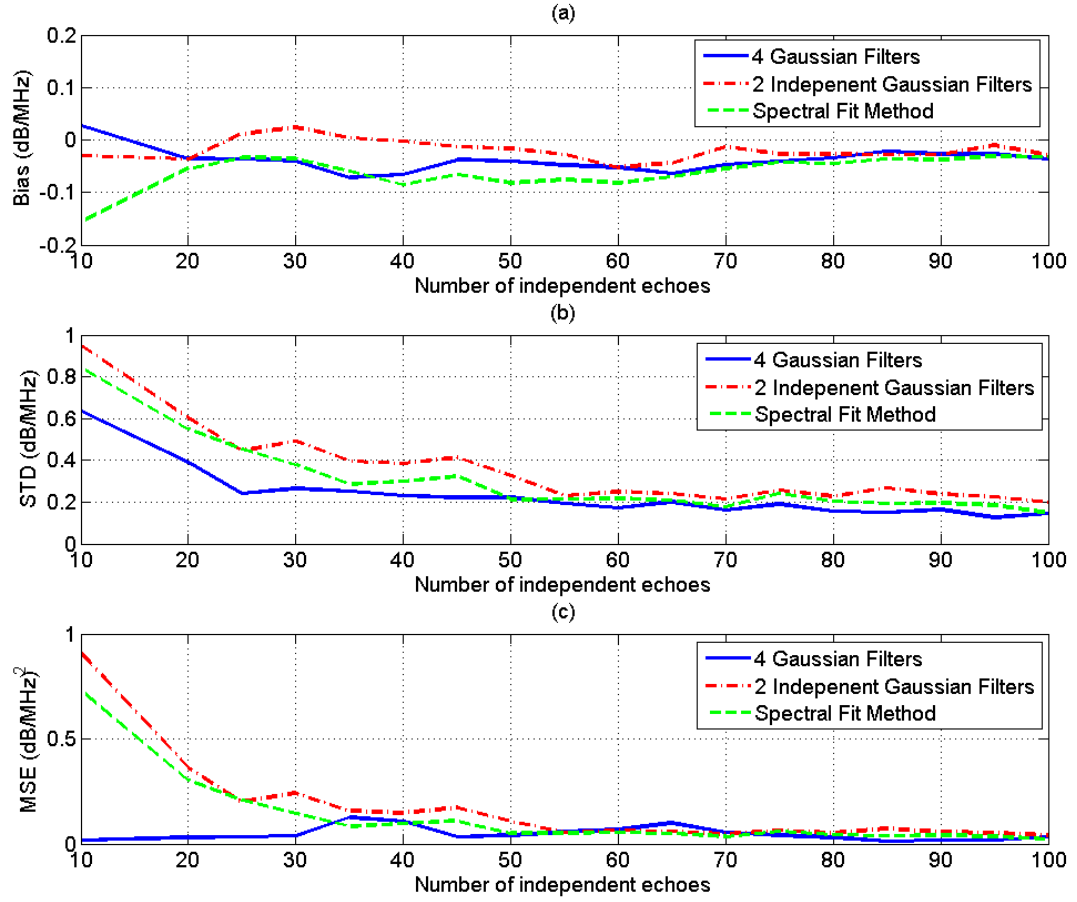


Figure 40 Plots of the (a) bias (b) STD, and (c) MSE of the estimate $d\alpha_s$, which was obtained using the multiple filter method with 3 independent Gaussian filters, the multiple filter method with 3 Gaussian filters, the multiple filter method with two independent filters, and the spectral fit method, with respect to the number of independent of echoes per ROI for an ROI length of 10 pulse lengths

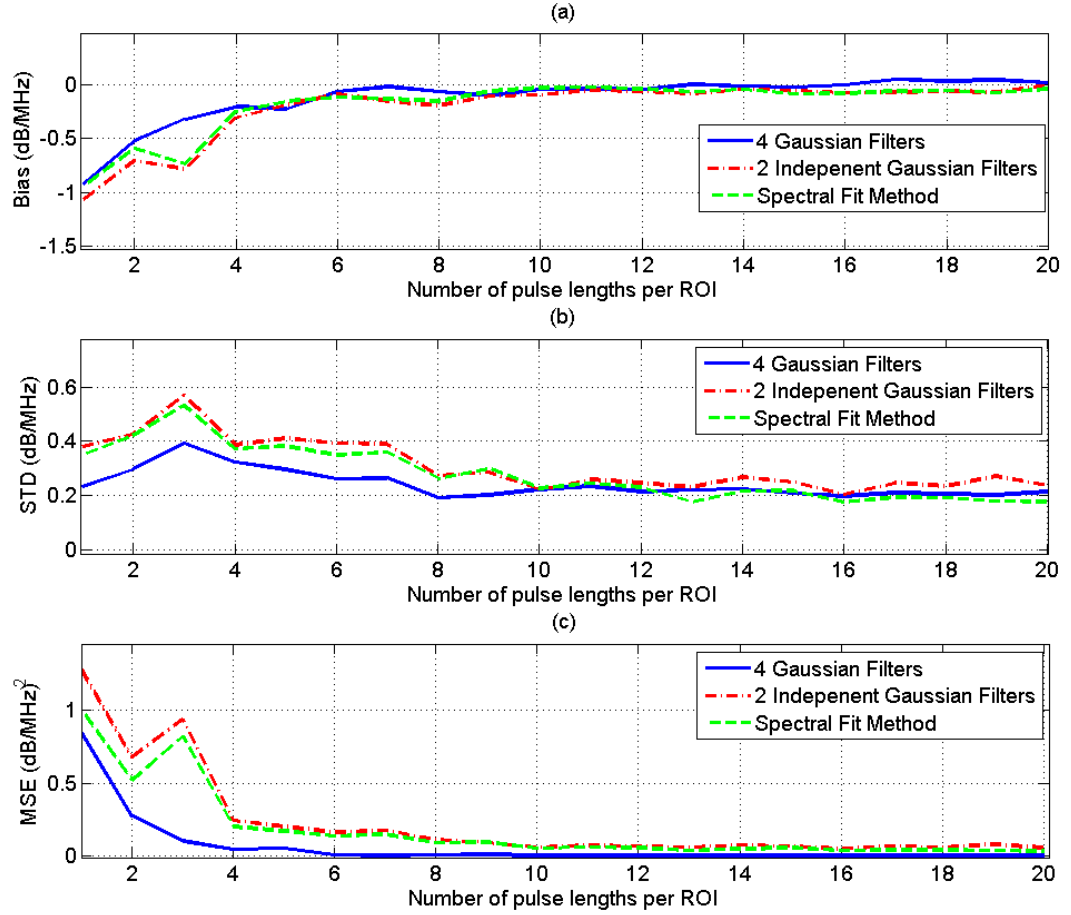


Figure 41 Plots of the (a) bias (b) STD, and (c) MSE of the estimate $d\alpha_s$, which was obtained using the multiple filter method with 3 Gaussian filters, the multiple filter method with two independent filters, and the spectral fit method, with respect to the number of pulse lengths per ROI for an ROI that contains 50 independent echo lines

5.3 Comparison using a spherically focused transducer

The same methods that were compared in the simulations were also compared using two TMPs (Gammex 406 LE 0.7, Gammex 406 LE 0.5) that had attenuation coefficient slopes 0.7 dB/cm-MHz and 0.5 dB/cm-MHz, respectively. The scattering targets in the two phantoms are glass beads (160 beads/mm³) with a mean diameter of 35 μm . The phantom

with the 0.7 dB/cm-MHz attenuation was chosen as the sample and the phantom with the 0.5 dB/cm-MHz phantom was chosen as the reference. The two phantoms were scanned using a spherically focused transducer (5.14 cm focal length, $f/4$, and 7.5 MHz center frequency). The transducer was translated horizontally at 1 mm increments and 1 RF echo was obtained at each position. The step size of 1 mm is larger than the beamwidth of the transducer which was measured to be approximately 0.837 mm. A total of 225 echoes were obtained for the sample and 45 RF echoes from the reference. Using a hydrophone, we measured the pulse length of the transducer and found it to be approximately equal to 0.274 mm.

To compare the spectral fit method to the multiple filter method, we varied the ROI width from 5 to 45 independent echo lines i.e. $N_s = N_r = 5:2:45$, the ROI length from 1 to 20 pulse lengths, and we obtained 5 estimates of $d\alpha_s$ for each combination using the spectral fit method, the multiple filter method with 2 independent Gaussian filters, and the multiple filter method with 4 overlapping Gaussian filters (see section 5.2). At each combination of ROI length and ROI width, we compared the bias, the standard deviation, and the MSE between the 5 estimates of $d\alpha_s$ that were obtained using each method.

Figure 42 (a), (b), and (c) show plots of the bias, STD, and MSE, respectively, of the estimates $d\alpha_s$ versus the number of independent echoes per ROI for and ROI length of 10 pulse lengths. Similarly, Figure 43 (a), (b), and (c) show plots of the bias, STD, and MSE, respectively, of the estimates $d\alpha_s$ versus the number of pulse lengths per ROI for and ROI that contains 45 independent echo lines. Based on these two figures, the spectral fit method and the multiple filter method with two independent Gaussian filters have comparable bias, STD, and MSE in the ACEs. A similar behavior was observed in the simulations. It is also

apparent from the figure that the multiple filter method with 4 overlapping Gaussian filters has a smaller bias in the ACEs compared to the spectral fit method and multiple filter method with 2 independent Gaussian filters. However, unlike the simulation results, the multiple filter method with 4 overlapping Gaussian filters has a larger STD in the ACEs compared to the spectral fit method and the multiple filter method with 2 independent Gaussian filters. This could be contributed to the fact that only 5 estimates were used to calculate the STD in the ACEs. 5 estimates may be inadequate to quantify the standard deviation in the ACEs. Another difference between the simulation results and the SPT results is that for a given ROI size, the STD in the estimates that were obtained using the simulations is larger than the STD in the estimates that were obtained using the SPT. This behavior will be explored in the discussion section.

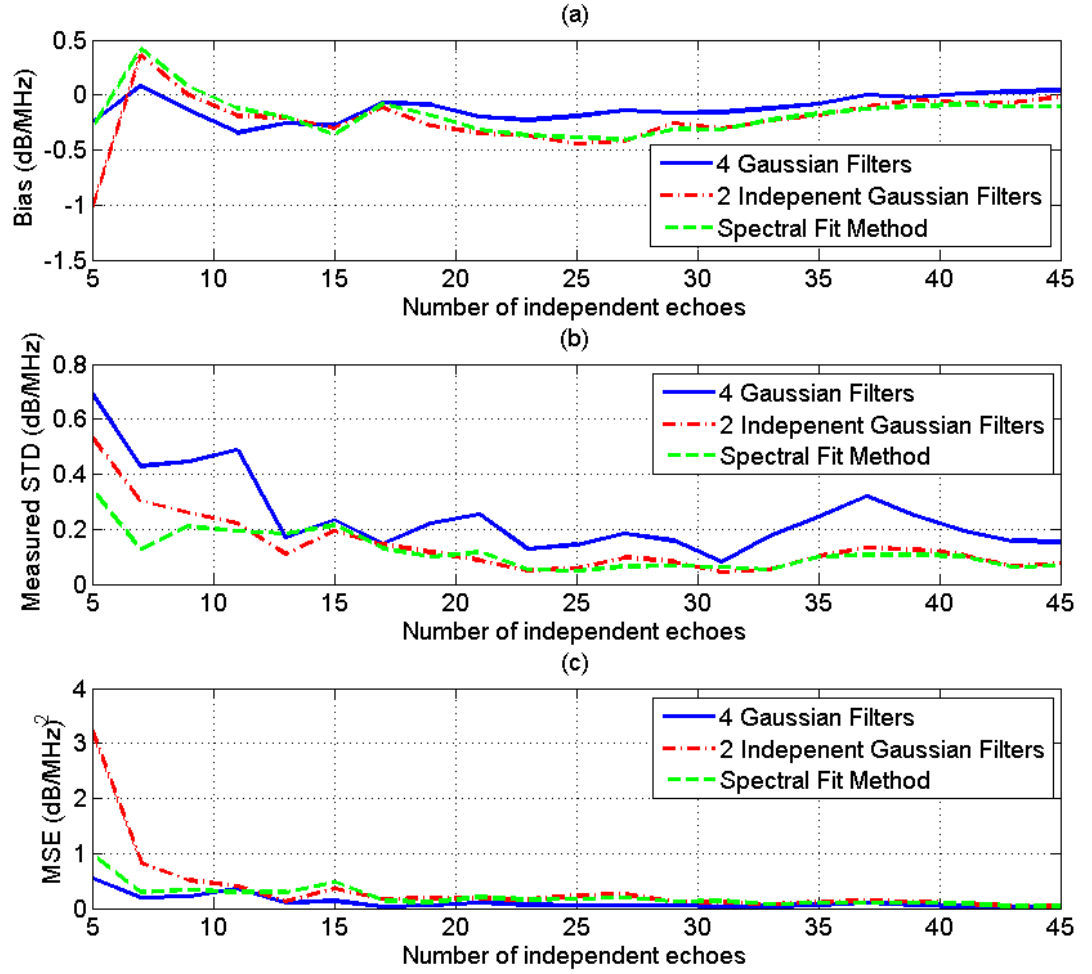


Figure 42 Plots of the (a) bias (b) STD, and (c) MSE of the estimate $d\alpha_s$, which was obtained using the multiple filter method with 3 independent Gaussian filters, the multiple filter method with 3 Gaussian filters, the multiple filter method with two independent filters, and the spectral fit method, with respect to the number of independent of echoes per ROI for an ROI length of 10 pulse lengths

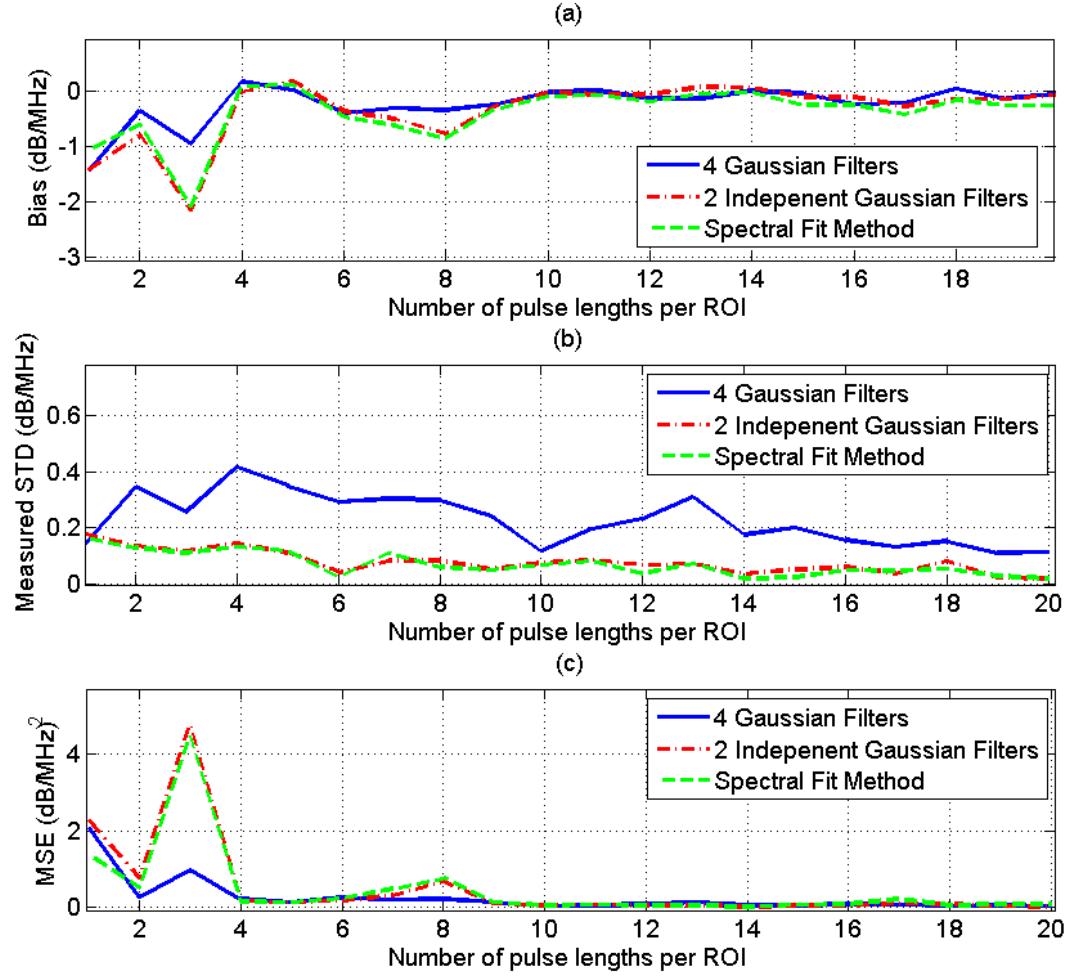


Figure 43 Plots of the (a) bias (b) STD, and (c) MSE of the estimate $d\alpha_s$, which was obtained using the multiple filter method with 3 Gaussian filters, the multiple filter method with two independent filters, and the spectral fit method, with respect to the number of pulse lengths per ROI for an ROI that contains 45 independent echo lines

5.4 Comparison using a clinical array transducer

We used a clinical array transducer (~7 MHz, L8-3 Linear Array Transducer) driven by a clinical ultrasound system (z.one Ultrasound System, ZONARE Medical Systems, Inc.) to obtain 10 RF data sets from the 0.7 dB/cm-MHz phantom and 1 RF data set from the 0.5

dB/cm-MHz phantom that were described in section 5.3. Each set had 60 independent echo lines. To compare the spectral fit method to the multiple filter method, we varied the ROI width from 10 to 60 independent echo lines i.e. $N_s = N_r = 10:10:60$, the ROI length from 1 to 20 pulse lengths, and we obtained 10 estimates of $d\alpha_s$ for each combination using each method. At each combination of ROI length and ROI width, we compared the bias, the standard deviation, and the MSE between the 10 estimates of $d\alpha_s$ that were obtained using the spectral fit method, the multiple filter method with 2 independent Gaussian filters, and the multiple filter method with 4 overlapping Gaussian filters (as was done in the simulations in section 5.2). At each combination of ROI length and ROI width, we compared the bias, the standard deviation, and the MSE between the 10 estimates of $d\alpha_s$ that were obtained using each method.

Figure 42 (a), (b), and (c) shows plots of the bias, STD, and MSE, respectively, of the estimates $d\alpha_s$ versus the number of independent echoes per ROI for an ROI length of 12 pulse lengths. Similarly, Figure 43 (a), (b), and (c) shows plots of the bias, STD, and MSE, respectively, of the estimates $d\alpha_s$ versus the number of pulse lengths per ROI for an ROI that contains 60 independent echo lines. These two figures show similar results to those that were obtained from the simulation data in section 5.2. One major difference however, is that for a given ROI size, the STD in the estimates that were obtained using the clinical array transducer is larger than the STD that is obtained in the simulations and larger than the STD in the estimates that were obtained using spherically focused transducer. This behavior will be explored in the discussion section.

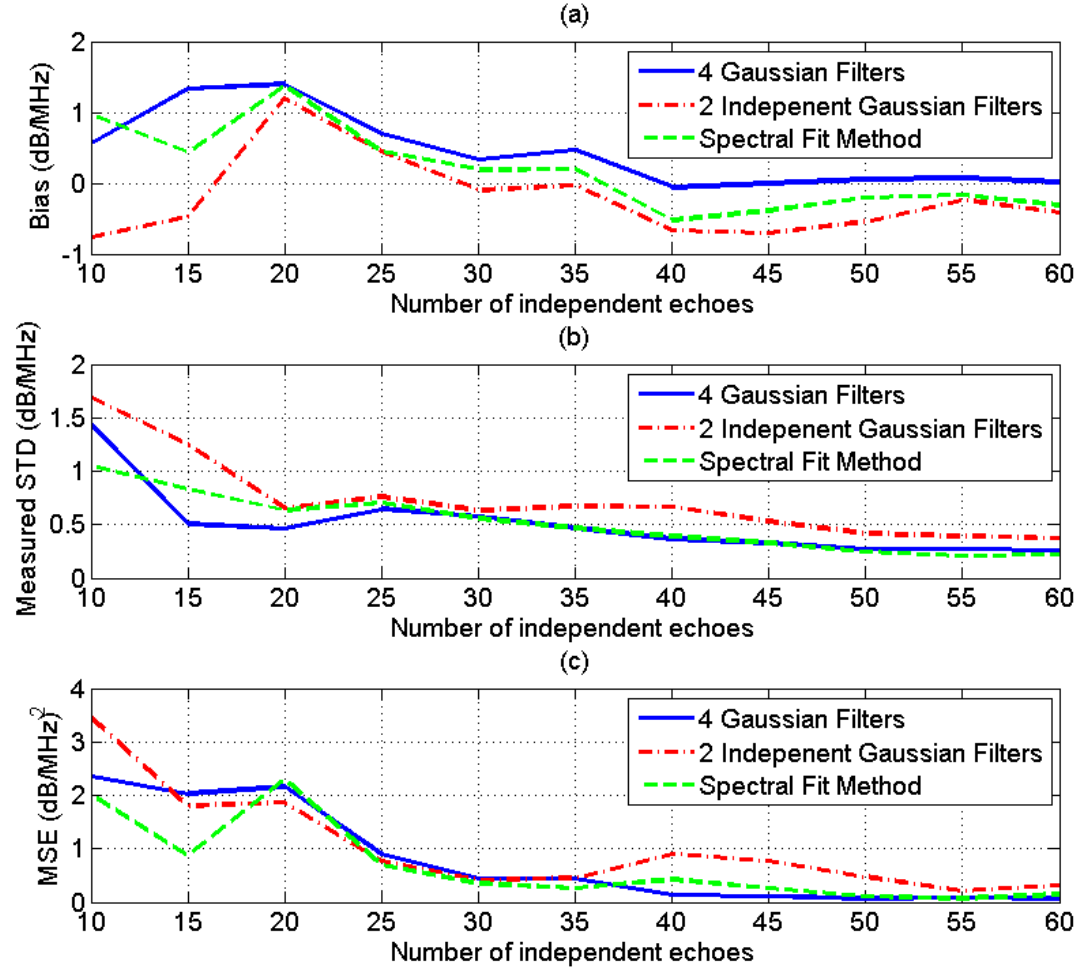


Figure 44 Plots of the (a) bias (b) STD, and (c) MSE of the estimate $d\alpha_s$, which was obtained using the multiple filter method with 3 independent Gaussian filters, the multiple filter method with 3 Gaussian filters, the multiple filter method with two independent filters, and the spectral fit method, with respect to the number of independent of echoes per ROI for an ROI length of 12 pulse lengths

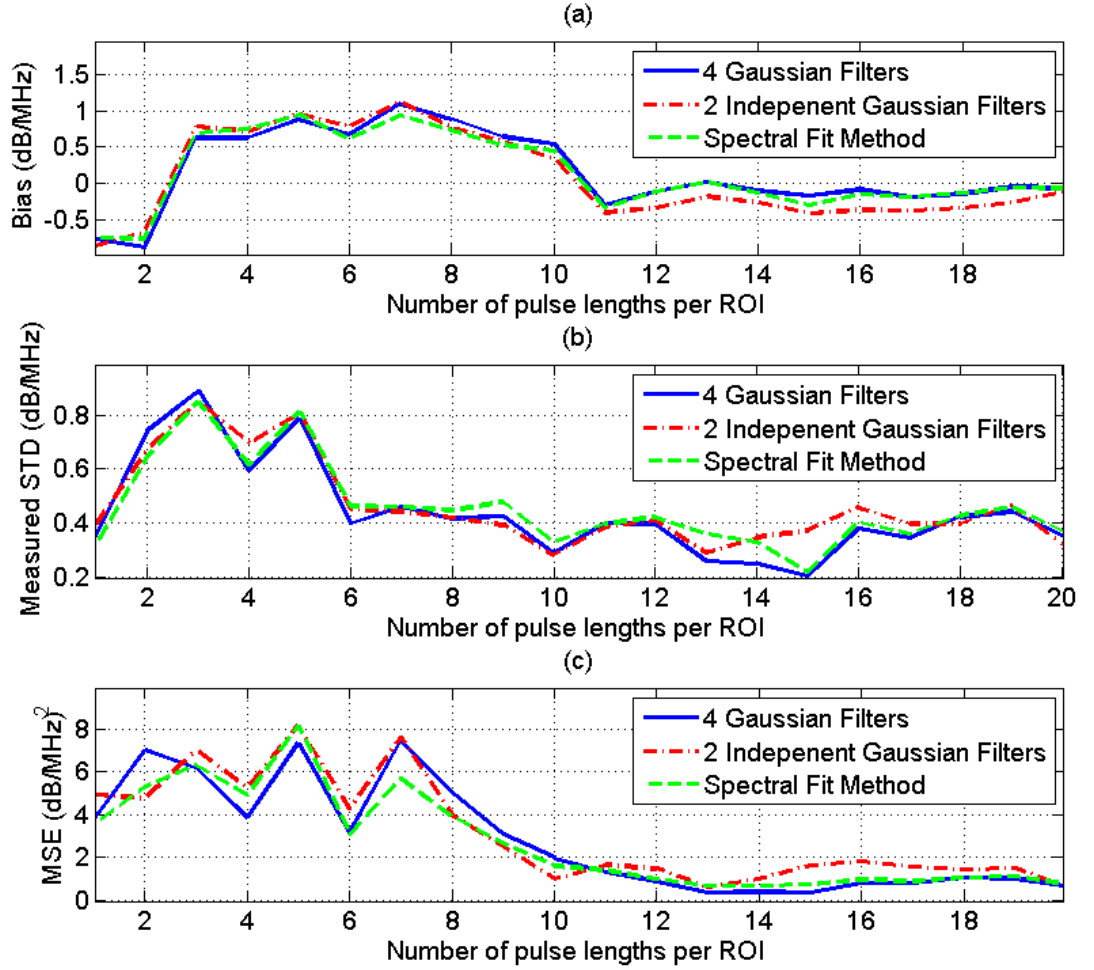


Figure 45 Plots of the (a) bias (b) STD, and (c) MSE of the estimate $d\alpha_s$, which was obtained using the multiple filter method with 3 Gaussian filters, the multiple filter method with two independent filters, and the spectral fit method, with respect to the number of pulse lengths per ROI for an ROI that contains 60 independent echo lines

5.5 Frequency dependence of the backscatter

In the derivation of the spectral fit method and the multiple filter method, we assumed a Gaussian Form Factor for the backscatter, i.e. $F_s(f, a_{\text{eff}_s}) \propto \exp(-Bf^2)$. This form factor has a frequency dependence of a power of 2. In soft tissues however, the frequency

dependence of the backscatter Form Factor may deviate slightly from a power of 2. In this case, it is important to know which of total attenuation estimation methods is less sensitive to a deviation from a power of 2 frequency dependence. In order to explore this, we used computer simulations (with the same transducer properties as in section 4.1.1) to generate 5 sample RF backscattered data sets. The medium scattering properties are the same as those in the simulation data that was described in section 4.1.1, with the exception of the frequency dependence of the backscatter. The 5 sample RF data sets have a power frequency dependence of 1.8, 1.9, 2, 1.1, and 1.2, respectively. We set the axial ROI size to 10 pulse lengths, and the lateral ROI size to 50 independent echo lines, and we obtained 30 estimates of $d\alpha_s$ using the spectral fit method and the multiple filter method with two independent Gaussian filters.

Figure 46 (a) and Figure 46 (b) show plots of the percent relative error and the standard deviation in the estimates of $d\alpha_s$, respectively, versus the frequency dependence of the backscatter. Based on this figure, both the spectral fit method and the multiple filter method are insensitive to a deviation from a power of two frequency dependence of the backscatter. This figure also shows that the multiple filter method has a slightly smaller bias and a slightly larger STD compared to the spectral fit method. A similar behavior was observed when the two algorithms were compared using the simulation in section 5.2.

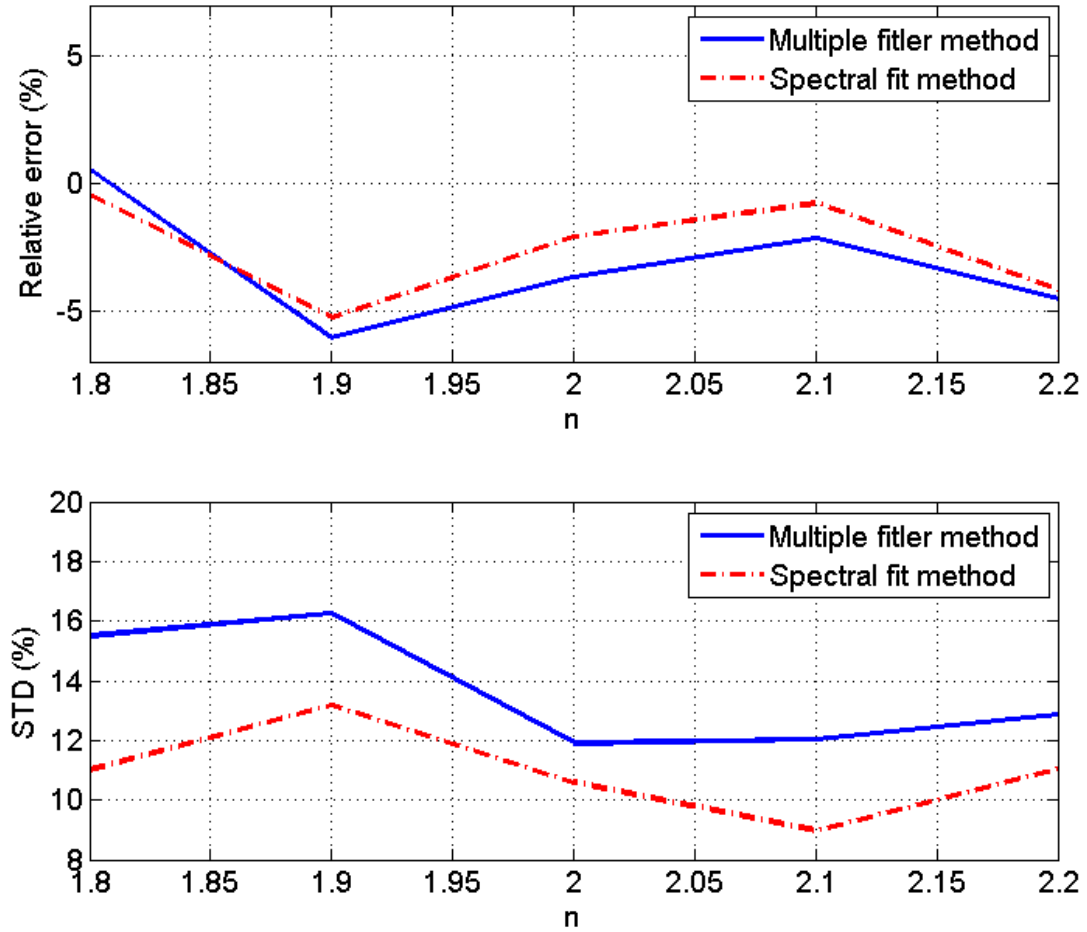


Figure 46 Plot of (a) the relative error and (b) the standard deviation in the estimates of $d\alpha_s$ versus the frequency dependence of the backscatter

5.6 Discussion

In this chapter, we compared the spectral fit method and the multiple filter method. The theoretical results showed that for a given ROI size, both the spectral fit method and the multiple filter method with 2 independent Gaussian filters yield comparable results in terms of the bias and the standard deviation of the total attenuation coefficient estimates. These results were validated using computer simulations and experiments on tissue mimicking

phantoms with a spherically focused transducer and a clinical array transducer. We have also shown that for the multiple filter method, using 3 overlapping Gaussian filters and a fourth Gaussian filter that spans the entire frequency range gives comparable or better results to using 2 independent Gaussian filters. However, we have shown in section 4.4.4 (Figure 38) that the optimal number of independent Gaussian filters in the multiple filter method is 2; therefore using two Gaussian filters with a certain amount of overlap and a third filter that spans the entire frequency ranges may give better results than using 3 overlapping Gaussian filters and a fourth Gaussian filter that spans the entire frequency range. A careful study must be done to find the optimal amount of overlap between the two Gaussian filters, and to find the optimal location of their center frequencies within the usable frequency range. The study could be done by modifying equation (4.38) to include the covariance between the random variables $a(1)$ and $a(2)$ (see equation (4.35)) which result from the first and the second Gaussian filters, respectively. The study may be complicated by the fact that the amount of overlap between two the Gaussian filters must be translated into a covariance between the random variables $a(1)$ and $a(2)$. However, computer simulations may be used to explore these issues. Based on this discussion, it is safe to say that the multiple filter method is a better choice than the spectral fit method for total attenuation estimation.

We have also shown that for both attenuation estimation algorithms, the variance in the ACEs has a larger dependence on the lateral ROI size than the axial ROI size. Furthermore, for a given ROI size, the STD in the estimates that were obtained using the clinical array transducer is larger than the STD that is obtained in the simulations and the STD in the estimates that were obtained using spherically focused transducer. To explore this further, we plotted the normalized power spectra that were obtained using the Gaussian focused beam in

the simulations, the spherically focused transducer, and the clinical array transducer in the phantom experiments as shown in Figure 47. We observed that the bandwidth of the clinical array transducer is smaller than the bandwidth of the Gaussian focused beam in the simulations, and that the bandwidth in the simulations is smaller than the bandwidth of the spherically focused transducer. A small bandwidth implies that the usable frequency range is small, and therefore the spacing between the center frequencies of the applied Gaussian filters is also small. When the center frequencies of the Gaussian filters are too close, the fit of the line equation given by (4.17) is less accurate because there is not a significant difference between the Gaussian center frequencies \tilde{f}_c .

The results of this chapter demonstrate that the multiple filter method or the spectral fit method could potentially be used to compensate for the total attenuation leading to a ROI in tissue. Compensating for the total attenuation leading an ROI within the cervix of pregnant patients will open doors to estimating acoustic parameters such as the backscatter coefficient, the scatterer size, and the ratio of coherent to incoherent scattering intensity. The backscatter coefficient has been shown to decrease with decreasing collagen concentration [35] and therefore the backscatter coefficient from the cervix may decrease as the cervix ripens and the collagen concentration decreases. The scatterer number density may decrease as the collagen fibril concentration decreases with increasing gestation. The collagen fibrils are highly organized at the beginning of pregnancy and they become more disorganized as the cervix ripens and prepares for delivery. This could lead to a lower ratio of coherent to incoherent scattering close to delivery compared to earlier stages of pregnancy.

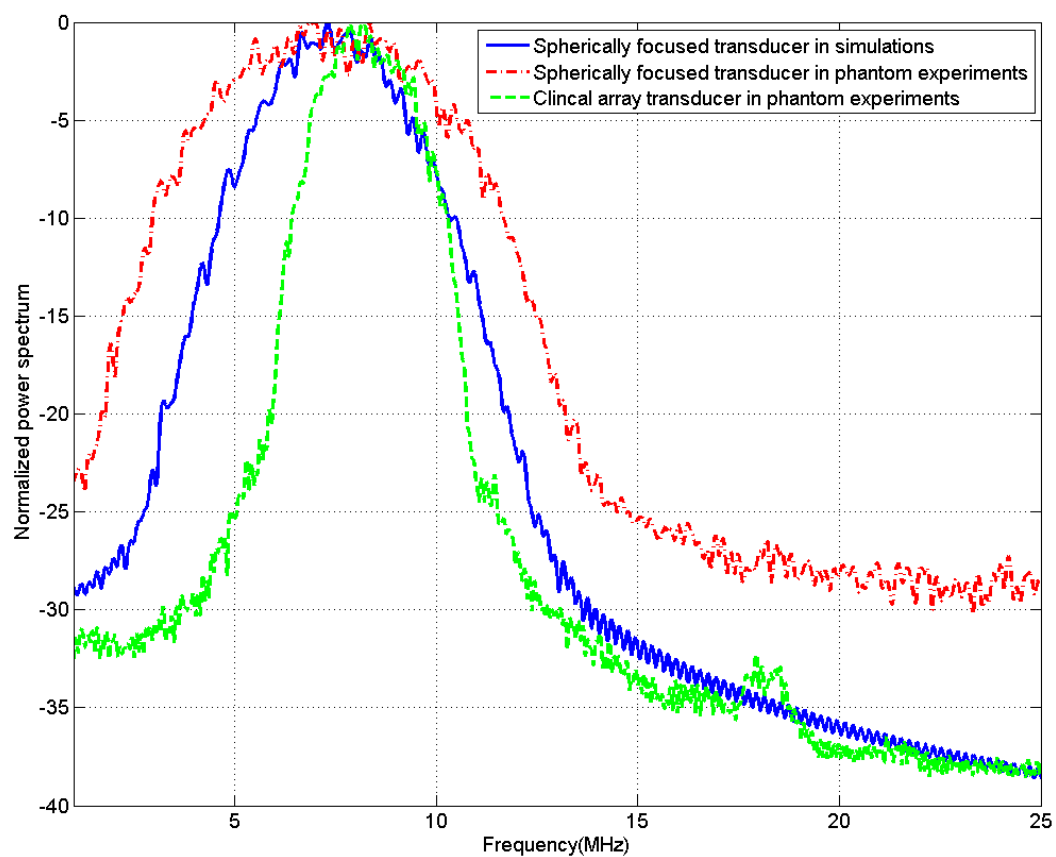


Figure 47 Plot of the normalized power spectrum versus frequency, for the Gaussian focused beam in the simulations, the spherically focused transducer, and the clinical array transducer.

6 SUMMARY AND DISCUSSION

In this thesis, we developed two methods for compensating for the measurement equipment and the total ultrasound attenuation along the propagation path. Because of the random nature of the echoes returned from the tissue during ultrasonic examination, statistical analysis was performed on each method. Another contribution towards this thesis is the optimization of three algorithms that use tissue mimicking phantoms to estimate the local ultrasonic attenuation with a region of interest of tissue. The last contribution is the application of one of the local attenuation estimation algorithms in in-vivo pregnant patient cervix data for the purpose of detecting premature delivery.

In chapter two, we used the spectral fit method to obtain attenuation estimates of the cervix of pregnant patients that are at different gestation ages. Results showed that although there was a large in-between patient variability, there was a relationship between the attenuation coefficient estimates and the interval to delivery and that the results were statistically significant. The significant between subject variability in attenuation coefficient estimates could have arisen from the natural biological variation in the cervix tissue between different women and the variation that is inherent to the attenuation estimation algorithm. Longitudinal studies are required in order to eliminate the in-between patient variability and to detect changes in the attenuation coefficient estimates with increasing gestation on a patient specific basis. As discussed in chapter 3, the attenuation coefficient estimates that are obtained using the spectral difference method have a small bias and variance when the ROIs are homogeneous. However, for the same pregnant patient, the spectral difference method yielded a large variance in the estimates of different regions of the cervix. Although it is possible that different regions in the cervix tissue have different attenuation values, it is

unlikely that the difference in the attenuation between the different regions is very high. Therefore, the high variance in the attenuation estimates of different regions in the cervix of a specific patient is a result of the in-homogeneities within the ROI. Using the hybrid method or the spectral log difference method to obtain the attenuation estimates may yield a smaller variance in the estimates for large ROIs. However, because in-homogeneities in soft tissue are made of changes in both the scatterer size and the scatterer number density, the estimates may not be accurate. The accuracy of the estimates will depend on the magnitude of variation in scatterer size within the ROI.

One way to maximize the accuracy in the ACEs (on the expense of large variance) is to divide the region of interest in tissue into multiple smaller sub-ROIs. These ROIs could be assumed homogeneous, and the spectral difference method can be used to estimate the attenuation coefficient within each sub-ROI. The mean of the estimates should approximate the attenuation coefficient of the original ROI. In future studies of human pregnant patients, we will divide the cervix into small ROIs that can be assumed homogeneous and obtain an attenuation map of the entire cervix. The variance in the estimates is expected to be high due to small ROIs. However the mean value of the estimates should approach the true value of the attenuation coefficient. Figure 48 shows an attenuation map of the cervix of a pregnant patient that was obtained using ROIs that are 99% overlapping. The axial ROI size is 3 pulse lengths, and the lateral ROI size is 5 independent echo lines. Appendix A describes the optimization of the spectral difference method of use in future longitudinal studies of the pregnant patient cervix.

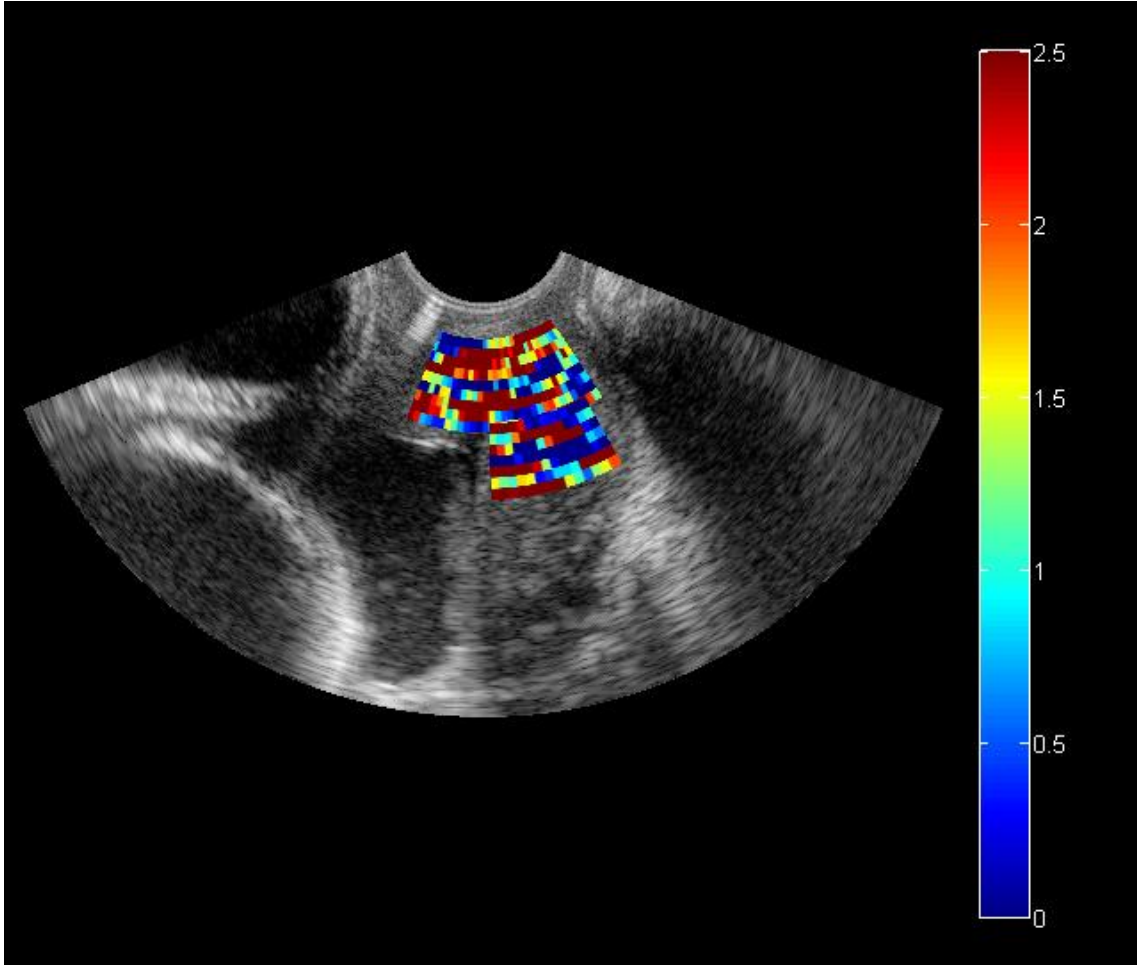


Figure 48 Attenuation map for the cervix of a pregnant patient (1.28 ± 0.98 dB/cm-MHz).
Axial ROI size = 3 pulse lengths, Lateral ROI size = 5 independent echo lines

In clinical settings, multiple scans of the patient cervix should be acquired throughout pregnancy. In each scan, the ROIs that correspond to the cervix are selected. Care must be taken to exclude any tissues that are not part of the cervix as they might have different attenuation values. Using the optimal ROI size that is obtained in phantom experiments (Appendix A), the spectral difference method can then be used to obtain an attenuation map of the entire cervix. Although the variance in the attenuation estimates maybe large, the mean of the estimates should be trusted as the true attenuation coefficient of the tissue. If number

of estimates is small (30 estimates or less) as a result of a small cervix, the mean of the attenuation coefficients estimates should not be trusted especially if the variance in the estimates is large. The clinician will then monitor the change in the attenuation coefficient with gestational age. A change in the attenuation coefficient may signal premature delivery. The clinician should also monitor the dilation of the cervix and the changes in the cervical length with increasing gestation. These tools combined may provide a better predictor of premature delivery.

In chapter 4, the spectral fit method and the multiple filter method that were used by Bigelow for total attenuation estimation were modified by employing a tissue mimicking reference phantom (TMP) instead of a planar reflector to compensate for the transfer function of transducer and the diffraction effects that result from focusing. The two algorithms were derived and statistical analysis was performed on each algorithm to obtain expressions for the variance in the attenuation coefficient estimates in terms of the number of frequency components in the usable frequency range (transducer bandwidth and axial ROI size), the number of independent echoes per ROI (Later ROI size), and the number of independent Gaussian filters in the multiple filter method. We also argue that the difference between the attenuation coefficient of the sample and the attenuation coefficient of the reference also affects the variance in the attenuation estimates. For example, if the attenuation coefficient of the sample is large compared to the attenuation coefficient of the reference, the spectrum of the sample will experience a larger shift towards the lower frequencies compared to the spectrum of the reference and this leads to a small usable frequency range. However, for a given a tissue mimicking phantom with a constant attenuation coefficient and an ultrasound

system with a fixed bandwidth, the only parameter that affects the variance of the estimates is the ROI size.

In chapter 5, we compared the spectral fit method and the multiple filter method. We found that both algorithms are highly dependent on the bandwidth and the ROI size. We also found that for a given ROI size, both the spectral fit method and the multiple filter method with 2 independent Gaussian filters yield comparable results in terms of the bias and the standard deviation of the total attenuation coefficient estimates. We have also shown that in the multiple filter method, using 3 overlapping Gaussian filters and a fourth filter that spans the entire usable frequency range gives better results than using only 2 independent Gaussian filters. We made the argument that using two overlapping Gaussian filters and a third filter that spans the entire usable frequency range may give better results if the amount of overlap between the two filters, and the center frequencies of the two overlapping filters are optimized.

The total attenuation estimation algorithms are highly dependent on bandwidth. One way of increasing the bandwidth is to use high frequency transducers. Using high frequency transducer however, limits the penetration depth in to tissue. Recently, methods that are based on coded excitation and pulse compression have been shown to improve the bandwidth [68]. Surface micro-machined capacitive ultrasonic transducers are new designs that demonstrated a big improvement in the bandwidth [69, 70]. Some ultrasound clinical systems, however, allow the transducer to be excited at three different center frequencies. This feature can be used to increase the usable frequency range in the power spectrum of the backscattered signal. Figure 49 shows a plot of the normalized power spectra that are obtained from the 0.7 dB/cm-MHz tissue mimicking phantom (described in section 3.6) by

exciting a clinical array transducer (L8-3 Linear Array Transducer, z.one Ultrasound System, ZONARE Medical Systems, Inc.) at three different frequencies. This figure shows that there is a large overlap between adjacent power spectra and that the -20 dB bandwidth for each spectrum is between 4 and 5 MHz. However, the -20 dB bandwidth for the combination of the power spectra is 7 MHz, approximately a 50% increase in the bandwidth. This potential increase in the bandwidth of the power spectrum can only be utilized if the effects of the equipment (Transmit pulse and transducer diffraction and electromechanical properties) are compensated by using a tissue mimicking phantom or a planar reflector to obtain reference data.

Figure 50 (a) shows a plot of the ratio of the power spectra from Figure 49 by the power spectra that are obtained for a reference tissue mimicking phantom (the 0.5 dB/cm-MHZ TMP described in section 3.6). Figure 50 (b) shows a plot of the spectrum that is obtained from combining the high frequency spectrum and low frequency spectrum from Figure 50 (a). The two spectra are averaged in the range of frequencies for which they are overlapping. As expected, the usable frequency range is approximately 7MHz.

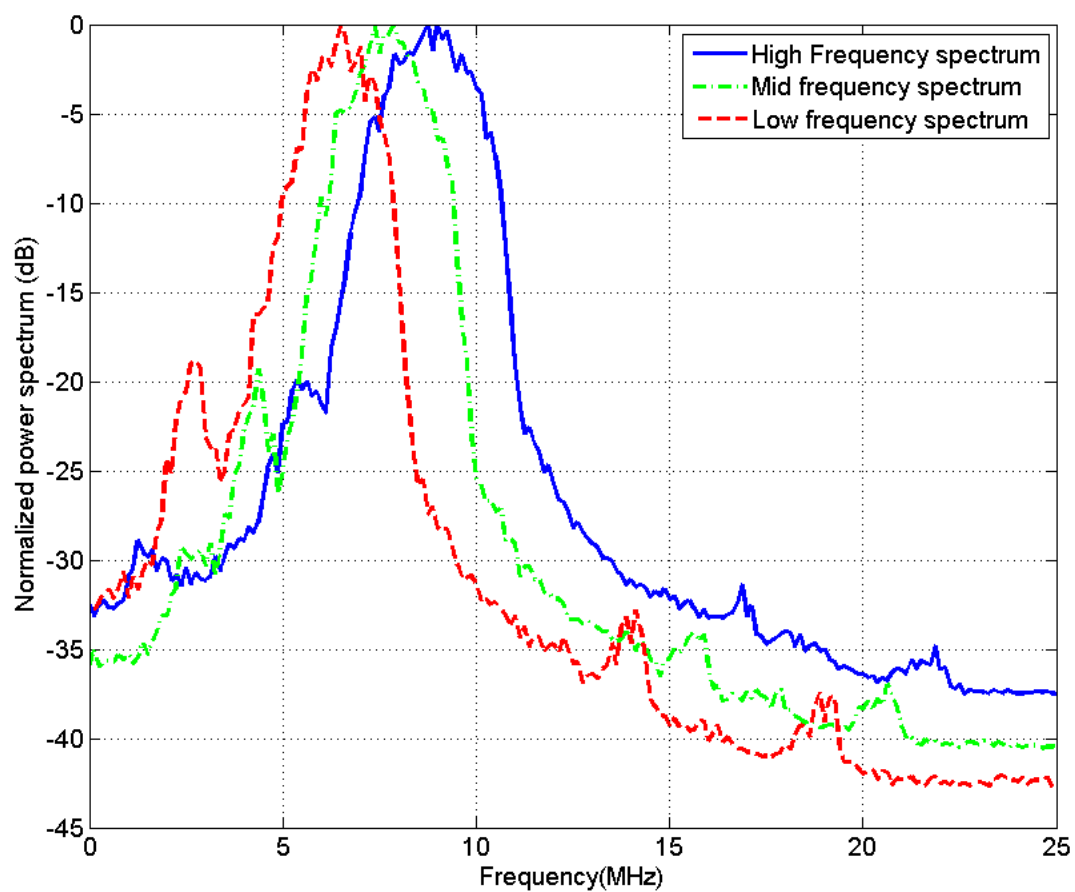


Figure 49 plot of the normalized power spectra that are obtained from a TMP by exciting a clinical array transducer (L8-3 Linear Array Transducer, z.one Ultrasound System, ZONARE Medical Systems, Inc.) at three difference frequencies

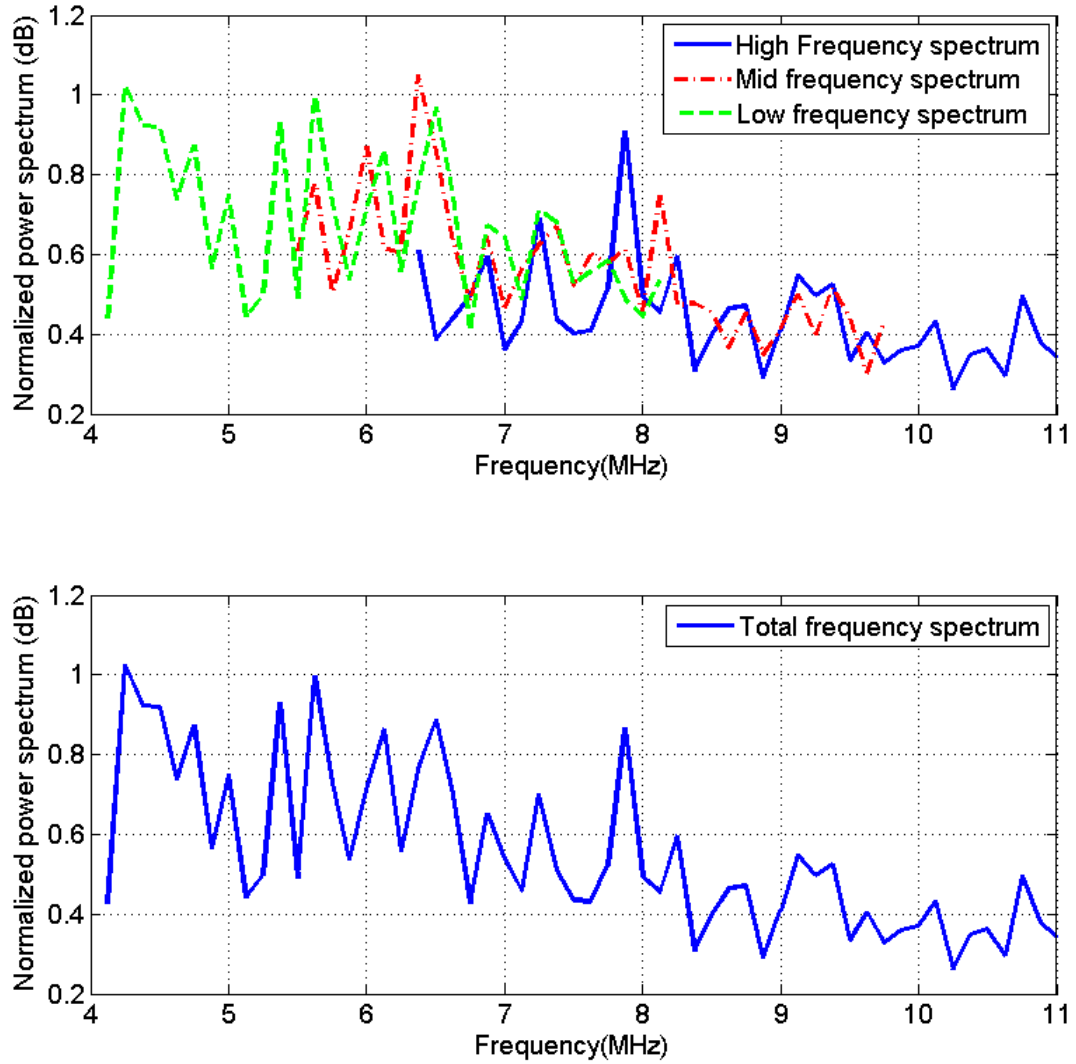


Figure 50 plot of (a) the ratio of the power spectra from Figure 49 by the power spectra that are obtained for a reference tissue mimicking phantom and (b) the spectrum that is obtained from combining the high frequency spectrum and low frequency spectrum from plot (a).

To explore the improvement in the total attenuation estimates that results from increasing the usable frequency range, we fixed the linear array transducer at the surface of

the 0.7dB/cm-MHz TMP (sample) and excited it at three center frequencies. Each time the transducer was excited, one data set was obtained. Using the same settings, we fixed the linear array transducer at the surface of the 0.5dB/cm-MHz TMP (reference) and excited it at three center frequencies. Each time the transducer was excited, one data set was obtained. We then used the multiple filter method with two independent Gaussian filters to obtain total attenuation estimates of overlapping ROIs in the sample TMP. These estimates were obtained for two cases. In the first case, we used only one spectrum from the sample to obtain the attenuation estimates, i.e. the spectrum that results from exciting the transducer at a center frequency of 7.5 MHz. In the second, case we used the spectrum that combines the spectra that were obtained from exciting the transducer at 3 different frequencies.

Figure 51 shows the attenuation map of the 0.7 dB/cm-MHz tissue mimicking phantom that is obtained by using the multiple filter method with two independent Gaussian filters and using the spectrum that is obtained from exciting the transducer at one center frequency (~ 7 MHz) only. Similarly, Figure 52 shows the attenuation map of the 0.7 dB/cm-MHz tissue mimicking phantom that is obtained by using the multiple filter method with two independent Gaussian filters and using the spectrum that combines the spectra that were obtained from exciting the transducer at 3 different frequencies. In both Figure 51 and Figure 52, the axial ROI size is 12 pulse lengths and the lateral ROI size is 35 independent echo lines. In Figure 51, the mean of the attenuation estimates is 0.6003 ± 1.06 dB/cm-MHz. In Figure 52, the mean of the attenuation estimates is 0.7085 ± 0.1323 dB/cm-MHz. Figure 53 and Figure 54 are similar to Figure 51 and Figure 52, respectively, however for these two figures, the axial ROI size is 6 pulse lengths and the lateral ROI size is 10 independent echo lines. In Figure 53, the mean of the attenuation estimates is 0.54 ± 2.35 dB/cm-MHz. In Figure

54, the mean of the attenuation estimates is 0.7013 ± 0.5298 dB/cm-MHz. Based on these results, we conclude that exciting the transducer at 3 different frequencies increases the usable frequency range significantly. The increase in the usable frequency range increases the accuracy and the precision of the total attenuation estimation algorithms. In addition, smaller ROIs can be used to obtain total attenuation estimates.

In clinical settings, compensating for the total attenuation along the propagation path will allow the clinician to obtain important acoustic parameters. For example, in the cervix of pregnant patient, estimating the backscatter coefficient, the scatterer size, and the ratio of coherent to incoherent scattering intensity could provide additional information about tissue microstructure. Monitoring the change in these acoustic parameters with increasing gestation age could signal the changes in tissue microstructure during cervical ripening and assist in predicting premature delivery. In the total attenuation estimation algorithms, it is important that the ROI is homogeneous. However, because the total attenuation estimation algorithms require large ROIs to obtain a small bias a small variance in the estimates, it may be difficult to find large regions of the cervix that may be completely homogeneous. One way to maximize the accuracy in the ACEs (on the expense of large variance) is to divide the region of interest in tissue into multiple smaller sub-ROIs. These ROIs could be assumed homogeneous, and the multiple filter method can be used to estimate the total attenuation coefficient within each sub-ROI. The mean of the estimates should approximate the total attenuation coefficient of the original ROI. This estimate of total attenuation coefficient can be used to compensate for the total attenuation in all cervix regions.

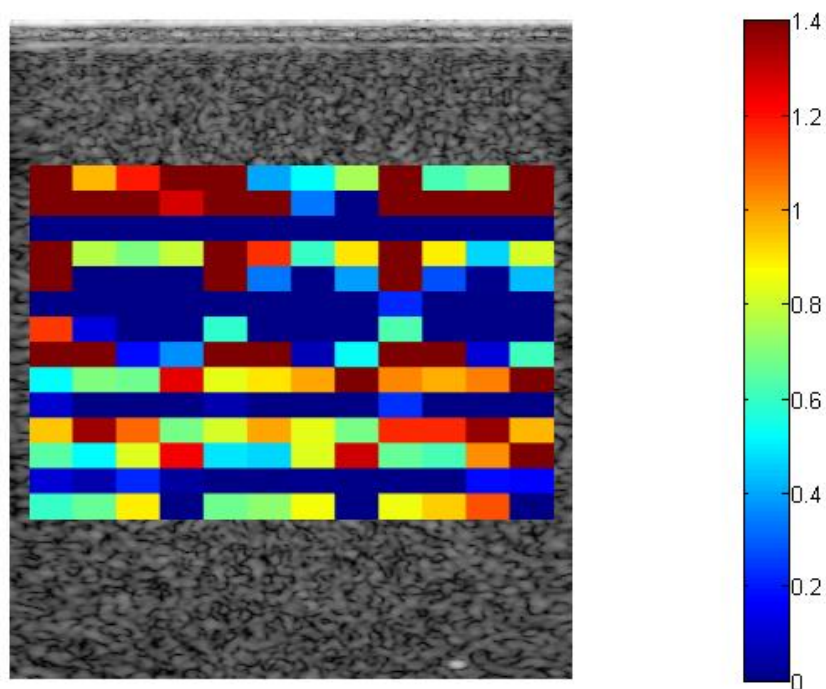


Figure 51 Total attenuation map of the 0.7dB/cm-MHz tissue mimicking phantom that is obtained by using the multiple filter method with two independent Gaussian filters and using the spectrum that is obtained from exciting the transducer at one center frequency (~ 7 MHz) only. The axial ROI size is 12 pulse lengths and the lateral ROI size is 35 independent echo lines. Mean = 0.6003 ± 1.06 dB/cm-MHz

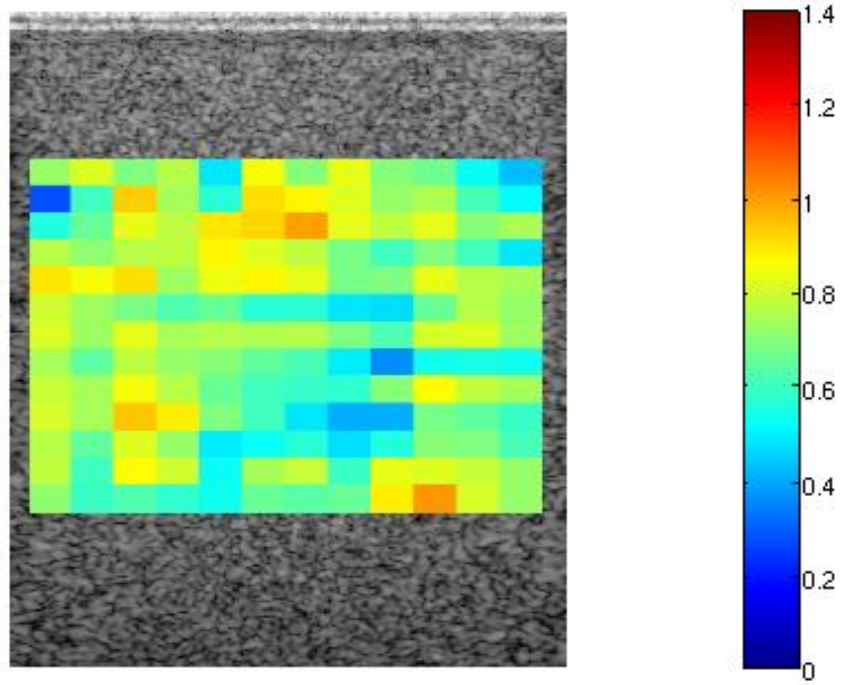


Figure 52 Total attenuation map of the 0.7dB/cm-MHz tissue mimicking phantom that is obtained by using the multiple filter method with two independent Gaussian filters and using the spectrum that combines the spectra from three excitement frequencies of the transducer. The axial ROI size is 12 pulse lengths and the lateral ROI size is 35 independent echo lines.
Mean=0.7085±0.13 dB/cm-MHz

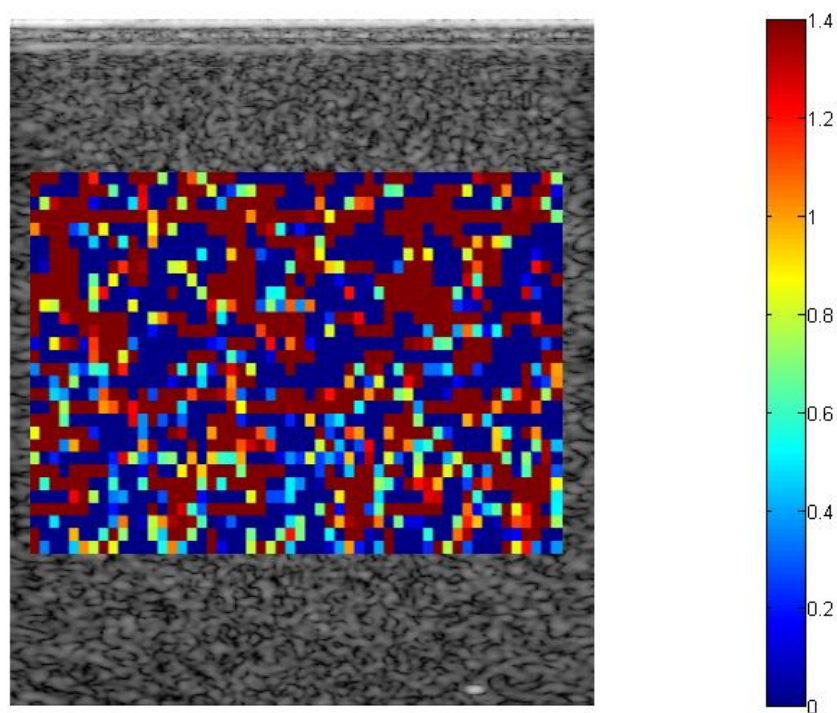


Figure 53 Total attenuation map of the 0.7dB/cm-MHz tissue mimicking phantom that is obtained by using the multiple filter method with two independent Gaussian filters and using the spectrum that is obtained from exciting the transducer at one center frequency (~ 7 MHz) only. The axial ROI size is 6 pulse lengths and the lateral ROI size is 10 independent echo lines. Mean = 0.54 ± 2.35 dB/cm-MHz

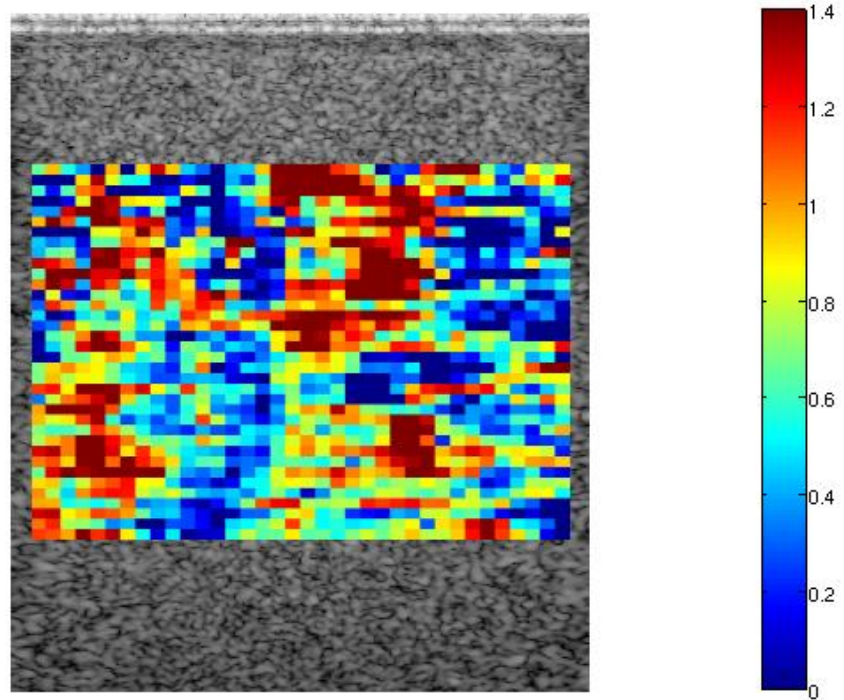


Figure 54 Total attenuation map of the 0.7dB/cm-MHz tissue mimicking phantom that is obtained by using the multiple filter method with two independent Gaussian filters and using the spectrum that combines the spectra from three excitement frequencies of the transducer. The axial ROI size is 6 pulse lengths and the lateral ROI size is 10 independent echo lines.
Mean=0.7013±0.53 dB/cm-MHz

APPENDIX A

OPTIMIZATION OF THE SPECTRAL DIFFERENCE METHOD FOR USE IN THE LONGITUDINAL STUDY OF THE PREGNANT PATIENT CERVIX

In section 3.6, we concluded that the spectral difference method is optimal for use in the longitudinal study of the pregnant patient cervix data. Using small ROIs within the cervix, the spectral difference method can be used to obtain an attenuation map of the entire cervix. Each individual small ROI within the cervix can be assumed homogeneous, even though the cervix may be heterogeneous as a whole. In order to apply the spectral difference method to the patient data however, the ROI size must be optimized. An ROI may be considered optimal if for a large number of ACEs (30 estimates or more), the mean in the ACEs is reasonably close to the true attenuation coefficient. Although a small standard deviation in the ACEs is desired, having small ROIs and keeping an accurate mean of the ACEs is more important. This is true because, as was shown in Chapter 3, any inhomogeneities within the ROI can lead to completely inaccurate estimates of the mean in the ACEs. In this appendix, we use tissue mimicking phantoms to find the optimal ROI size for obtaining a local attenuation map. The RF echo lines were obtained from the trans-vaginal array transducer that was used for pregnant patient cervix scans.

A 6.8 MHz trans-vaginal array transducer (E9-4, z.one Ultrasound System, ZONARE Medical Systems, Inc., Mountain View, CA) was used to obtain two scans (2 independent slices) of the reference tissue mimicking phantom. The tissue mimicking phantom had an attenuation coefficient of 0.5 dB/cm-MHz and a sound propagation speed of 1540 m/s which is similar to the propagation speed in soft tissue. The scattering targets in the phantom were

glass beads with a number density of 160 mm^{-3} and an average scatterer diameter of $35 \text{ }\mu\text{m}$. The spectral difference method was then used to obtain local attenuation maps of the TMP for varying ROI sizes. All the ROIs contain two overlapping time gated windows. The overlapping between the two time gated windows is 50%. The axial ROI size is varied by varying the size of the time gated windows. The lateral ROI size is varied by varying the number of independent echoes per ROI. The attenuation maps were obtained by performing 99% overlapping between the ROIs axially (adjacent ROIs share one time gated window), and 99% overlapping laterally (adjacent ROIs share 99% of the number of echo lines per ROI). **Error! Reference source not found.** shows the local attenuation map of the reference tissue mimicking phantom that is obtained using the spectral difference method for an axial ROI size of 3 pulse lengths and a lateral ROI size of 5 independent echo lines. Figure 55 shows the local attenuation map of the reference tissue mimicking phantom that is obtained using the spectral difference method for an axial ROI size of 10.5 pulse lengths and a lateral ROI size of 10 independent echo lines. The mean in the ACEs for Figure 55 and **Error! Reference source not found.** are $0.4435 \pm 1.10 \text{ dB/cm-MHz}$, and $0.47 \pm 0.12 \text{ dB/cm-MHz}$, respectively.

Table 2 shows the mean and the STD of the ACEs that were obtained for various ROI sizes. It is apparent that as the ROI size increases, the STD in the ACEs decreases. For the ROI that has an axial ROI size of 1.5 pulse lengths and a lateral ROI size of 5 independent echo lines, the bias in the mean of the ACEs is large. However, for ROIs that have an axial ROI size of 3 pulse lengths or more and a lateral ROI size of 5 independent echo lines or more, the bias in the mean of the ACEs is reasonably small (11.3% error for 3 pulse lengths and 5 echo lines), and only slight improvements in the mean of the ACEs are observed as the

ROI size increases. Based on these results, we concluded that ROIs that have an axial of 3 pulse lengths and a lateral size of 5 independent echo lines are optimal for use in the longitudinal study of pregnant patient cervix data.

Axial ROI size (pulse lengths)	Lateral ROI size (Number of independent echo lines)	Mean (dB/cm-MHz) (True attenuation coefficient = 0.5 dB/cm-MHz)	STD(dB/cm-MHz)
1.5	5	0.4147	2.83
3	5	0.4435	1.10
4.5	5	0.4476	0.62
6	5	0.4622	0.39
3	7	0.4542	1.03
3	10	0.4672	0.84
10.5	10	0.47	0.12

Table 2 The mean and the STD of the local attenuation coefficient estimates in the reference tissue mimicking phantom. The estimates were obtained by using the spectral difference method on the RF data of the reference tissue mimicking phantom that is obtained from the trans-vaginal array transducer.

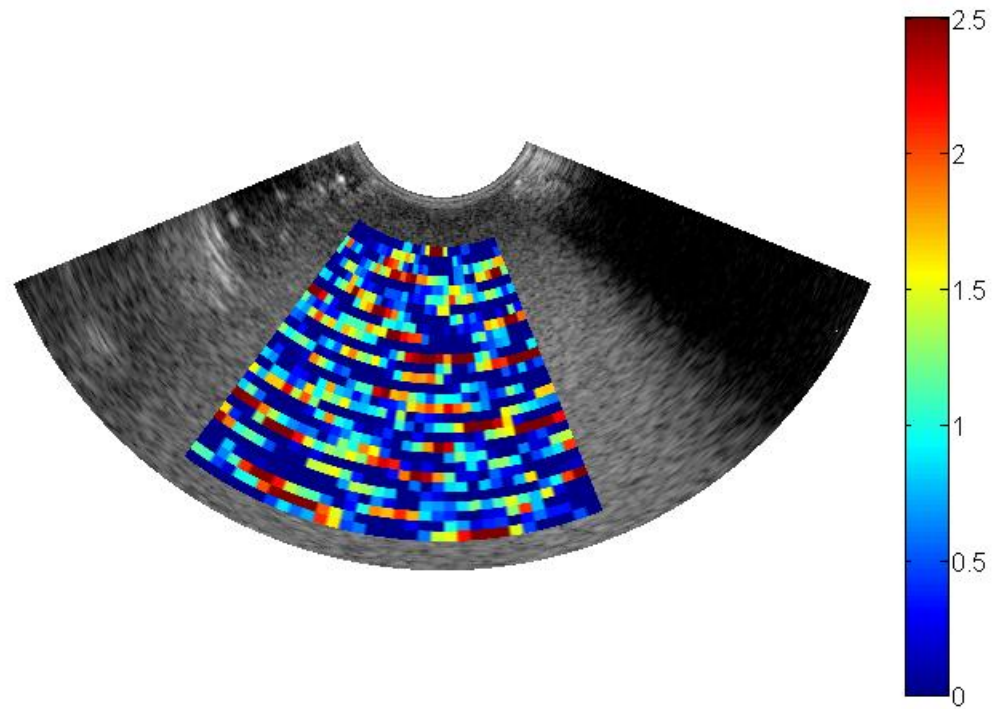


Figure 55 Local attenuation map of the reference tissue mimicking phantom that is obtained using the spectral difference method for an axial ROI size of 3 pulse lengths and a lateral ROI size of 5 independent echo lines. 0.4435 ± 1.10 dB/cm-MHz

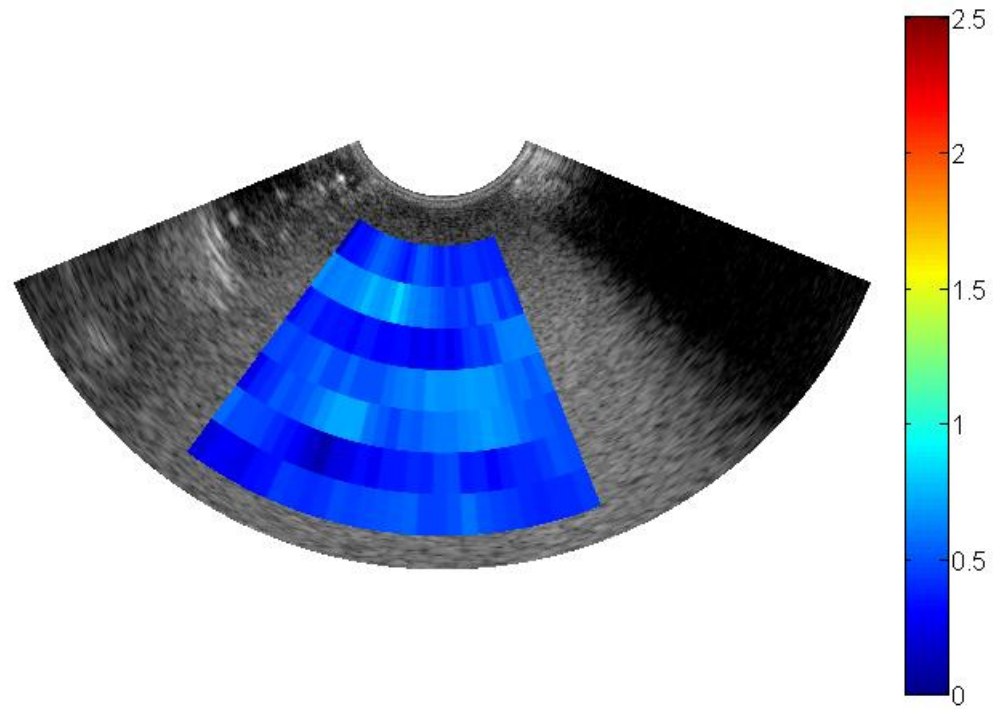


Figure 56 local attenuation maps of the reference tissue mimicking phantom that is obtained using the spectral difference method for an axial ROI size of 10.5 pulse lengths and a lateral ROI size of 10 independent echo lines. 0.47 ± 0.12 dB/cm-MHz

APPENDIX B**PROCEDURE FOR EXTRACTING THE RAW DATA FROM A ZONARE
ULTRASOUND SYSTEM**

1. Before the raw data can be extracted. You must have Matlab component runtime installed in your computer. This allows Matlab executable files to run on the computer.
2. To install Matlab component runtime (MCR), open my documents, and enter <ftp://12.40.200.87> in the address bar. This website will not open if you enter it in internet explorer.
3. Enter this information in the prompt window:

User Name: advtech2

Password: invent420
4. Open the folder that has the Matlab version you have. For example : “R2008b MCR v79”
5. Double click on “MCRInstaller.exe” to download it to your computer.
6. After the download is complete, double click on “MCRInstaller.exe” to install it.
7. Move all the raw data files to a folder in the C: drive. The command !IQread (discussed below) doesn’t work in the U: drive.
8. Move the executable file “IQread.exe” to the same folder where the raw data is located in the C: drive. Make sure that this file corresponds to the Zonare clinical system you have. If it gives and license file error, contact Zonare and obtain the correct “IQread.exe” for your clinical system.

9. The raw data files that are used to generate the radio frequency (RF) signals start with “US” and end with “R”. Example “US00010R”.
10. Open Matlab and set your current folder to be the folder where the raw data files and the “IQread.exe” are located.
11. Extract the raw data: In the command prompt, type “!IQread” followed by the raw data file name. Example: “IQread US00010R”. This will automatically generate the IQ data file and place it in the current folder. The IQ data file name is “rawData.mat”
12. If multiple files are to be extracted, it is important to rename the IQ data file from “rawData.mat” to another name. Example “US00010R.mat”. This is because every time the “IQread” command is run, the “rawData.mat” file gets overridden with the new IQ data.
13. To view the contents of the “rawData.mat” file, type “load rawData.mat” in the command prompt. A struct named “Bmode” will load. To view the contents of the struct “Bmode,” type “Bmode” in the command prompt. Bmode contains a struct named “param” and array named “data.” The array “data” contains the IQ data from 5 frames. The struct “param” contains information about the transducer and the acquisition details. To view the contents of the “param” struct, type “Bmode.param.”

APPENDIX C

PROCEDURE FOR OBTAINING LOCAL ATTENUATION MAPS

1. To obtain local attenuation maps from data that is obtained from exciting the transducer at 3 center frequencies open folder “Combined files 3 center frequencies.”
2. To obtain local attenuation maps from data that is obtained from exciting the transducer at only 1 center frequencies open folder “Combined files”.
3. Open the file “Local_attenuation_map.m.”
4. Use the function “local_atten_est_mod”. If you want to skip every other 2 echo lines to get independent echoes: This will give you 3 estimates per ROI. The three estimates are then averaged.
5. Use the function “local_atten_est.m” otherwise. This will give only one estimate per ROI. This uses all the available echoes in the ROI and doesn’t skip every other 2 echo lines.
6. You will be prompted to enter whether the attenuation coefficient in the reference is linear with frequency. Enter “y” if linear or “n” in it is nonlinear with frequency. Make sure you use small letters.
 - a. If linear, you will be prompted to enter the attenuation coefficient slope in dB/cm-MHz.
 - b. In nonlinear, you will be asked to enter the name of the attenuation file of the reference phantom. The file must contain two row vectors, “f_ref” and “atten_ref”. “f_ref” is the frequency and must be in Hz. “atten_ref” is the

attenuation coefficient and must be in dB/cm. For example, enter “atten_BRP_phantom”.

7. A prompt will display “Should we compensate for the transmission coefficient into the reference phantom”. You will need a .mat file that has the transmission coefficient data. This file must contain the vector “T_in” the transmission coefficient from water to phantom and the vector, “T_out” the transmission coefficient from phantom to water and the frequency in Hz “f”.
 - a. Enter 0 if no compensation is required. This is true when the reference phantom has no transmission window (saran wrap for example).
 - b. Enter 1 if a Wisconsin phantom is used as the reference phantom
 - c. Enter 2 if the Gammex phantom is used as the reference phantom
8. A window will open prompting you to select the raw data for the reference. Select the tissue mimicking phantom raw data file (or files) that you want to use as a reference.
9. A second window will open prompting you to select the raw data for the sample. Select the sample raw data file (or files) for the sample.
10. In the command prompt, you will be prompted to enter the coordinates of your region of interest in the sample. At the same time 2 figures are displayed. Figure 1 shows the original B mode image, and Figure 2 shows the B mode image in vertical columns. Use the zoom tool in Figure 2 to select your region of interest. Enter the coordinates of your ROI as follows: [top row bottom row ; left column right column]. For example: [20 130; 10 150].

11. In the command prompt, you will be prompted to enter the coordinates of the usable data in the reference. Again, use the zoom tool in Figure 2 to select the usable region in reference B mode image. As before, enter the coordinate of the usable region in the command prompt. [top row bottom row ; left column right column].
12. You will then be prompted to enter the row where the attenuation starts in the reference. Look at Figure 2 and find the row where the attenuate starts and enter the value in the command prompt.
13. You will then be prompted to enter the row where the attenuation starts in the sample. Look at Figure 2 and find the row where the attenuate starts and enter the value in the command prompt.
14. Steps 11 and 12 are not required to obtain the attenuation map, however because some functions are shared, a value must be entered for each one. These values will not be used in the code.
15. Figure 1 will then be displayed. This figure shows the correlation between the rows of the RF signals. This figure will allow you to obtain a rough estimate of the pulse length. Use the zoom tool in Figure 1 to select the pulse length and enter the number of samples per pulse length in the command prompt. For example: 50. In the matlab code, this number will be multiplied by the time spacing between the samples to obtain the pulse length in seconds.
16. Another Figure 1 will be displayed. This figure shows the Full width half maximum (FWHM) of the power spectrum obtained for varying time gated windows sizes (pulse lengths). Chose the optimum number of spatial pulse lengths per ROI to be

the value for which the FWHM stabilizes. Enter this value in the command prompt.

For example: 5.

17. You will then be prompted to enter the percent overlap between the time gated windows. For example: 50.
18. You will then be prompted to enter the number of echoes per ROI. Enter you desired number of echoes per ROI. If you want to use all the echoes available, enter the number that is displayed above the prompt “input the number of echoes per ROI.”
19. You will then be prompted to enter the % overlap between the echo lines. This is the overlap in the lateral direction. For example: 50.
20. You will then be prompted to enter the % overlap in the axial direction. This is the % overlap between ROIs axially. For example: 50.
21. You will then be prompted to enter the number of time gated windows per ROI. The ROI length is related the window size, the number of windows, and the percent overlap between the windows according to the following equation.

$$number_of_windows = \left(\frac{ROI_length}{window_size} - \frac{\%overlap}{100} \right) \left(\frac{100}{100 - \%overlap} \right)$$

$$ROI_length = window_size \times \left[\left(1 - \frac{\%overlap}{100} \right) \times number_of_windows + \frac{\%overlap}{100} \right]$$

where the ROI length and the window size are in pulse lengths . The number of windows must be an integer. Example1: window size = 5 pulse lengths, %overlap = 50%, number of windows = 3. ROI length = 5[(1-0.5)*3 +0.5]= 10 pulse lengths.

22. A Plot of the power spectrum of the sample and the power spectrum of the reference in dB will be displayed.

- a. If the transducer is excited at only 1 frequency, similar plots will appear as you press enter in the command prompt depending on the total number of windows available. Look at the spectra and find the noise level. You will then be prompted to enter the noise level in dB. For example : -20
 - b. If the transducer is excited at 3 frequencies, you need to enter the noise level for each plot. Each plot corresponds to either the high center frequency, the middle center frequency, or the low center frequency. Unlike in (a) above, only 1 spectrum per center frequency is displayed. This spectrum corresponds to the first window.
23. Three figures will then be displayed showing attenuation maps. Figure 1 is the attenuation map obtained using the spectral log difference method. Figure 2 is the attenuation map obtained using the spectral difference method. Figure 3 is the attenuation map using the hybrid method.

APPENDIX D

PROCEDURE FOR OBTAINING TOTAL ATTENUATION MAPS

1. To obtain total attenuation maps from data that is obtained from exciting the transducer at 3 center frequencies open the folder “Combined files 3 center frequencies.”
2. Open the file “Total_attenuation_map.m.”
3. Use the function “Total_atten_est_mod”. If you want to skip every other 2 echo lines to get independent echoes: This will give you 3 estimates per ROI. The three estimates are then averaged.
4. You will be prompted to enter whether the attenuation coefficient in the reference is linear with frequency. Enter “y” if linear or “n” if it is nonlinear with frequency. Make sure you use small letters.
 - a. If linear, you will be prompted to enter the attenuation coefficient slope in dB/cm-MHz.
 - b. In nonlinear, you will be asked to enter the name of the attenuation file of the reference phantom. The file must contain two row vectors, “f_ref” and “atten_ref”. “f_ref” is the frequency and must be in Hz. “atten_ref” is the attenuation coefficient and must be in dB/cm. For example, enter “atten_BRP_phantom”.
24. A prompt will display “Should we compensate for the transmission coefficient into the reference phantom”. You will need a .mat file that has the transmission coefficient data. This file must contain the vector “T_in” the transmission coefficient

from water to phantom and the vector, “T_out” the transmission coefficient from phantom to water and the frequency in Hz “f”.

- c. Enter 0 if no compensation is required. This is true when the reference phantom has no transmission window (saran wrap for example).
 - d. Enter 1 if a Wisconsin phantom is used as the reference phantom
 - e. Enter 2 if the Gammex phantom is used as the reference phantom
5. A window will open prompting you to select the raw data for the reference. Select the tissue mimicking phantom raw data file (or files) that you want to use as a reference.
6. A second window will open prompting you to select the raw data for the sample. Select the sample raw data file (or files) for the sample.
7. In the command prompt, you will be prompted to enter the coordinates of your region of interest in the sample. At the same time 2 figures are displayed. Figure 1 shows the original B mode image, and Figure 2 shows the B mode image in vertical columns. Use the zoom tool in Figure 2 to select your region of interest. Enter the coordinates of your ROI as follows: [top row bottom row ; left column right column]. For example: [20 130; 10 150].
8. In the command prompt, you will be prompted to enter the coordinates of the usable data in the reference. Again, use the zoom tool in Figure 2 to select the usable region in reference B mode image. As before, enter the coordinate of the usable region in the command prompt. [top row bottom row ; left column right column].

9. You will then be prompted to enter the row where the attenuation starts in the reference. Look at Figure 2 and find the row where the attenuate starts and enter the value in the command prompt.
10. You will then be prompted to enter the row where the attenuation starts in the sample. Look at Figure 2 and find the row where the attenuate starts and enter the value in the command prompt.
11. Figure 1 will then be displayed. This figure shows the correlation between the rows of the RF signals. This figure will allow you to obtain a rough estimate of the pulse length. Use the zoom tool in Figure 1 to select the pulse length and enter the number of samples per pulse length in the command prompt. For example: 50. In the matlab code, this number will be multiplied by the time spacing between the samples to obtain the pulse length in seconds.
12. Another Figure 1 will be displayed. This figure shows the Full width half maximum (FWHM) of the power spectrum obtained for varying time gated windows sizes (pulse lengths). Chose the optimum number of spatial pulse lengths per ROI to be the value for which the FWHM stabilizes. Enter this value in the command prompt. For example: 5.
13. You will then be prompted to enter the percent overlap between the time gated windows. This means the % overlapping between ROI in the axial direction. For example: 50.
14. You will then be prompted to enter the number of echoes per ROI. Enter you desired number of echoes per ROI. If you want to use all the echoes available, enter the number that is displayed above the prompt "input the number of echoes per ROI."

15. You will then be prompted to enter the % overlap between the echo lines. This is the overlap in the lateral direction. For example: 50.
16. A Plot of the power spectrum of the sample and the power spectrum of the reference in dB will be displayed.
 - a. If the transducer is excited at only 1 frequency, similar plots will appear as you press enter in the command prompt depending on the total number of windows available. Look at the spectra and find the noise level. You will then be prompted to enter the noise level in dB. For example : -20
 - b. If the transducer is excited at 3 frequencies, you need to enter the noise level for each plot. Each plot corresponds to either the high center frequency, the middle center frequency, or the low center frequency. Unlike in (a) above, only 1 spectrum per center frequency is displayed. This spectrum corresponds to the first window.
17. Three figures will then be displayed showing attenuation maps. Figure 1 is the attenuation map obtained using the spectral fit method. Figure 2 is the attenuation map obtained using the multiple filter method with two Gaussian filters. Figure 3 is the attenuation map using the multiple filter method with 2 Gaussian filters and a third filter that used the entire usable frequency range.

APPENDIX E

PROCEDURE FOR OBTAINING THE BACKSCATTER COEFFICIENT

1. To obtain the backscatter coefficient from data that is obtained from exciting the transducer at 3 center frequencies open folder “Combined files 3 center frequencies.”
2. To obtain the backscatter coefficient from data that is obtained from exciting the transducer at only 1 center frequencies open folder “Combined files”
3. Use the function “BSC_est_mod”. If you want to skip every other 2 echo lines to get independent echoes: This will give you 3 estimates per ROI. The three estimates are then averaged.
4. Use the function “BSC_est.m” otherwise. This will give only one estimate per ROI. This uses all the available echoes in the ROI and doesn’t skip every other 2 echo lines.
5. You will be prompted to enter whether the attenuation coefficient in the reference is linear with frequency. Enter “y” if linear or “n” in it is nonlinear with frequency. Make sure you use small letters.
 - a. If linear, you will be prompted to enter the attenuation coefficient slope in dB/cm-MHz.
 - b. In nonlinear, you will be asked to enter the name of the attenuation file of the reference phantom. The file must contain two row vectors, “f_ref” and “atten_ref”. “f_ref” is the frequency and must be in Hz. “atten_ref” is the attenuation coefficient and must be in dB/cm. For example, enter “atten_BRP_phantom”.

6. A prompt will display “Should we compensate for the transmission coefficient into the reference phantom”. You will need a .mat file that has the transmission coefficient data. This file must contain the vector “T_in” the transmission coefficient from water to phantom and the vector, “T_out” the transmission coefficient from phantom to water, and “f” the frequency in Hz. The vectors “T_in” and “T_out” must be row vectors of equal size and must be obtained for the same frequency range in the BSC file. i.e. the vectors “f”, ”BSC”, ”T_in”, ”T_out” must all be of equal size.
 - a. Enter 0 if no compensation is required. This is true when the reference phantom has no transmission window (saran wrap for example).
 - b. Enter 1 if a Wisconsin phantom is used as the reference phantom
 - c. Enter 2 if the Gammex phantom is used as the reference phantom
7. You will be prompted to enter the name of the backscatter coefficient file of the reference phantom. This .mat file must contain the frequency vector “f” in Hz, and the “BSC” vector in (1/sr). Both “f” and “BSC” must be row vectors with equal size. Example: <1x900double>.
8. A window will open prompting you to select the raw data for the reference. Select the tissue mimicking phantom raw data file (or files) that you want to use as a reference.
9. A second window will open prompting you to select the raw data for the sample. Select the sample raw data file (or files) from which you want to obtain an attenuation map.
10. In the command prompt, you will be prompted to enter the coordinates of your region of interest in the sample. At the same time 2 figures are displayed. Figure 1 shows

the original B mode image, and Figure 2 shows the B mode image in vertical columns. Use the zoom tool in Figure 2 to select your region of interest. Enter the coordinates of your ROI as follows: [top row bottom row ; left column right column]. Example: [20 130; 10 150].

11. In the command prompt, you will be prompted to enter the coordinates of the usable data in the reference. Again, use the zoom tool in Figure 2 to select the usable region in reference B mode image. As before, enter the coordinate of the usable region in the command prompt. [top row bottom row ; left column right column].
12. You will then be prompted to enter the row where the attenuation starts in the reference. Look at Figure 2 and find the row where the attenuation starts and enter that value in the command prompt.
13. You will then be prompted to enter the row where the attenuation starts in the sample. Look at Figure 2 and find the row where the attenuation starts and enter that value in the command prompt.
14. Figure 1 will then be displayed. This figure shows the correlation between the row of the RF signals. This figure will allow you to obtain a rough estimate of the pulse length. Use the zoom tool in Figure 1 to select the pulse length and enter the number of samples per pulse length in the command prompt. For example: 50. In the matlab code, this number will be multiplied by the time spacing between the samples to obtain the pulse length in seconds.
15. Another Figure 1 will be displayed. This figure shows the Full width half maximum (FWHM) of the power spectrum obtained for varying time gated windows sizes (pulse lengths). Chose the optimum number of spatial pulse lengths per ROI to be

the value for which the FWHM stabilizes. Enter this value in the command prompt.

For example: 5.

16. You will then be prompted to enter the percent overlap between the time gated windows. For example: 50.
17. You will then be prompted to enter the number of echoes per ROI. Enter you desired number of echoes per ROI. If you want to use all the echoes available, enter the number that is displayed above the prompt “input the number of echoes per ROI.”
18. You will then be prompted to enter the % overlap between the echo lines. This is the overlap in the lateral direction. For example: 50.
19. You will then be prompted to enter the % overlap between the ROIs in the axial direction. For example: 50.
18. A Plot of the power spectrum of the sample and the power spectrum of the reference in dB will be displayed.
 - a. If the transducer is excited at only 1 frequency, similar plots will appear as you press enter in the command prompt depending on the total number of windows available. Look at the spectra and find the noise level. You will then be prompted to enter the noise lever in dB. For example : -20
 - b. If the transducer is excited at 3 frequencies, you need to enter the noise lever for each plot. Each plot corresponds to either the high center frequency, the middle center frequency, or the low center frequency. Unlike in (a) above, only 1 spectrum per center frequency is displayed. This spectrum corresponds to the first window.

19. You will then be prompted to enter the attenuation coefficient of the reference in dB/cm-MHz.
- a. If the reference has a linear frequency dependent attenuation coefficient, enter the attenuation coefficient slope in dB/cm-MHz.
 - b. If the reference has a nonlinear frequency dependent, you must load the reference attenuation .mat file. This .mat file must contain two row vectors of equal size “freq_ref”, and “atten_ref”. “freq_ref” must be in Hz, and “atten_ref” must be in Np/cm.
20. You will then be prompted to enter the attenuation coefficient of the sample in dB/cm-MHz.
- a. If the sample has a linear frequency dependent attenuation coefficient, enter the attenuation coefficient slope in dB/cm-MHz.
 - b. If the sample has a nonlinear frequency dependent, you must load the sample attenuation .mat file. This .mat file must contain two row vectors of equal size “freq_sample,” and “atten_sample,” “freq_sample” must be in Hz, and “atten_sample” must be in Np/cm.
21. If parts b of 19, and 20 above are the case, you must uncomment the lines of the code where you load the files of attenuation of the sample and or the reference.
22. Finally, a plot that shows the average BSC over all windows with respect to frequency is displayed. The BSC of the reference is also displayed.

APPENDIX F

PROCEDURE FOR OBTAINING THE SCATTERER SIZE

1. To obtain the scatterer size maps from data that is obtained from exciting the transducer at 3 center frequencies open folder “Combined files 3 center frequencies.”
2. To obtain the scatterer size maps from data that is obtained from exciting the transducer at only 1 center frequencies open folder “Combined files”
3. Open the file “scatterer_size_map.mat.”
4. Use the function “scatterer_size_est_mod”. If you want to skip every other 2 echo lines to get independent echoes: This will give you 3 estimates per ROI. The three estimates are then averaged.
5. Use the function “scatterer_size_est.m” otherwise. This will give only one estimate per ROI. This uses all the available echoes in the ROI and doesn’t skip every other 2 echo lines.
6. You will be prompted to enter whether the attenuation coefficient in the reference is linear with frequency. Enter “y” if linear or “n” if it is nonlinear with frequency. Make sure you use small letters.
 - a. If linear, you will be prompted to enter the attenuation coefficient slope in dB/cm-MHz.
 - b. In nonlinear, you will be asked to enter the name of the attenuation file of the reference phantom. The file must contain two row vectors, “f_ref” and “atten_ref”. “f_ref” is the frequency and must be in Hz. “atten_ref” is the attenuation coefficient and must be in dB/cm. For example, enter “atten_BRP_phantom”.

7. A prompt will display “Should we compensate for the transmission coefficient into the reference phantom”. You will need a .mat file that has the transmission coefficient data. This file must contain the vector “T_in” the transmission coefficient from water to phantom and the vector, “T_out” the transmission coefficient from phantom to water, and “F” the frequency in Hz.
 - a. Enter 0 if no compensation is required. This is true when the reference phantom has no transmission window (saran wrap for example).
 - b. Enter 1 if a Wisconsin phantom is used as the reference phantom
 - c. Enter 2 if the Gammex phantom is used as the reference phantom
8. Run the file “scatterer_size_map.mat.”
9. A window will open prompting you to select the raw data for the reference. Select the tissue mimicking phantom raw data file (or files) that you want to use as a reference.
10. A second window will open prompting you to select the raw data for the sample. Select the sample raw data file (or files) from which you want to obtain an attenuation map.
11. In the command prompt, you will be prompted to enter the coordinates of your region of interest in the sample. At the same time 2 figures are displayed. Figure 1 shows the original B mode image, and Figure 2 shows the B mode image in vertical columns. Use the zoom tool in Figure 2 to select your region of interest. Enter the coordinates of your ROI as follows: [top row bottom row ; left column right column]. Example: [20 130; 10 150].

12. In the command prompt, you will be prompted to enter the coordinates of the usable data in the reference. Again, use the zoom tool in Figure 2 to select the usable region in reference B mode image. As before, enter the coordinate of the usable region in the command prompt. [top row bottom row ; left column right column].
13. You will then be prompted to enter the row where the attenuation starts in the reference. Look at Figure 2 and find the row where the attenuation starts and enter that value in the command prompt.
14. You will then be prompted to enter the row where the attenuation starts in the sample. Look at Figure 2 and find the row where the attenuation starts and enter that value in the command prompt.
15. Figure 1 will then be displayed. This figure shows the correlation between the row of the RF signals. This figure will allow you to obtain a rough estimate of the pulse length. Use the zoom tool in Figure 1 to select the pulse length and enter the number of samples per pulse length in the command prompt. For example: 50. In the matlab code, this number will be multiplied by the time spacing between the samples to obtain the pulse length in seconds.
16. Another Figure 1 will be displayed. This figure shows the Full width half maximum (FWHM) of the power spectrum obtained for varying time gated windows sizes (pulse lengths). Chose the optimum number of spatial pulse lengths per ROI to be the value for which the FWHM stabilizes. Enter this value in the command prompt. For example: 5.

17. You will then be prompted to enter the percent overlap between the time gated windows. This is the % overlap between the ROIs in the axial direction. For example: 50.
18. You will then be prompted to enter the number of echoes per ROI. Enter you desired number of echoes per ROI. If you want to use all the echoes available, enter the number that is displayed above the prompt “input the number of echoes per ROI.”
19. You will then be prompted to enter the % overlap between the echo lines. This is the overlap in the lateral direction. For example: 50.
23. A Plot of the power spectrum of the sample and the power spectrum of the reference in dB will be displayed.
 - a. If the transducer is excited at only 1 frequency, similar plots will appear as you press enter in the command prompt depending on the total number of windows available. Look at the spectra and find the noise level. You will then be prompted to enter the noise lever in dB. For example : -20
 - b. If the transducer is excited at 3 frequencies, you need to enter the noise lever for each plot. Each plot corresponds to either the high center frequency, the middle center frequency, or the low center frequency. Unlike in (a) above, only 1 spectrum per center frequency is displayed. This spectrum corresponds to the first window.
24. You will then be prompted to enter the attenuation coefficient of the reference in dB/cm-MHz.
 - a. If the reference has a linear frequency dependent attenuation coefficient, enter the attenuation coefficient slope in dB/cm-MHz.

- b. If the reference has a nonlinear frequency dependent, you must load the reference attenuation .mat file. This .mat file must contain two row vectors of equal size “freq_ref”, and “atten_ref”. “freq_ref” must be in Hz, and “atten_ref” must be in Np/cm.
25. You will then be prompted to enter the attenuation coefficient of the sample in dB/cm-MHz.
- a. If the sample has a linear frequency dependent attenuation coefficient, enter the attenuation coefficient slope in dB/cm-MHz.
 - b. If the sample has a nonlinear frequency dependent, you must load the sample attenuation .mat file. This .mat file must contain two row vectors of equal size “freq_sample,” and “atten_sample,” “freq_sample” must be in Hz, and “atten_sample” must be in Np/cm.
26. If parts b of 24, and 25 above are the case, you must uncomment the lines of the code where you load the files of attenuation of the sample and or the reference.
27. Finally, a plot that shows the scatterer size attenuation map is displayed.

ACKNOWLEDGMENTS

I would like to express the deepest appreciation to my major advisor, Dr. Timothy Bigelow, who has conveyed a spirit of hard work, commitment to research and scholarship, and an excitement in regard to teaching. Without his guidance and persistent help, this dissertation would not have been possible.

I would like to thank my committee members for their direction in the project. I also thank Dr. Barbara McFarlin for providing us with pregnant patient cervix data, and for the informative discussions about premature delivery.

Finally, I would like to give special thanks to my wife, my parents, and my brothers for their encouragement, support, patience, and unending love.

REFERENCES

- [1] M. L. Oelze, J. F. Zachary, and J. William D. O'Brien, "Characterization of tissue microstructure using ultrasonic backscatter: Theory and technique for optimization using a Gaussian form factor," *The Journal of the Acoustical Society of America*, vol. 112, pp. 1202-1211, 2002.
- [2] J. C. G. a. S. Leeman, "Echo structure in medical ultrasonic pulse-echo scanning " *Physics in Medicine and Biology* vol. 22, pp. 431-443, 1977.
- [3] J. Mamou, M. L. Oelze, J. William D. O'Brien, and J. F. Zachary, "Identifying ultrasonic scattering sites from three-dimensional impedance maps," *The Journal of the Acoustical Society of America*, vol. 117, pp. 413-423, 2005.
- [4] F. L. Lizzi, M. Greenebaum, E. J. Feleppa, M. Elbaum, and D. J. Coleman, "Theoretical framework for spectrum analysis in ultrasonic tissue characterization," *The Journal of the Acoustical Society of America*, vol. 73, pp. 1366-1373, 1983.
- [5] F. L. Lizzi, M. Ostromogilsky, E. J. Feleppa, M. C. Rorke, and M. M. Yaremko, "Relationship of Ultrasonic Spectral Parameters to Features of Tissue Microstructure," *Ultrasonics, Ferroelectrics and Frequency Control, IEEE Transactions on*, vol. 34, pp. 319-329, 1987.
- [6] F. L. Lizzi, et al, "Computer model of ultrasonic hyperthermia and ablation for ocular tumors using bmode data," *Ultrasound in Medicine & Biology*, vol. 18, 1992.
- [7] F. L. Lizzi, E. J. Feleppa, M. Astor, and A. Kalisz, "Statistics of ultrasonic spectral parameters for prostate and liver examinations," *Ultrasonics, Ferroelectrics and Frequency Control, IEEE Transactions on*, vol. 44, pp. 935-942, 1997.
- [8] D. Nicholas, C. R. Hill, and D. K. Nassiri, "Evaluation of backscattering coefficients for excised human tissues: Principles and techniques," *Ultrasound in Medicine & Biology*, vol. 8, pp. 7-15, 1982.
- [9] R. F. W. Michael F. Insana, Brain S. Garra, David G. Brown, Thomas H. Shawker, "Analysis of ultrasound image texture via generalized rician statistics," *Optical Engineering*, vol. 25, pp. 743-748, 1986.
- [10] M. F. I. Robert F. Wagner, David G. Brown, "Unfied approach to the detection and classification of speckle texture in diagnostic ultrasound," *Optical Engineering*, vol. 26, pp. 738-742, 1986.
- [11] M. L. Oelze and J. W. D. O'Brien, "Defining optimal axial and lateral resolution for estimating scatterer properties from volumes using ultrasound backscatter," *The Journal of the Acoustical Society of America*, vol. 115, pp. 3226-3234, 2004.
- [12] P. M. Morse and K. U. Ingard, *Theoretical Acoustics*: Princeton University Press, 1986.
- [13] L. L. Fellingham and F. G. Sommer, "Ultrasonic Characterization of Tissue Structure in the In Vivo Human Liver and Spleen," *Sonics and Ultrasonics, IEEE Transactions on*, vol. 31, pp. 418-428, 1984.
- [14] F. W. Kremkau, *Diagnostic Ultrasound: Principles and Instruments*, 5 ed.: W.B Saunders Company, 1998.
- [15] L. Felligham, "A stochastic approach to ultrasonic tissue characterization," in *Stanford University*, 1979.
- [16] M. L. Oelze, W. D. O'Brien, Jr., J. P. Blue, and J. F. Zachary, "Differentiation and characterization of rat mammary fibroadenomas and 4T1 mouse carcinomas using

- quantitative ultrasound imaging," *Medical Imaging, IEEE Transactions on*, vol. 23, pp. 764-771, 2004.
- [17] E. J. Feleppa, F. L. Lizzi, D. J. Coleman, and M. M. Yaremko, "Diagnostic spectrum analysis in ophthalmology: A physical perspective," *Ultrasound in Medicine & Biology*, vol. 12, pp. 623-631, 1986.
 - [18] L. Landini, R. Sarnelli, and F. Squartini, "Frequency-dependent attenuation in breast tissue characterization," *Ultrasound in Medicine & Biology*, vol. 11, pp. 599-603, 1985/8// 1985.
 - [19] L. Landini and R. Sarnelli, "Evaluation of the attenuation coefficients in normal and pathological breast tissue," *Medical and Biological Engineering and Computing*, vol. 24, pp. 243-247, 1986.
 - [20] Z. F. Lu, J. A. Zagzebski, and F. T. Lee, "Ultrasound backscatter and attenuation in human liver with diffuse disease," *Ultrasound in Medicine & Biology*, vol. 25, pp. 1047-1054, 1999.
 - [21] J. M. Reid, "Self-reciprocity calibration of echo-ranging transducers," *The Journal of the Acoustical Society of America*, vol. 55, pp. 862-868, 1974.
 - [22] L. X. Yao, J. A. Zagzebski, and E. L. Madsen, "Backscatter coefficient measurements using a reference phantom to extract depth-dependent instrumentation factors," *Ultrasonic Imaging*, vol. 12, pp. 58-70, 1990.
 - [23] M. F. Insana, J. A. Zagzebski, and E. L. Madsen, "Improvements in the spectral difference method for measuring ultrasonic attenuation" *Ultrasonic imaging*, vol. 5, pp. 331-345, 1983.
 - [24] S. A. Goss, R. L. Johnston, and F. Dunn, "Comprehensive compilation of empirical ultrasonic properties of mammalian tissues," *The Journal of the Acoustical Society of America*, vol. 64, pp. 423-457, 1978.
 - [25] T. Varghese and K. D. Donohue, "Estimating mean scatterer spacing with the frequency-smoothed spectral autocorrelation function," *Ultrasonics, Ferroelectrics and Frequency Control, IEEE Transactions on*, vol. 42, pp. 451-463, 1995.
 - [26] T. J. Hall, M. F. Insana, L. A. Harrison, and G. G. Cox, "Ultrasonic measurement of glomerular diameters in normal adult humans," *Ultrasound in Medicine & Biology*, vol. 22, pp. 987-997, 1996.
 - [27] T. A. Bigelow and W. D. O'Brien, Jr., "Scatterer size estimation in pulse-echo ultrasound using focused sources: Calibration measurements and phantom experiments," *The Journal of the Acoustical Society of America*, vol. 116, pp. 594-602, 2004.
 - [28] T. A. Bigelow, M. L. Oelze, and J. William D. O'Brien, "Estimation of total attenuation and scatterer size from backscattered ultrasound waveforms," *The Journal of the Acoustical Society of America*, vol. 117, pp. 1431-1439, 2005.
 - [29] T. A. Bigelow, "Ultrasound attenuation estimation using backscattered echoes from multiple sources," *The Journal of the Acoustical Society of America*, vol. 124, pp. 1367-1373, 2008.
 - [30] W. M. Callaghan, M. F. MacDorman, S. A. Rasmussen, C. Qin, and E. M. Lackritz, "The Contribution of Preterm Birth to Infant Mortality Rates in the United States," *Pediatrics*, vol. 118, pp. 1566-1573, October 1, 2006 2006.
 - [31] R. L. Goldenberg, "The Management of Preterm Labor," *Obstetrics & Gynecology*, vol. 100, pp. 1020-1037, 2002.

- [32] P. C. Leppert, "Anatomy and physiology of cervical ripening," *Clin Obstet Gynecol*, vol. 38, pp. 267-79, Jun 1995.
- [33] P. C. Leppert, R. Kokenyesi, C. A. Klemenich, and J. Fisher, "Further evidence of a decorin-collagen interaction in the disruption of cervical collagen fibers during rat gestation," *American Journal of Obstetrics and Gynecology*, vol. 182, pp. 805-812, 2000.
- [34] B. L. McFarlin, W. D. O'Brien, Jr, M. L. Oelze, J. F. Zachary, and R. C. White-Traut, "Quantitative Ultrasound Assessment of the Rat Cervix," *J Ultrasound Med*, vol. 25, pp. 1031-1040, August 1, 2006 2006.
- [35] J. Pohlhammer and J. W. D. O'Brien, "Dependence of the ultrasonic scatter coefficient on collagen concentration in mammalian tissues," *The Journal of the Acoustical Society of America*, vol. 69, pp. 283-285, 1981.
- [36] S. Leeman, L. Ferrari, J. P. Jones, and M. Fink, "Perspectives on Attenuation Estimation from Pulse-Echo Signals," *Sonics and Ultrasonics, IEEE Transactions on*, vol. 31, pp. 352-361, 1984.
- [37] S. W. Flax, N. J. Pelc, G. H. Glover, F. D. Gutmann, and M. McLachlan, "Spectral characterization and attenuation measurements in ultrasound," *Ultrasonic Imaging*, vol. 5, pp. 95-116, 1983.
- [38] P. A. Narayana and J. Ophir, "The measurement of attenuation in nonlinearly attenuating media by the zero crossing method," *Ultrasound in Medicine & Biology*, vol. 10, pp. 715-718, 1984 1984.
- [39] K. J. Parker and R. C. Waag, "Measurement of Ultrasonic Attenuation Within Regions Selected from B-Scan Images," *Biomedical Engineering, IEEE Transactions on*, vol. BME-30, pp. 431-437, 1983.
- [40] T. A. Bigelow and W. D. O'Brien, Jr., "Impact of local attenuation approximations when estimating correlation length from backscattered ultrasound echoes," *The Journal of the Acoustical Society of America*, vol. 120, pp. 546-553, 2006.
- [41] K. J. Parker, R. M. Lerner, and R. C. Waag, "Comparison of techniques for in vivo attenuation measurements," *Biomedical Engineering, IEEE Transactions on*, vol. 35, pp. 1064-1068, 1988.
- [42] R. Kuc and M. Schwartz, "Estimating the Acoustic Attenuation Coefficient Slope for Liver from Reflected Ultrasound Signals," *Sonics and Ultrasonics, IEEE Transactions on*, vol. 26, pp. 353-361, 1979.
- [43] R. Kuc, "Clinical Application of an Ultrasound Attenuation Coefficient Estimation Technique for Liver Pathology Characterization," *Biomedical Engineering, IEEE Transactions on*, vol. BME-27, pp. 312-319, 1980.
- [44] R. Kuc, "Estimating acoustic attenuation from reflected ultrasound signals: Comparison of spectral-shift and spectral-difference approaches," *Acoustics, Speech and Signal Processing, IEEE Transactions on*, vol. 32, pp. 1-6, 1984.
- [45] H. Kim and T. Varghese, "Hybrid Spectral Domain Method for Attenuation Slope Estimation," *Ultrasound in Medicine & Biology*, vol. 34, pp. 1808-1819, 2008.
- [46] T. A. Bigelow, B. L. McFarlin, W. D. O'Brien, Jr., and M. L. Oelze, "In vivo ultrasonic attenuation slope estimates for detecting cervical ripening in rats: Preliminary results," *The Journal of the Acoustical Society of America*, vol. 123, pp. 1794-1800, 2008.

- [47] K. Hyungsuk and T. Varghese, "Attenuation estimation using spectral cross-correlation," *Ultrasonics, Ferroelectrics and Frequency Control, IEEE Transactions on*, vol. 54, pp. 510-519, 2007.
- [48] G. Treece, R. Prager, and A. Gee, "Ultrasound attenuation measurement in the presence of scatterer variation for reduction of shadowing and enhancement," *Ultrasonics, Ferroelectrics and Frequency Control, IEEE Transactions on*, vol. 52, pp. 2346-2360, 2005.
- [49] T. A. Bigelow, "Estimating the Total Ultrasound Attenuation Along the Propagation path by Applying Multiples Filters to Backscattered Echoes From a Single Spherically Focused Source," *IEEE Transactions on Ultrasonics, Ferroelectrics, and Frequency Control*, 2010.
- [50] M. F. Insana, R. F. Wagner, D. G. Brown, and T. J. Hall, "Describing small-scale structure in random media using pulse-echo ultrasound," *The Journal of the Acoustical Society of America*, vol. 87, pp. 179-192, 1990.
- [51] N. Parmar and M. C. Kolios, "Attenuation mapping for monitoring thermal therapy using ultrasound transmission imaging," in *Engineering in Medicine and Biology Society, 2004. IEMBS '04. 26th Annual International Conference of the IEEE*, 2004, pp. 1329-1332.
- [52] N. Parmar and M. Kolios, "An investigation of the use of transmission ultrasound to measure acoustic attenuation changes in thermal therapy," *Medical and Biological Engineering and Computing*, vol. 44, pp. 583-591, 2006.
- [53] H. C. Starritt, F. A. Duck, and V. F. Humphrey, "Forces acting in the direction of propagation in pulsed ultrasound fields," *Physics in Medicine and Biology*, vol. 36, pp. 1465-1474, 1991.
- [54] S. Calle, J.-P. Remenieras, O. B. Matar, M. E. Hachemi, and F. Patat, "Temporal analysis of tissue displacement induced by a transient ultrasound radiation force," *The Journal of the Acoustical Society of America*, vol. 118, pp. 2829-2840, 2005.
- [55] H. Tu, J. Zagzebski, and Q. Chen, "Attenuation estimations using envelope echo data: Analysis and simulations," *Ultrasound in Medicine & Biology*, vol. 32, pp. 377-386, 2006.
- [56] P. a. J. F. G. He, "Application of stochastic analysis to ultrasonic echoes---Estimation of attenuation and tissue heterogeneity from peaks of echo envelope," *The Journal of the Acoustical Society of America*, vol. 79, pp. 526-534, 1986.
- [57] D. A. Sidney, "Three-dimensional ultrasound power deposition modeling, thermal field visualization, and clinical integration of hyperthermia therapy," *Massachusetts Institute of Technology*, 1997.
- [58] T. A. Bigelow, "Estimating the total ultrasound attenuation along the propagation path by applying multiple filters to backscattered echoes from a single spherically focused source," *Ultrasonics, Ferroelectrics and Frequency Control, IEEE Transactions on*, vol. 57, pp. 900-907, 2010.
- [59] J. A. Z. M. F. Insana, E. L. Madsen, and G. R. Frank,, "Analysis of a spectral difference method for measuring the slope of attenuation coefficients," *Ultrasonic Imaging*, vol. 5, pp. 173-173, 1983.
- [60] K. A. Wear, "A Gaussian framework for modeling effects of frequency-dependent attenuation, frequency-dependent scattering, and gating," *Ultrasonics, Ferroelectrics and Frequency Control, IEEE Transactions on*, vol. 49, pp. 1572-1582, 2002.

- [61] M. F. Insana and T. J. Hall, "Parametric ultrasound imaging from backscatter coefficient measurements: image formation and interpretation," *Ultrason Imaging*, vol. 12, pp. 245-67, Oct 1990.
- [62] P. R. Bevington, *Data reduction and error analysis for the physical sciences*, 1969.
- [63] P. Chaturvedi and M. F. Insana, "Error bounds on ultrasonic scatterer size estimates," *The Journal of the Acoustical Society of America*, vol. 100, pp. 392-399, 1996.
- [64] S. L. Marple, *Digital spectral analysis with applications*. Englewood Cliffs, NJ, 1987.
- [65] R. L. B. George Casella, *Statistical Inference*, 2 ed.: Duxbury Press, 2001.
- [66] T. A. Bigelow, "Improved algorithm for estimation of attenuation along propagation path using backscattered echoes from multiple sources," *Ultrasonics*, vol. 50, pp. 496-501, 2009.
- [67] T. Bigelow, "Estimating the total ultrasound attenuation along the propagation path by applying multiple filters to backscattered echoes from a single spherically focused source," *Ultrasonics, Ferroelectrics and Frequency Control, IEEE Transactions on*, vol. 57, pp. 900-907, 2010.
- [68] M. L. Oelze, "Bandwidth and resolution enhancement through pulse compression," *Ultrasonics, Ferroelectrics and Frequency Control, IEEE Transactions on*, vol. 54, pp. 768-781, 2007.
- [69] I. Ladabaum, J. Xuecheng, H. T. Soh, A. Atalar, and B. t. Khuri-Yakub, "Surface micromachined capacitive ultrasonic transducers," *Ultrasonics, Ferroelectrics and Frequency Control, IEEE Transactions on*, vol. 45, pp. 678-690, 1998.
- [70] A. S. Ergun, G. G. Yaralioglu, and B. T. Khuri-Yakub, "Capacitive Micromachined Ultrasonic Transducers: Theory and Technology," *Journal of Aerospace Engineering*, vol. 16, pp. 76-84, 2003.